

# **Comprehensive Study of Wind Loads on Parapets**

**Rania Bedair**

**A Thesis**

**in**

**The Department**

**of**

**Building, Civil & Environmental Engineering**

**Presented in Partial Fulfillment of the Requirements**

**For the Degree of Doctor of Philosophy (Building Engineering) at**

**Concordia University**

**Montreal, Quebec, Canada**

**April 2009**

**© Rania Bedair, 2009**



Library and Archives  
Canada

Published Heritage  
Branch

395 Wellington Street  
Ottawa ON K1A 0N4  
Canada

Bibliothèque et  
Archives Canada

Direction du  
Patrimoine de l'édition

395, rue Wellington  
Ottawa ON K1A 0N4  
Canada

*Your file* *Votre référence*  
ISBN: 978-0-494-63348-9  
*Our file* *Notre référence*  
ISBN: 978-0-494-63348-9

**NOTICE:**

The author has granted a non-exclusive license allowing Library and Archives Canada to reproduce, publish, archive, preserve, conserve, communicate to the public by telecommunication or on the Internet, loan, distribute and sell theses worldwide, for commercial or non-commercial purposes, in microform, paper, electronic and/or any other formats.

The author retains copyright ownership and moral rights in this thesis. Neither the thesis nor substantial extracts from it may be printed or otherwise reproduced without the author's permission.

---

In compliance with the Canadian Privacy Act some supporting forms may have been removed from this thesis.

While these forms may be included in the document page count, their removal does not represent any loss of content from the thesis.

**AVIS:**

L'auteur a accordé une licence non exclusive permettant à la Bibliothèque et Archives Canada de reproduire, publier, archiver, sauvegarder, conserver, transmettre au public par télécommunication ou par l'Internet, prêter, distribuer et vendre des thèses partout dans le monde, à des fins commerciales ou autres, sur support microforme, papier, électronique et/ou autres formats.

L'auteur conserve la propriété du droit d'auteur et des droits moraux qui protègent cette thèse. Ni la thèse ni des extraits substantiels de celle-ci ne doivent être imprimés ou autrement reproduits sans son autorisation.

---

Conformément à la loi canadienne sur la protection de la vie privée, quelques formulaires secondaires ont été enlevés de cette thèse.

Bien que ces formulaires aient inclus dans la pagination, il n'y aura aucun contenu manquant.

  
**Canada**

## **ABSTRACT**

### **COMPREHENSIVE STUDY OF WIND LOADS ON PARAPETS**

**Rania Bedair, Ph. D.**

**Concordia University, 2009**

The current thesis aims at defining and evaluating the local (components and cladding) wind loads on parapets. For the first time, it was attempted to measure such loads in full-scale, in order to address the issues encountered in previous wind tunnel studies. Field testing was carried out using the full-scale experimental building (3.97 m long, 3.22 m wide and 3.1 m high) of Concordia University (located near the soccer field at the Loyola Campus). In order to define individual surface pressures as well as their combined effect from both parapet surfaces, simultaneous peak and mean wind-induced pressures were measured on both exterior and interior surfaces of a uniform perimeter parapet with a height of 0.5 m. Roof edge and corner pressures were also recorded. In addition, a complete wind flow simulation was performed in the Boundary Layer Wind Tunnel (BLWT) of Concordia University using a 1/50 scale model of the experimental building with two different parapet heights, equivalent to 0.5 and 1 m. The choice of geometric scale based on correctly modeling the turbulence intensity at the roof height. The wind tunnel results were compared with the field data for validation purposes. In general, the comparison shows good agreement, although some discrepancies were identified for critical wind directions.

In the past, it was difficult to directly model and record the parapet surface pressures, due to modeling limitations. Therefore, wind loads on parapets were mainly estimated from pressures measured on the wall and the roof of the building in the vicinity of a parapet. The current results demonstrate, in general, that the design method provided in the ASCE 7-05 overestimates the total load on the parapet. In addition, design recommendations are provided and can be considered by the standards.

Numerical simulation of the wind flow over the test building model with the parapet was also performed by using the CFD code Fluent 6.1.22. The steady-state RANS equations were solved with two modified  $k-\varepsilon$  turbulence models, namely the RNG  $k-\varepsilon$  model and the RLZ  $k-\varepsilon$  model. Considering the current state-of-the-art, peak pressures are not predicted reliably by computational approaches. Therefore, in the present study only mean wind-induced pressures on the roof and on parapet surfaces were computed. The computational results show that parapets act to reduce high negative pressures on the leading edge and to make the distribution of mean pressures on the roof more uniform. The simulated pressures are generally in good agreement with the corresponding wind tunnel data.

## ACKNOWLEDGMENTS

I wish to express my sincere gratitude to **Dr. Ted Stathopoulos** for his supervision, guidance, encouraging and support during the course of this work.

Acknowledgments are due to all the members of thesis committee for their constructive suggestions and to Dr. Patrick Saathoff for his assistance during the early stage of the experimental work

I would like to express my sincere gratitude to my parents, sisters, brother and my lovely sons. Special worm appreciation is given to my husband for his assistance, understanding, encouraging, support and love.

## TABLE OF CONTENTS

LIST OF TABLES	xi	
LIST OF FIGURES	xii	
NOMENCLATURE	xvi	
ABBREVIATIONS	xix	
<b>CHAPTER 1</b>	<b>INTRODUCTION</b>	
1.1	Testing of Low-rise Building	1
1.2	Flat Roofs with Parapets	3
1.3	Significance of the Study	3
1.4	Research Objectives	4
1.5	Work Methodology	5
1.6	Flow Patterns on a Low Building	6
1.7	Outline of the Thesis	7
<b>CHAPTER 2</b>	<b>LITERATURE REVIEW</b>	
2.1	Full-scale Investigations	10
2.1.1	Building roofs with parapets	15
2.2	Wind Tunnel Investigations	16
2.2.1	Wind loads on roofs with parapets	20
2.2.2	Wind loads on parapets themselves	26

2.3	Numerical Computations	27
2.4	Current Wind Loading Standards Regarding Parapets	32
2.5	Summary	33
<b>CHAPTER 3</b>	<b>NUMERICAL SIMULATION</b>	
3.1	Introduction to FLUENT	42
3.2	Governing Equations	43
3.3	Turbulence Models	44
3.3.1	Standard $k-\varepsilon$ model	45
3.3.2	Realizable $k-\varepsilon$ model	45
3.3.3	RNG $k-\varepsilon$ model	46
3.4	Numerical Simulation Procedure	47
3.4.1	Computational domain	48
3.4.2	Grid generation	49
3.4.3	Boundary conditions	50
3.5	Sensitivity study of the numerical solution	53
<b>CHAPTER 4</b>	<b>EXPERIMENTAL WORK</b>	
4.1	Full-scale Testing	62
4.1.1	Experimental building	63
4.1.2	Measurement of wind speed and direction	64
4.1.3	Upstream wind flow parameters	65
4.1.4	Reference static pressure	66

4.1.5	Pressure measurements	67
4.1.6	Verification of the Collected Data	69
4.2	Wind Tunnel Modeling	70
4.2.1	Modeling of the experimental Building	71
4.2.2	Boundary Layer Simulation	72
4.2.3	Wind-induced pressure	75
4.2.3.1	Pressure Measurements	76
4.2.3.2	Extreme value analysis	77

**CHAPTER 5            EXPERIMENTAL RESULTS AND COMPARISONS**

5.1	Local Loading Coefficients	95
5.1.1	Correlation of pressures on the roof and the interior parapet surface	98
5.1.2	Correlation of pressures on the exterior And the interior parapet surface	100
5.1.3	Total local loading coefficients on parapets	101
5.1.4	Parapet pressures: full-scale versus wind tunnel	102
5.1.5	Comparisons with other studies	103
5.1.6	Comparison with NBCC (2005)	105
5.2	Area-Averaged Loading Coefficients	106
5.2.1	Comparisons with the ASCE 7-05	108

<b>CHAPTER 6</b>	<b>NUMERICAL RESULTS AND DISCUSSION</b>	
6.1	Flow Patterns around the Building	126
6.2	Mean pressure distribution on the roof	127
6.3	Effect of parapet height on roof pressures	129
6.4	Mean pressures on the parapet itself	129
<b>CHAPTER 7</b>	<b>CONCLUSIONS, RECOMMENDATIONS AND FUTURE WORK</b>	
7.1	Summary	139
7.2	Concluded Remarks	141
7.3	Recommendation Based on the Current Study	145
7.4	Limitations of the Present Study	146
7.5	Future Work	147
	<b>REFERENCES</b>	149
	<b>APPENDIX A</b>	
A.1	Velocity and Turbulence Parameters	170
A.2	Anemometer Calibration	175
A.3	DSM System Setting and Operating Principle	176
A.5	Gumbel Plot	179

## **APPENDIX B**

B.1	Wind Speed and Turbulence Intensity Profiles (ESDU, 1983)	180
B.2	Minimum Design Loads for Buildings and Other Structures, Sec. 6.5 Analysis Procedures (ASCE 7-05)	181
B.2.1	Main wind force-resisting system	181
B.2.2	Components and cladding	182

## LIST OF TABLES

Table 3.1	Specification of computational domain sets used in the current analysis	55
Table 4.1	Stability classification (Sedefian and Bennet, 1980)	79
Table 4.2	Full-scale testing parameters	80
Table 4.3	Wind tunnel modeling parameters for different simulated exposures	81
Table 4.4	Wind tunnel modeling parameters used in the present study	82
Table 5.1	Characteristics of different models used in each study	112
Table 5.2	Comparison of parapet load coefficients derived from NBCC (2005) with the current measured values	113
Table 6.1	Numerical and experimental pressure coefficients	131
Table B.1	Internal pressure coefficient, $GC_{pi}$	183

## LIST OF FIGURES

Figure 1.1	An aerial view of low buildings in a city center	8
Figure 1.2	Vortex formation on roof edges (Cook, 1985)	9
Figure 2.1	Corner mean pressure coefficients in terms of $h_p/L$ (Stathopoulos et al., 1992)	36
Figure 2.2	Parapet wall at the WERFL of TTU(parapet under construction, 2004)	37
Figure 2.3	Roof corner pressure coefficients for cut-parapet configurations (Stathopoulos and Baskaran, 1988-b)	38
Figure 2.4	Turbulent air flow field around a cube (Murakami, 1990)	39
Figure 2.5	Mean stream lines expected around the center line of the current building	40
Figure 2.6	Assumed load acting on the parapet (ASCE-7, 2005)	41
Figure 3.1	Flow chart of numerical computation method	56
Figure 3.2	Building configurations and computational domain (not to scale)	57
Figure 3.3	Grid arrangements for the computational domain: (a) Near the building model (b) For the whole domain.	58
Figure 3.4	Inlet and incident vertical profiles of (a) Turbulence intensity, (b) Mean velocity, (c) Turbulent kinetic energy, (d) Turbulent dissipation rate	59
Figure 3.5	Computational domain used in sensitivity analysis	60
Figure 3.6	Experimental and computational pressure coefficients with different computational domains	61
Figure 4.1	Basic exposure of the experimental station (South-West)	83
Figure 4.2	Details of the test building	84

Figure 4.3	Details of parapet section and tap locations	85
Figure 4.4	Flow patterns around a rectangular building (ASHRAE, 1999)	86
Figure 4.5	Mean wind speed and direction measured during 24 hours (a) Wind speed (b) Wind direction	87
Figure 4.6	Typical time histories for wind speed and wind direction measured at the anemometer height	88
Figure 4.7	Typical time histories for parapet surface pressure coefficients	89
Figure 4.8	The wind tunnel in simulated terrain (a) Wind tunnel inlet (b) Inside view of the tunnel	90
Figure 4.9	Building models with different parapet heights	91
Figure 4.10	Details of pressure tap layout of the building model	92
Figure 4.11	Profiles of turbulence intensity and mean velocity, and the spectrum at the roof height: (a) Longitudinal turbulence intensity profile and (b) Mean wind velocity profile (c) Wind spectrum at the roof height	93
Figure 4.12	Extreme value behavior for a segment of the $C_p$ time history of Tap $B1i$ for perpendicular wind direction: (a) Time history (data point 1-600) (b) Gumbel plot	94
Figure 5.1	Surface parapet pressure coefficients recorded near the corner (Tap $B1$ ) (a) Exterior surface parapet pressure coefficients (b) Interior surface parapet pressure coefficients	114
Figure 5.2	Surface parapet pressure coefficients recorded at the mid-span (Tap $B3$ ) (a) Exterior surface parapet pressure coefficients (b) Interior surface parapet pressure coefficients	115
Figure 5.3	Comparison of peak pressure coefficients on the roof and the inside parapet surface measured near corner (Tap $B1$ ) (a) Full-scale pressure coefficients (b) Wind tunnel pressure coefficients	116

Figure 5.4	Comparison of peak pressure coefficients on the roof and the inside parapet surface measured at mid-span (Tap <i>B3</i> ) (a) Full-scale pressure coefficients (b) Wind tunnel pressure coefficients	117
Figure 5.5	Effect of wind direction on the correlation coefficients of $C_{Pr}$ and $C_{Pi}$	118
Figure 5.6	Comparison between Pressure coefficients measured in Full-scale and Wind tunnel	119
Figure 5.7	Effect of wind direction on the correlation Coefficients of $C_{Pe}$ and $C_{Pi}$	120
Figure 5.8	Peak local load coefficients on the parapet measured (a) Pressure coefficients at the corner (Tap <i>B1</i> ) (b) Pressure coefficients at mid-span (Tap <i>B3</i> )	121
Figure 5.9	Comparison of peak pressure coefficients from different studies: (c) Exterior surface parapet pressure coefficients (d) Interior surface parapet pressure coefficients (c) Simultaneous combined pressure coefficients from both surfaces	122
Figure 5.10	Variation of peak loading coefficients (obtained from the most critical azimuth) with different tributary areas: (a) Exterior parapet loading coefficients (b) Interior parapet loading coefficients (c) Net loading from both surfaces	123
Figure 5.11	Comparison of edge region loading coefficients with ASCE 7-05 (a) Exterior parapet loading coefficients (b) Interior parapet loading coefficients (c) Net loading from both surfaces	124
Figure 5.12	Comparison of interior region loading coefficients with ASCE 7-05 : (a) Exterior parapet loading coefficients (b) Interior parapet loading coefficients (c) Net loading from both surfaces	125
Figure 6.1	Mean velocity vector field around the building (Vertical cross-section) (a) Upstream standing vortex (b) Near wake recirculation	

	(c) Separation region	132
Figure 6.2	Mean velocity vector field around the building (Plan-view)	
Figure 6.3	Contours of pressure coefficient on roof surface from different studies ( $h_p = 0$ m): (a) RNG $k-\varepsilon$ (present study) (b) N-R two layer method (Zhou, 1995) (c) Experimental (Hunt, 1982)	133
Figure 6.4	Contours of pressure coefficients on roof surface (current study): (a) Wind tunnel, $h_p = 0.1$ m (b) RNG $k-\varepsilon$ , $h_p = 0.1$ m	134
Figure 6.5	Pressure coefficient along the center line of building roof: (a) $h_p = 0.1$ m (b) $h_p = 0.2$ m	135
Figure 6.6	Effect of parapet height on roof pressure	136
Figure 6.7	Change of parapet surface pressure coefficients with parapet height (a) Individual mean pressure coefficients (b) Combined mean pressure coefficients	137
Figure A.1	Calibration of the anemometer used in field testing	170
Figure A.2	Mean velocity and turbulence intensity profiles for different exposures (a) Terrain-1 (b) Terrain-2 (c) Terrain-3 (d) Terrain-5	175
Figure A.3	DSM-3000 system diagram (Wang, 2005)	177
Figure A.4	ZOC-33 system diagram (Wang, 2005)	178
Figure B.1	External pressure coefficients, $GC_{pf}$ (Walls)	184
Figure B.2	External pressure coefficients, $GC_p$ (Roofs)	185

## NOMENCLATURE

$B$	Building width (m)
$C_p$	Pressure coefficient
$C_{Pe}$	Exterior parapet surface pressure coefficient
$C_{Pi}$	Interior parapet surface pressure coefficient
$C_{Pr}$	Pressure coefficient on the roof
$\Delta C_p$	Net pressure coefficient on the parapet
$C_{Pe-max}$	Maximum instantaneous pressure coefficient on parapet exterior surface
$C_{Pe-min}$	Minimum instantaneous pressure coefficient on parapet exterior surface
$C_{Pi-max}$	Maximum instantaneous pressure coefficient on parapet interior surface
$C_{Pi-min}$	Minimum instantaneous pressure coefficient on parapet interior surface
$d_p$	Distance between first grid line and solid boundary (m)
$f$	Frequency (Hz)
$G_u$	Gust factor
$GC_{pe}$	Exterior peak parapet surface pressure coefficient
$GC_{pi}$	Internal peak parapet surface pressure coefficient
$H$	Building height (m)
$h_p$	Parapet height (m)
$I$	Turbulence Intensity
$J_e$	Jensen number
$k$	Turbulence kinetic energy ( $m^2/s^2$ )

$k_s$	equivalent sand-grain roughness height (m)
$L$	Building length (m)
$L_x$	Longitudinal scale of turbulence (m)
$m$	Mode
$p$	Static pressure (N/m <sup>2</sup> )
$p_o$	Reference pressure (N/m <sup>2</sup> )
$q_p$	Velocity pressure evaluated at the top of the parapet (N/m <sup>2</sup> )
$R$	Scaling length
$Re$	Reynolds number
$s$	Dispersion
$T$	Time (s)
$U, V, W$	Velocity components along x, y, z directions
$U_g$	Gradient velocity (m/s)
$u^*$	Friction velocity (m/s)
$u'$	Velocity fluctuation
$x$	Distance from the leading corner (m)
$Z^+$	Dimensionless distance
$z$	Height above mean ground level (m)
$z_g$	Gradient height (m)
$z_o$	Aerodynamic roughness height parameter (m)
$\alpha$	Power law exponent
$\varepsilon$	Turbulence dissipation rate (m <sup>3</sup> /s <sup>2</sup> )
$\zeta$	Vertical distance from the base of the parapet (m)

$\theta$	Wind azimuth ( $^{\circ}$ )
$\kappa$	Von Karman constant
$\mu$	Dynamic viscosity of the air (Pa . s)
$\nu$	Kinematic viscosity of the air ( $\text{m}^2/\text{s}$ )
$\rho$	Air density ( $\text{kg}/\text{m}^3$ )
$\sigma_{\theta}$	Standard deviation of wind direction ( $^{\circ}$ )
$\sigma_u$	Standard deviation of wind speed (m/s)

## ABBREVIATIONS

2D	Two Dimensional
3D	Three Dimensional
ABL	Atmospheric Boundary Layer
AIAA	American Institute of Aeronautics and Astronautics
ASM	Algebraic Stress Model
ASCE	American Society of Civil Engineers
ASHRAE	American Society of Heating, Refrigerating and Air-Conditioning Engineers
BAL	Building Aerodynamic Laboratory
BLWT	Boundary Layer Wind Tunnel
BRE	Building Research Establishment
CFD	Computational Fluid Dynamics
CSCE	Canadian Society of Civil Engineers
CVM	Control Volume Method
CWE	Computational Wind Engineering
DSD	Down-Stream Distance
DSM	Digital Service Module
ESDU	Engineering Sciences Data Unit
FS	Full Scale
LES	Large Eddy Simulation
MBMA	Metal Building Manufactures Association

MSC	Meteorological Service of Canada
NBCC	National Building Code of Canada
NIST	National Institute of Standards and Technology
NRC	National Research Center
PVC	Polyvinyl Chloride
RANS	Reynolds-Average Navier-Stocks
RE	Reynolds Equation
RLZ	Realizable
RNG	Renormalization Group
RSM	Reynolds Stress Model
RVM	Random Vortex Method
rms	root mean square
SIMPLE	Semi-Implicit Method for Pressure-Linked Equations
TTU	Texas Tech University
UWO	University of Western Ontario
USD	Up-Stream Distance
USNRC	United States Nuclear Regulatory Commission
WERFL	Wind Engineering Research Field Laboratory
WT	Wind Tunnel
ZOC	Zero, Operate, Calibrate

## *Chapter One*

### **INTRODUCTION**

The majority of structures built all over the world can be categorized as low-rise buildings. An industrial or residential low-rise building can be defined as a structure that has a height to width ratio ( $H/B$ ) of less than unity. Wind loads on low-rise buildings are highly fluctuating and difficult to be determined since such buildings are located in the lower region of the atmosphere where atmospheric turbulence and speed gradients are stronger. The lateral strength of a low-rise building is mainly governed by wind loads rather than the high seismic zones, particularly in zones of severe wind. This type of buildings is more prone to wind damage than other structures (NBCC, 2005). Large part of wind damage to a low-rise building is restricted to the envelope of the building, in particular to roof sheathing.

#### **1.1 Testing of Low-rise Buildings**

Boundary layer wind tunnel experimentation is considered the basic tool of almost all wind engineering studies of wind loads on structures. Wind tunnel enables modeling the complex nature of the wind itself and its interaction with an object. Several wind-tunnel examinations were focused on the evaluation of wind-induced pressures on flat roofs of low-rise buildings, with and without parapets. Current technology shows that most of

these experiments can provide highly reliable results. However, model testing of low-rise buildings has limitations of simulation. Natural wind conditions are simulated by adopting the turbulent boundary layer in wind tunnel; however, the Reynolds numbers in wind tunnel tests are much smaller than those for real buildings.

Recently, Computational Fluid Dynamics (CFD) has the potential to be used for optimization analysis of different building shapes and arrangements. The boundary effects can be avoided with the numerical simulation. However, since wind flow is turbulent and its interaction with buildings is characterized by high Reynolds number of the order of  $10^6 - 10^7$ , numerical calculation for such cases in 3-D is very complicated. Therefore, the application of CFD method is limited and based on many assumptions.

Full-scale testing is the most reliable to obtain wind-measured data, which represents the real life wind loads on buildings and structures. Consequently, in wind engineering research, it is extremely important to conduct field measurements of wind flow on full-scale buildings in order to reveal the real characteristics of both atmospheric surface layer and wind pressures. Such measurements provide data to validate wind tunnel results, to overcome the deficiencies of model-scale testing and to improve the understanding of wind loads acting on structural systems (Mehta, 2004). Reliable full-scale results are also essential for verification and developments of numerical simulation of atmospheric flow around buildings. However, this type of testing is expensive, time consuming and has manpower intensive nature. As a result, limited number of full-scale wind studies was reported, compared to the wind tunnel and numerical ones.

## **1.2 Flat Roofs with Parapets**

Figure 1.1 shows an aerial photograph of buildings in a city center. It is quite clear that the majority of flat-roofed buildings have parapets around them. A parapet is a significant element for any low or high-rise building. Parapets are used for joining of wall and roof membrane in addition to their safety purposes. Many flat or shallow pitch roofs fail near the windward edge in the region of severe local suction. Various solutions, ranging from specialized aerodynamic devices to traditional architectural features, were used in an attempt to reduce these high local roof loads. Parapets are probably the most widely used, they are expected to modify the wind flow over the roof of a building and, thus, change the effective wind loads acting on the roof. Therefore, they are considered the best-documented architectural device for reducing high roof corner and edge loads. Parapets work by lifting the separated shear layer clear off the roof surface, so dissipating the high local edge suctions over a much larger area (Blackmore, 1988). However, the benefits gained by reducing edge loads may be offset by increasing loads on interior regions (Stathopoulos, 1982).

## **1.3 Significance of the Study**

Understanding and defining the wind loads on roof parapets is very important since these loads must be included in the design of the main wind force resisting systems of buildings, in addition to being essential for the design of parapets themselves.

Several previous investigations were focused on how the parapet modifies wind loads on building roofs. However, no study was carried out in an attempt to measure the wind loads on parapets themselves until recently (Stathopoulos et al., 2002-a and 2002-b) due to modeling limitations, as it was very difficult to directly model and record the parapet surface pressures in the wind tunnel. Accordingly, in the past practice, empirical values were suggested based on a rational approach rather than from experimental investigations, due to insufficient research. The ASCE-7 (2005) standards, estimate the wind loads on parapets from pressures measured on the wind-ward wall and the roof of the building in the vicinity of parapets. On the other hand, the NBCC (2005) does not include any recommendations regarding the design wind loads of parapets. The importance of the current study is evolved owing to the lack of guidance provided by code provisions.

#### **1.4 Research Objectives**

The current thesis aims at understanding the flow-pressure mechanism on and around roof parapets and measuring surface pressures on both faces of the parapet in order to determine the design coefficients related to wind loading on parapets. Specific objectives include:

- Evaluate mean and simultaneous peak pressures on both parapet surfaces experimentally.
- Estimate the appropriate loading coefficients used for parapet design based on a comprehensive experimental study.

- Inspect the ability of a CFD code in predicting the wind pressures on building roofs with parapets and on the parapets themselves.
- Provide code provisions with more information regarding the real wind loads on parapets.

### **1.5 Work Methodology**

In order to achieve a precise assessment of the previous objectives, the following path of action is followed:

- Perform a complete field testing using a full-scale low-rise building located in an open area and utilize the data to evaluate wind tunnel results. The experimental building is located at one corner of the soccer field at Loyola Campus, Concordia University, Montreal, Qc. A wooden perimeter parapet is fixed on the building roof with tapping on all its surfaces. The field testing has dealt with extensive measurements of the wind-induced pressures on the roof and the parapet.
- Carry out a detailed wind tunnel investigation, using a scaled model of the experimental building, and investigate the surface parapet pressures as well as roof pressures in the presence of parapet. Using 1:50 length scale, the experimental building model is tested in the wind tunnel of Building Aerodynamics Laboratory of Concordia University.
- Perform a three-dimensional numerical computation, using the CFD code, Fluent 6.1.22, with the RNG  $k-\varepsilon$  model and the RLZ  $k-\varepsilon$  model and compare the results with the experimental data.

- Compare the overall results with the current codes of practice, namely NBCC (2005) and ASCE 7 (2005), and develop a set of design recommendations regarding wind loads on parapets.

### **1.6 Flow Patterns on a Low-rise Building**

At any location on the exterior of a structure, the wind-induced pressures are likely to be highly unsteady and to vary significantly from point to point. This is due to turbulence in flow and turbulence caused by flow separation from the sharp edges of the building (Stathopoulos and Surry, 1981). The scale of the resulting pressure fluctuations must then depend on both the building size and the size of eddies in the oncoming wind. High suctions on roofs are caused by the deflection and acceleration of the wind flow after its separation at the roof edge (Stathopoulos, 1981). Corner areas are particularly susceptible to wind damage and pressures on roofs are a function of wind direction and the highest, i.e. worst, suction (Kind, 1988). At the oblique wind directions, near 45° wind azimuth, strong vortices occur at the upwind roof corners.

Cook, 1985, explained the mechanism of roof edge vortex. Figure 1.2 shows the vortex formation at roof corner and pressure distribution on a building roof. The flow marked 1 separates on the windward edge and tends to be displaced under the flow marked 2 as the flow 2 separates immediately downwind of flow 1. The vorticity of shear layers from 1 adds to that of 2 and this process continues along the roof edges (windward), resulting in a strong conical vortex called the Delta Wing Vortex. These vortices generally occur in

pairs, one on each windward edge of the roof. The center of each vortex is a region of high negative pressure. The pair of vortices produces negative pressure behind each windward edge of the roof.

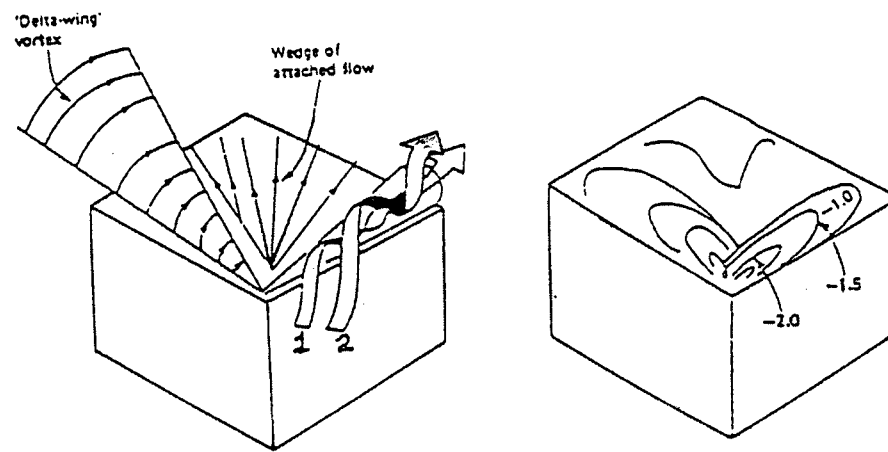
## 1.7 Outline of the Thesis

The current thesis is organized in seven chapters as follows:

- *Chapter two* presents review for the available previous works about wind loading on low-rise building roofs with parapets, in both wind tunnel and full-scale, in addition to the research studies that have simulated wind flow using CFD algorithms.
- *Chapter three* introduces theoretical background of the numerical solution and describes the simulation procedure that has been performed using Fluent code.
- *Chapter four* presents full-scale and wind tunnel experimental work.
- *Chapter five* compares and evaluates the experimental results.
- *Chapter six* evaluates the numerical results
- *Chapter seven* includes conclusions, recommendations and future work.



**Figure 1.1: An aerial view of low buildings in a city center, showing a plethora of parapets**



Flow structure

Pressure distribution

**Figure 1.2: Vortex formation on roof edges (Cook, 1985)**

## *Chapter Two*

### **LITERATURE REVIEW**

Several previous studies focused on the investigations of wind loads on building roofs and the effect of different parapet configurations on these loads. However, due to modeling restrictions, it was very difficult to directly model and record the parapet surface pressures. Therefore, wind loads on parapets themselves had not been examined until recently (Stathopoulos et al, 2002-a and 2002-b). This chapter discusses mainly the experimental studies that dealt with the wind loads on low-rise building roofs with and without parapets, in both full-scale and wind tunnel. Recent investigations that attempt to examine the wind loads on parapets themselves are also discussed. Some previous numerical studies, which utilized CFD to simulate wind flow on and around low-rise buildings, are presented.

#### **2.1 Full-scale Investigations**

Full-scale testing is important to achieve reliable data, which represent the real life wind loads on buildings and structures, and to provide verifications of the wind tunnel results (Mehta, 2004). Over the last four decades, a limited number of full-scale tests are pursued for wind effects on low-rise buildings. Most of full-scale buildings are designed to hold out wind loads using data and principles outlined in national codes of practice,

which almost completely rely upon data from wind-tunnel experiments. Eaton and Mayne (1974) conducted a wind pressure experiment on a two-story building located in Aylesbury, England. The building was 7 m x 13.3 m with a variable roof pitch of 5° to 45° from the horizontal. 72 pressure measuring transducers were used. Wind speed and direction were measured with a 10 m mast at 3, 5 and 10 m height. Wind profile upstream and wind flow in the downstream urban environment were investigated using an anemometer at 20 m mast. Wind tunnel experiments were followed by Sill et al. (1992) at 17 laboratories worldwide using a 1:100 model of the Aylesbury building. Comparison between full-scale and wind tunnel measurements indicated that the traditionally used similarity parameter, Jensen number, is not sufficient to ensure similarity when significant isolated local roughness are presented. Moreover, the variation in pressure coefficients in different experiments is due to the differences in the method of data acquisition and in the measuring point of reference static and dynamic pressures.

Marshall (1975) conducted field experiments on a single-family dwelling in Montana. The dwelling was 6.8 m x 23 m with a wing of 5 m x 5.8 m and roof pitch of 11.5°. The pressure transducers were mounted on the roof surface to avoid penetrating the roof membrane of the house. Wind speed and direction were measured by a prop-vane anemometer at a height of 6.1m. Wind tunnel testing was completed using a model of the same house with scale of 1:50 in order to compare the model results with the full-scale data. The comparison showed that the discrepancy in the results between model and full-scale was perhaps due to inadequate simulation of wind characteristics in wind tunnel.

Marshall (1977) performed another field testing on a mobile home at National Bureau of Standards in Gaithersburg (Maryland). The full-scale dimensions of that home were 3.7 m x 18.3 m and it could be rotated to obtain different wind angles of attack. The anemometers were mounted at a five levels ranging from 1.5 m to 18 m. The surface pressures and the total drag and lift force were measured. The results indicated that negative pressure fluctuations occurred on the end walls and along the perimeter of the roof.

Kim and Mehta (1979) studied the roof uplift loads on a full-scale building at Texas Tech University (TTU). The analysis of spectra of wind speed and wind loads showed peaks and lows at same frequencies. A statistical model was developed from this study which concluded that the fluctuating component of roof uplift is best represented by a Gamma probability density function. Levitan et al. (1986) studied pressure coefficients on the roof of another building at TTU. The study indicated that mean and peak pressure coefficients on the wind-ward roof area are greater for wind azimuth  $\theta = 60^\circ$  than those for  $\theta = 90^\circ$ . Subsequently, the researchers at TTU constructed the Wind Engineering Research Field Laboratory (WERFL) which is a permanent laboratory to study wind effects on low-rise buildings in the field. The building is 9.1 m wide, 13.7 m long and 4 m high with an almost flat roof and it can be rotated in order to allow control over wind angle of attack. The meteorological tower supports wind instruments at six levels: 1, 2.5, 4, 10, 21 and 49 m above the ground. A significant amount of data on winds and surface pressures was collected (Levitan and Mehta, 1992-a and 1992-b).

Mehta et al. (1992) studied the roof corner pressure on the building to obtain baseline data in the field for stationary winds. The largest pressures act along the roof edges while significantly lower pressures occur at the interior taps and at the corner tap. The trends shown in this investigation regarding the roof pressure data are reasonable indicating a degree of validation of the field data. Moreover, Wagaman et al. (2002) studied the separation bubble formed by flow perpendicular to the full-scale TTU building and provided useful information for flow visualization researchers.

The Silsoe Research Institute in England provided useful full-scale measurements on the Silsoe Structures Building. The building was 12.9 m wide, 24.1 m long and 4.1 m high and had a gable roof angle of  $10^\circ$ . The structure consists of seven cold-formed steel portal frames. Hoxey and Moran, 1983, focused on the geometric parameters that affect wind loads on the building. Curved eaves and conventional sharp eaves were tested and the study showed some inadequacy of many national standards for the prediction of loads on low-rise buildings. Robertson (1992) studied the wind-induced response of the Silsoe building in the field. One-hour recordings of free-stream wind pressure, wind direction, external and internal pressures and structural strain were measured under strong wind conditions (8 to 14 m/s). This work provided the details of pressure coefficient information necessary to obtain a specific level of accuracy in predicting wind-induced internal structural loadings (stresses).

Hoxey and Robertson (1994) completed full-scale measurements of surface pressures on the Silsoe Building. They examined methods for analyzing full-scale data to obtain

pressure coefficients. The study shows that the quasi-steady method predicts the maximum pressure exerted on the cladding and these pressures can be averaged over an appropriate area to obtain design cladding loads. Moreover, approximating the non-uniform wind load over a roof slope by an area-averaged pressure coefficient led to acceptable predictions of stresses and deflections.

An experimental low-rise building was built, in 1985, in Concordia University for research dealing with the control of rain penetration through pressurized cavity walls. The building was a small one-room house 3.3 m high, 3.7 m long and 3.2 m wide with sloped roof, which was modified to a flat roof in 1990. It is located in an open area, beside the soccer field of Loyola Campus. Stathopoulos and Baskaran (1990-a) examined the wind pressures on roof corners of that building in the field. A three-cup anemometer and wind vane were mounted on a tower 20 m away from the building and at a height of 4.7 m. The results of the study indicated that very high suctions occur indeed on points very close to the roof corner for oblique wind directions and the comparison with wind tunnel results showed good agreement in terms of mean pressure coefficients.

Maruyama et al. (2004) measured the pressure and flow using a full-scale 2.4 m cube located in an open field. A number of anemometers were arranged on a 10 m high tower around the cube. Wind and pressure data were measured simultaneously. The surface boundary layer develops up to the height of the tower and the cube is well immersed in the turbulent layer. The correlation between the upcoming flow velocities at an upwind

measuring point and the pressures on the cube surface was relatively strong: positive correlation on the wall and negative correlation on the roof.

### **2.1.1 Building roofs with parapets**

Stathopoulos et al. (1999) carried out a field testing on the full-scale experimental building of Concordia University in order to investigate the effect of parapet on roof pressures; which may be considered the only full-scale study regarding roof parapets. The anemometer and vane were located on a tower mounted on the building roof. Field data were compared with wind-tunnel experimentation of the building model with different length scales (Marath, 1992) and with the results of other studies (Figure 2.1).

The full-scale investigation showed that lower parapets which have  $h_p/L < 0.02$  increase the corner suctions and higher parapets ( $h_p/L > 0.02$ ) reduced these suctions, where  $h_p$  is parapet height and  $L$  is the building length. Considering very low parapets,  $h_p/L = 0.008$  and  $0.016$ , roof pressures were found to be more depended on the ratio of parapet height to building height ( $h_p/H$ ). Such study in full-scale provided useful clarification for the previous wind tunnel results regarding the effect of parapet on roof pressures. However, only mean pressures were examined at that stage. It should be noted that the current study is conducted using the same full-scale building after it was relocated to the corner of the soccer field in 2003.

Recently, the researchers at TTU recognized the importance of studying parapet loads in full-scale. Therefore, as part of the NIST project at Texas Tech, a parapet was constructed at the WERFL building (see Figure 2.2). The experiment was intended to examine wind-induced pressures on the inside, outside and top surfaces of the parapet, in addition to the internal pressures inside the parapet section. However, no complete study can be shown until now.

## **2.2 Wind Tunnel Investigations**

The first comprehensive study aimed at defining wind loads on low-rise buildings was performed by Stathopoulos (1979) in the boundary layer wind tunnel of the University of Western Ontario. The parameters examined included building geometry, surrounding terrain, wind direction and building attachments. One of the significant developments in this study was the introduction of a pneumatic averaging system that allowed for the spatial and time averaging of the surface pressures recorded over the surface of the building. This enabled the pressures recorded at each individual pressure tap to be combined at each instant in time to provide a time series of the combined pressures. By doing so, area-averaged loads for areas of various sizes could be accurately determined. The analysis methodology provided in this study is applied to the majority of wind tunnel studies.

The full-scale measurements on TTU building provided a criterion data for verifying wind tunnel experiments and numerical simulations. Surry (1986) compared pressure

measurement results on the full-scale building at TTU with those obtained from a 1:50 scaled model tested in wind tunnel. The study also examined the effect of terrain roughness on mean and peak pressure coefficients. The comparison showed good agreement, however for oblique winds the data indicated significant differences in peak coefficients.

Okada and Ha (1992) tested three scale models of the TTU building, 1:65, 1:100 and 1:150. The comparison shows good agreement in terms of mean wind-pressure coefficients but large differences of rms and peak pressures. The authors concluded that the most important factor regarding these differences was related to the frequency-response characteristics of the pressure-measurement system used in the study.

Cheung et al. (1997) attained good agreement of a 1/10 scale model of TTU building with full-scale results, in which no artificial increase in the longitudinal turbulence intensity was made. The authors suggested that the increased Reynolds number was believed to play a significant part in their achievement.

Ham and Bienkiewicz (1998) performed a study of approach wind flow and wind-induced pressure on a 1:50 geometrical scale model of TTU building at Colorado State University. The physical simulation technique developed using conventional wind tunnel devices led to a very good representation of the TTU nominal flow. This agreement was attributed to improved modeling of approach flow and relatively high frequency response of the pressure measuring system.

Tieleman et al. (1998) interested in the effect of the different flow parameters on the observed pressure coefficients, they compared the full-scale data collected from TTU laboratory with results of mean, rms, and peak pressure on the roof of a 1:50-scaled model of the same building. The authors stated that the reproduction of the horizontal turbulence intensities and their small-scale turbulence content in the wind tunnel is very important for the possibility of agreement between model and field roof pressure coefficients.

Tieleman et al. (2008) represented the distributions of peak suction forces in separation regions on a surface-mounted prism by Gumbel distributions, using the field and laboratory data of the WERFL of TTU. The authors stated that wind engineers must realize that wind tunnel experiments of the atmospheric flows never duplicate the non-stationary conditions that occur in the atmosphere. Consequently, the peak distributions obtained over a long period with the method of moments exhibit much greater dispersion of the peaks than the distributions obtained over a much shorter period with the Sadek–Simiu (2002) procedure.

Full-scale testing of the Silsoe Building provides an opportunity to undertake detailed full-scale/model scale wind pressure comparisons. Richardson and Surry (1991 and 1992) performed wind tunnel model of scale 1:100 for the building. Collaborative research with the Boundary Layer Wind Tunnel Laboratory of University of Western Ontario was conducted. The comparisons of wind tunnel results with the obtained full-scale data showed that very good agreement is possible between full and model-scale

data. However, the model-scale underestimates the suction significantly where the separation occur on the wind-ward roof slope.

Richards et al. (2007) reported a wind-tunnel modeling of the Silsoe 6 m Cube at the University of Auckland. The approach taken in this study was to match the velocity profile and the high-frequency turbulence as closely as possible. Similar mean pressure distributions were obtained as a result. In addition, reasonable agreement is obtained by expressing the peak pressure coefficient as the ratio of the extreme surface pressures to the peak dynamic pressure observed during the run.

Lin et al. (1995) proved experimentally that corner vortices for both smooth and boundary layer flow dominate the absolute suction pressures coefficient,  $C_p$ , while their effects are dramatically reduced with increasing distance from the leading corner and with increasing tributary area. The relationship between the effective load and tributary area is insensitive to the building dimensions if area is normalized by  $H^2$  where  $H$  is the building height (Lin and Surry, 1998) and it is only slightly dependent on the shape of the areas that include the corner point. In this region, loads reduce rapidly with increasing tributary area. The authors used simultaneous time series of pressures measured at locations within the corner region to form new time series of uplift loads by instantaneous spatial averaging, for various building heights and plan dimensions.

Kawai (1997) also investigated the structure of conical vortices on a flat roof in oblique flow by hot-wire velocity measurements in smooth and turbulent one. The author stated

that the strength of the conical vortices was larger in the smooth flow than in the turbulent flow. Consequently, the larger mean suction acted on the roof in smooth flow, and each conical vortex grew and decayed alternatively to produce imbalance in the suction distribution.

Uematsu and Isyumov (1998) provided an empirical formula for estimating the minimum pressure coefficient in the leading edge and corner regions which could be applied to buildings with roof pitches larger than approximately 4:12. In the leading edge and corner regions, where severe suctions occurred, the effect of time average on the peak pressure was related to that of spatial average through the equivalent length and the square root of the area. The analysis of wind effects on design (Kasperski, 1996), taking into account a characteristic load combination of at least dead load, showed that final design was based on a negative wind-induced bending moment in the downwind frame corner for many practical cases.

### **2.2.1 Wind loads on roofs with parapets**

Leutheusser (1964) carried out the first detailed study regarding the effect of parapets on the wind loads of flat roofs under uniform conditions. The author believed that, for oblique wind directions, the parapets cause an extreme reduction of the high suctions particularly at the corners and edges of the roof. Furthermore, the presence of parapets made the roof pressure distribution more uniform but it did not affect the magnitude of the average roof pressure coefficient and the pressure distribution over the building

sidewalls. However, the study was carried out in uniform flow conditions and the mean velocity and turbulence intensity profiles found in natural wind were disregarded, thus the above results may not be representative of turbulent flow conditions. Subsequently, Columbus (1972) studied the effect of parapets considering turbulent, in addition to uniform flow conditions. However, the study shows that parapets do not cause any reduction on local mean pressures in turbulent flow in contrast to the case of uniform flow.

Kind (1974) studied the gravels blown off rooftops and found that the critical wind speeds increase with increasing parapet height. This indicates that parapets reduce the pressure coefficients on the roof. On the contrary, Davenport and Surry (1974) indicated that local mean suctions are increased when the parapet is added, particularly for oblique wind direction. Kramer (1978) suggested that parapet height significantly affect the corner roof pressures. For the case of  $h_p/B > 0.04$ , where  $h_p$  is parapet height and  $B$  is building width, corner pressures were reduced by 70 %. Consistent with that results, Sockel and Taucher (1980) concluded that when  $h_p/H = 0.2$ , where  $H$  is building height, the mean suction pressures at the roof corner were reduced by 50 %. Also, parapets act to reduce the fluctuating pressure components.

A systematic approach was followed by Stathopoulos (1982) to clarify the effect of parapets on flat roof pressures of low-rise buildings as well as to inspect the discrepancies that were found between some authors. The study concluded that the addition of parapets around the roof causes a reduction of the roof-edge local suction by 30%, these suctions

slightly increase on the interior roof. On the other hand, parapets tend to increase the mean local suction and positive peak and mean pressure coefficients as well, particularly at the corner areas. Root mean square (rms) pressure coefficients show little changes in the building with parapets. The study has recommended specifications to the NBCC regarding the wind loads on low-rise buildings with parapets.

Lythe and Surry (1983) performed a comprehensive research examining a number of parapet and building heights in order to study the effects of parapets on wind load distribution on roofs. The study showed that:

- The distribution of loads on a roof consists of a very highly loaded corner region, a highly loaded edge region and a more moderately loaded interior region.
- Edge region width is increased with building height and by the addition of parapets.
- Corner region width remains nearly constant with building height except for cases of very high parapets.
- Corner region mean and peak pressures increase on low buildings with low parapets but decrease otherwise.

An investigation of wind-induced failure of various roofing systems was carried out by testing different building shapes, each with a number of different parapet heights (Kind, 1986); and followed by pressure measurements on two small low-rise building models in a relatively thick boundary layer, with pressure taps very close to the roof edges (Kind, 1988). The author found that increasing parapet height leads to a decrease of worst

suction coefficients. Moreover, worst suctions on flat-roofed low-rise buildings were only mildly sensitive to the characteristics of the approach-flow boundary layer.

Stathopoulos and Baskaran (1988-a, 1988-b and 1988-c) produced a series of articles clarifying the effect of parapets on local surface pressures (see Figure 2.3). Such study examined the effects of building height, ranging from 12 to 145 m, and large range of parapet heights including low parapets (0-3 m) on both local and area-averaged roof pressures for a variety of wind directions. The effect of one-side parapet, such as billboard, on the roof corner pressures was also examined. However, the building tested in this case is a high-rise building, with height  $H = 96$  m. The conclusions of these studies could be summarized as follows:

- Parapets do not affect roof interior wind loads.
- Low parapets (<1.0 m) reduce local high suctions on roof edges by 30 %, increase them on roof corners by 100 % and increase area-averaged loads on roof corners by 20 %.
- High parapets (>1.0 m): reduce local high suctions on roof edges by 15 % and increase these suctions on roof corners by 50 %.
- One-side parapets induce higher mean and peak local suctions at roof corners, even for high parapets, in comparison with perimeter parapets.

Kareem and Lu (1992) studied the mean and fluctuating pressure distributions on the roof of a square cross-section building with adjustable height. Measurements were done in two terrains representing open country and urban flow conditions. Perimeter parapet

walls of two different heights were introduced. Parapets were found to reduce peak suction pressure. In agreement with Kind (1988) the effectiveness of perimeter parapets in reducing suction pressure coefficients increased by increasing their height.

Badian (1992) carried out wind tunnel experiments in order to evaluate the wind loads on flat roof edges and corners on buildings with parapets, the models were tested with high number of taps distributed on one corner and along its adjacent edge. The study confirmed that parapets generally reduced the high suction on the roof edges. Furthermore, parapets with a height of 1.0 m or lower increased peak and mean pressures for low buildings.

Bienkiewicz and Sun (1992) performed fundamental studies of wind loading on the roof of a 1/50-scaled model of the TTU test building with some parapet heights. The presence of low parapets ( $h_p/H < 0.04$ ) results in an increase in the overall maximum mean and peak suction. Moreover, high parapets ( $h_p/H > 0.08$ ) reduce both values. The researchers believed that parapets are very useful in reducing high pressures created at roof corners and edges. Nevertheless, the height and shape of parapets significantly affect this reduction. Therefore, some studies were interested in examining different parapet configurations.

Surry and Lin (1995) investigated the sensitivity of high suction near corners to the use of relatively minor alterations to the roof corner geometry. Different parapet configurations were used as a modification to the roof corners. The study shows that:

- Porous parapets leading to a reduction of the high suctions of up to 70 % near the corner.
- For the saw-tooth partial parapets, the high suctions near the corner observed are reduced by up to 40 %.
- Reductions of about 60 % in the high suction magnitude are also reached near the corner, for the rooftop splitter configurations with the porous splitters being slightly better than the solid ones.

Mans et al. (2003) have also studied the effect of a single parapet (above only one wall) on local roof pressures near the leading corner of a low-rise building. The study focused on a comparison of the results with those previously obtained for a continuous parapet. The results of this study agreed with the conclusion of Baskaran and Stathopoulos (1988-b) and indicated that isolated parapets, regardless of height, generate larger suction pressures on the roof surface in comparison to a continuous parapet and to the case of no parapet, with regards to low-rise buildings. In contrast, tall continuous parapets ( $h_p/H > 0.4$ ) may reduce the corner suction pressures, which agreed with Stathopoulos and Baskaran, 1988-c.

Pindado and Meseguer (2003) examined different parapet configurations, including non-standard configuration (cantilevered parapets), to reduce the wind suctions generated on the roofs by conical vortices. This study demonstrated that low-height parapets ( $h_p/H < 0.05$ ), where  $h_p$  is parapet height and  $H$  is building height, with medium porosity are more

efficient than solid parapets. Also, low-height cantilevered parapets ( $h_p/H < 0.031$ ) produced a very effective reduction more than vertical parapets, either solid or porous.

### **2.2.2 Wind loads on parapets themselves**

The first investigation for the wind loads on parapets themselves was performed by Stathopoulos et al. (2002-a). Due to modeling limitations, no study previously attempted to directly model and record the parapet surface pressures. Instead, in past practice the wind loads on the parapet were estimated from pressures measured on the wall and roof of the building in the vicinity of the parapet. In this case, it was assumed the pressures on the front wall surface are equivalent to the external parapet surface pressures and the interior parapet surface pressures are identical to the roof edge pressures. This assumption does not take into consideration the differences between roof edge/corner suctions and those on the inside surface of the parapet. Therefore, the primary focus of the study was to determine the validity of this estimation method. The study concluded that parapet design loads obtained by applying the National Building Code of Canada (NBCC, 2002) for windward wall and roof region were significantly higher than actual loads on the tested parapet. However, the dimensions of the modeled building ( $L/H = 1$  and  $L/H = 2$ , where  $L$  is building length and  $H$  is building height) classify it more as an intermediate-rise building rather than a low-rise building.

Subsequently, Stathopoulos et al. (2002-b), performed an experimental study to determine wind pressure coefficient appropriate for the design of parapets for low-rise

buildings ( $L/H = 3$ ). The study focuses on measuring the surface parapet pressures simultaneously in order to investigate the combination effect of parapet surface loads. The comparison of the results with the ASCE 7-02, provisions shows that the latter to be on the conservative side for all cases.

A study was completed by Mans et al. (2005) in order to analyze wind-induced pressures on parapets of low-rise buildings. In agreement with Stathopoulos et al. (2002-a) the authors found that evaluation of parapet loads, using pressures recorded on the wall and roof in the vicinity of a parapet; overestimates the measured parapet loading by approximately 10 %.

### **2.3 Numerical Computations**

Many studies previously attempted to simulate wind flow on and around structures by means of numerical algorithms (Computational Fluid Dynamics, CFD) in order to predict different wind parameters. Hanson et al. (1984) examined the possibilities of developing a numerical model to simulate wind flow around buildings. The study used both the Random Vortex Method (RVM) and the Control Volume Method (CVM). The results were not compared with experimental data. However, significant contribution was made to demonstrate the advantages of CVM over RVM. The latter was found not compatible with turbulence models and inefficient in predicting wind flow around three-dimensional sharp edge buildings.

Paterson (1986) attempted to solve the Reynolds Equation (RE) using the standard  $k-\varepsilon$  turbulence model developed by Launder and Spalding (1974). The author employed the CVM to discretize the RE. The computed results were compared with different wind tunnel and full-scale measurements. However, the recirculation zone and the pressure on the building sides were not acceptable for all cases. It was included that the predicted parameters need improvements particularly at separation zone and in the wake.

Murakami and Mochida (1988) computed the steady wind conditions around a cubic model using the standard  $k-\varepsilon$  model. The study revealed that the numerical evaluation of wind pressures on flat roofs of rectangular buildings is very complex. Murakami (1990) attempted the numerical simulation of the airflow around a cube for unsteady flow using the standard  $k-\varepsilon$  model for turbulence. The author concluded that the  $k-\varepsilon$  model with a fine mesh can reproduce mean velocity field and mean pressure field more accurately than a coarse mesh compared with wind tunnel results. However, significant differences were observed in the distribution of the turbulent energy around the windward corner and in the wake (see Figure 2.4).

Stathopoulos and Baskaran (1990-b) evaluated wind effects around buildings through an individually developed code. In order to improve the results of standard  $k-\varepsilon$  model in predicting recirculation and separation regions, two simple modifications were applied to the calculations, namely, a streamline-curvature correction and a preferential-dissipation correction. A new zonal-treatment procedure was developed to link the solid boundary nodes with the computational domain for the turbulence variables ( $k$  and  $\varepsilon$ ).

In 1992, Murakami analyzed velocity-pressure fields and wind-induced forces on and around a building model, and compared the results with those from the wind tunnel. The study confirmed that the results of the 3D computation match well to the experimental data, while 2D results include significant discrepancies. More detailed time-averaged flow fields around a cube within a surface boundary layer using three types of well known turbulence models, namely the  $k-\varepsilon$  eddy viscosity model, the Algebraic Stress Model (ASM) and the Large Eddy Simulation (LES) model, were given by Murakami et al. (1992). The model equations used for ASM were based on the methods of Rodi, 1976, and Gibson and Launder, 1978, except for the treatment of the wall reflection term (Murakami et al. 1990). The accuracy of these simulations was assessed by comparison with results from wind tunnel tests. LES results show the best agreement with the experimental data. Standard  $k-\varepsilon$  model overestimates the kinetic energy around the leading edge of the building and thus it underestimates both the length and height of the recirculation zone on the top of the building. However, some modified  $k-\varepsilon$  models can overcome this drawback.

Selvam (1992) simulated the three-dimensional wind flow around the TTU building model using  $k-\varepsilon$  model. The computational data with staggered grid arrangement agreed well with the experimental results. However, the numerical results from the non-staggered grid failed to predict the roof pressures. In addition, Selvam (1997) used LES to solve the Navier-Stokes equations for wind flow around the TTU building. The computed mean pressures were in good agreement with field measurement results. However, the peak pressures were much higher than the field data.

Stathopoulos and Zhou (1993) proposed a two-layer methodology combining the  $k-\varepsilon$  model in the external flow region with either a one-equation model (Norris and Reynolds, 1975), or a modified  $k-\varepsilon$  model, in the near wall area. This two-layer method based on the one equation model was found effective in predicting the separation above the roof surface and near the side walls of a cubic building.

He and Song (1997) also, simulated the wind flow around the TTU building and roof corner vortex using LES method. The authors stated that the three-dimensional roof vortex model was in good agreement with wind-tunnel and full-scale results.

A systematic investigation of numerical effects on the computation of turbulent flows over a square cylinder has been made by Lee (1997). The author found that some conventional  $k-\varepsilon$  models may give reasonable prediction when proper numerical parameters are included.

Meroney et al. (1999) compared recirculation zones around several building shapes using standard  $k-\varepsilon$  model, RNG  $k-\varepsilon$  model and Reynolds Stress Model (RSM) using Fluent 4.2.8. All constants in these turbulence models are default values. The authors stated that the RSM provides a more accurate flow field than both types of  $k-\varepsilon$  models. Also, the results showed that pressure coefficients on the front, back and rooftop can be predicted very well when compared with experimental data, although recirculation zones around the building were not reproduced accurately. However, no explanation was

provided regarding this good agreement of pressure coefficients and bad agreement of flow field with the experimental data.

Chang and Meroney (2003) investigate the sensitivity of high roof suctions to the presence of surroundings using Fluent code with  $k-\varepsilon$  model. The overall numerical results appear similar to the experimental data of a 1/50 scale model of TTU building. However, the numerical results of the front edge region at flow separation indicate higher suction.

In order to improve the overestimated kinetic energy around the leading edge of the building by the standard  $k-\varepsilon$  model, Gao and Chow (2005) proposed a method to change the speed distributions around the sharp corner of the building. By limiting the longitudinal velocities in the first cell adjacent to the sharp edge of the cube and making good use of the wall functions at the intersection cells of the velocity components. In this case, the positions of maximum turbulent kinetic energy and the flow separation and reattachment could be predicted by the standard  $k-\varepsilon$  model.

Zang and Gu (2008) used a revised  $k-\varepsilon$  model by Re-Normalizing the Group of equations (RNG  $k-\varepsilon$  model) to solve the RANS equations, in order to investigate the wind-induced interference effects on the pressure distributions on a building adjacent to another one in staggered arrangement. The numerical results were in qualitative agreement with the experimental data. The author also confirmed that the RNG  $k-\varepsilon$  model seems to be a useful tool for predictions of wind pressures.

Based on the previous survey, the expected flow stream lines around the current test building with the parapet are presented in Figure 2.5.

#### **2.4 Current Wind Loading Standards Regarding Parapets**

Wind standards and codes provide very little guidance regarding the wind loading on parapets, or their influence on the local (cladding and component) loads. Moreover, their recommendations are based on a rational approach and do not come from experimental research. Defining a wind loading standard to be used in the design of low-rise buildings requires a consideration of many parameters, including building geometry, surrounding terrain and wind direction. Thus, experimental studies for evaluating parapet loads become a primary task for the researchers in this area. Although, the standards do consider how the loading on the parapet itself may affect the roof surface pressure coefficients, they do not consider wind loads on parapets themselves.

The ASCE 7-02 considered the importance of the design wind loads of parapets. In the absence of research, a design method in the wind load section uses wall pressures for the outside surface of the parapet and roof edge/corner suctions for the inside surface in order to estimate the total drag force on the parapet, as shown in Figure 2.6. This method may be conservative since it does not consider the lack of simultaneous occurrence of maximum pressure value on the outside surface and the maximum suction on the inside surface of the parapet on the windward side of a roof (Stathopoulos et al., 2002-b).

For the design of the main structural system the ASCE 7-02 (2002) standard recommends net coefficients ( $GC_p$ ) of + 1.8 and - 1.1 for the windward and leeward parapets, respectively. However, after completion of preliminary work on which the present study is based (Stathopoulos et al., 2002-a and 2002-b), these values were revised in the ASCE 7-05 version to + 1.5 and - 1.0. With regards to the loads on the component and cladding, ASCE 7-05 recommends  $GC_p$  values of + 3.8 and - 2.4 for windward and leeward parapets, respectively, at corner region and + 2.8 and - 2.2 for mid-span location. Appendix B includes the ASCE 7-05 recommendations, as written in the standard.

NBCC (2005) does not provide explicit recommendation regarding wind loads on parapets. However, a similar procedure with that of the ASCE 7-05 can be used.

## **2.5 Summary**

The main points concluded in this chapter can be summarized as follows:

- Peak suction pressures occur at the leading corner of the building, where the flow separates from the building roof creating two vortices. These pressures reduce significantly with increasing distance from that corner. The worst angle of attack is generally between  $30^\circ$  and  $60^\circ$  from the normal extending of one face of the building.
- Large differences have been recorded for root mean square (rms) and peak pressure values particularly near roof corners. These differences were due to inequality in tap diameter, edge geometry, turbulence scale or Reynolds number, in addition to

the corner vortex development or the presence of convective and non-stationary effects in full-scale.

- Regarding the effect of parapet on roof pressures:
  - The addition of parapets around the building roofs reduces the high suction pressures on roof corners (Leutheusser, 1964; Kind, 1974; Stathopoulos, 1982).
  - The presence of parapets made the roof pressure distribution more uniform (Leutheusser, 1964; Lythe and Surry, 1983; Baskaran and Stathopoulos, 1988).
  - Parapet heights significantly affect roof corner pressures: the addition of relatively high parapets ( $h_p > 1$  m) reduces the high suction pressures on roof edges and corners, on the other hand, low parapets ( $h_p < 1$  m) may increase these pressures (Kramer 1978; Sockel and Taucher, 1980; Kind, 1988; Kareem and Lu, 1992; Stathopoulos and Baskaran, 1987; Badian, 1992; Bienkiewicz and Sun; Mans, 2003).
  - Various parapet configurations were examined as in order to effectively reduce the corner suction pressures (Stathopoulos and Baskaran, 1988; Surry and Lin, 1995; Pindado and Meseguer, 2003; Mans et al., 2003)
  - Some discrepancies exist between authors as they considered that parapets do not cause any reduction in roof mean pressures (Columbus, 1972) or that the addition of parapets increases the local mean suction on building roofs (Davenport and Surry, 1974).
- The few studies that dealt with the wind loads on the parapet itself provided very useful information; however, only limited wind tunnel investigations were completed. These studies concluded that code provisions may be conservative in

predicting parapet design loads (Stathopoulos et al., 2002-a and 2002-b; Mans et al., 2005).

- No previous full-scale study was attempted to measure the real wind-induced pressures on parapets.
- With regard to the numerical computational studies:
  - The standard  $k-\varepsilon$  model overestimates the kinetic energy around the leading edge of the building and thus it underestimates both the length and height of the recirculation zone on the top of the building.
  - Several modified  $k-\varepsilon$  models have been proposed to overcome significant errors such as overestimation of turbulence kinetic energy  $k$ , results in the standard  $k-\varepsilon$  model. These modified models accurately estimate the flow separation and reattachment to the roof
  - Theoretically, non-linear models such as LES and RSM are more accurate than linear models ( $k-\varepsilon$  models); therefore such models are recommended, although they still require some improvements. However, these methods apply to unsteady-state large scale motion of turbulent flow and need finer grid arrangement, i.e. more computational resources, compared to  $k-\varepsilon$  method.
  - Some attempts were made in order to compute peak pressures on different building by means of non-linear models. However, these pressures were not predicted reliably.

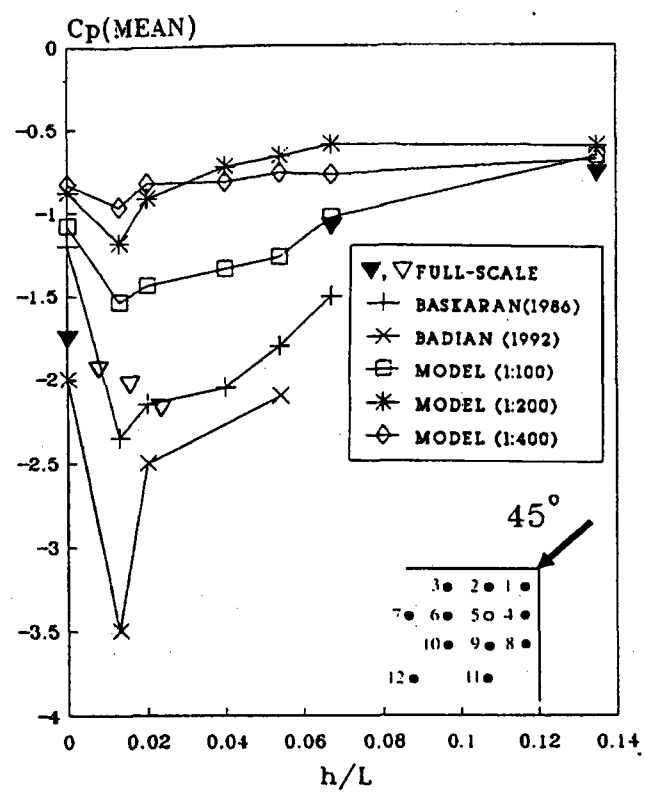
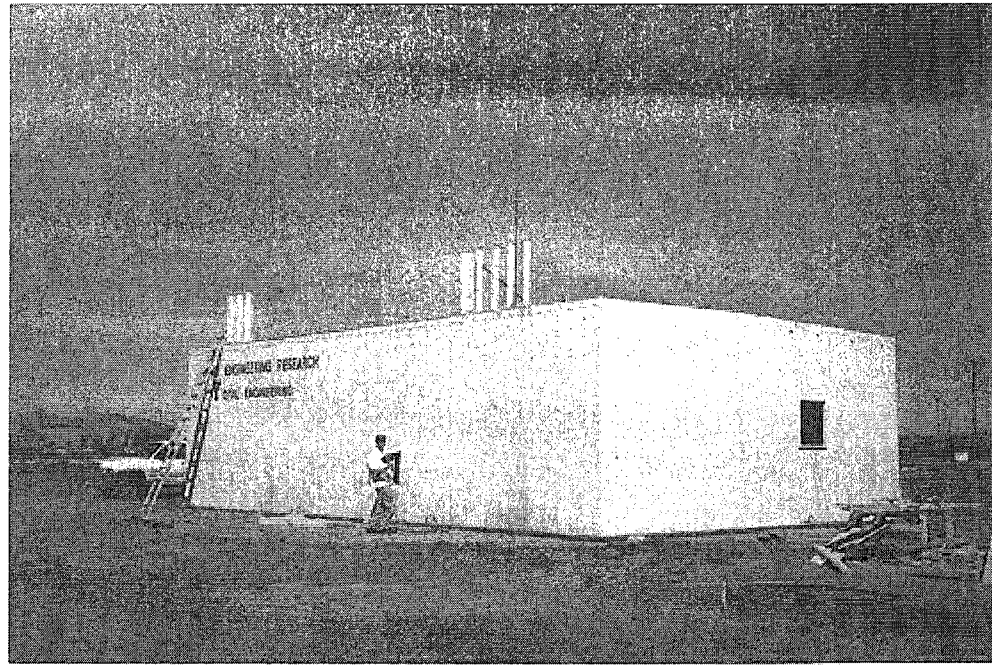


Figure 2.1: Corner mean pressure coefficients in terms of  $h_p/L$

(Stathopoulos et al., 1999)



**Figure 2.2: Parapet wall at the WERFL of TTU  
(parapet under construction, 2004)**

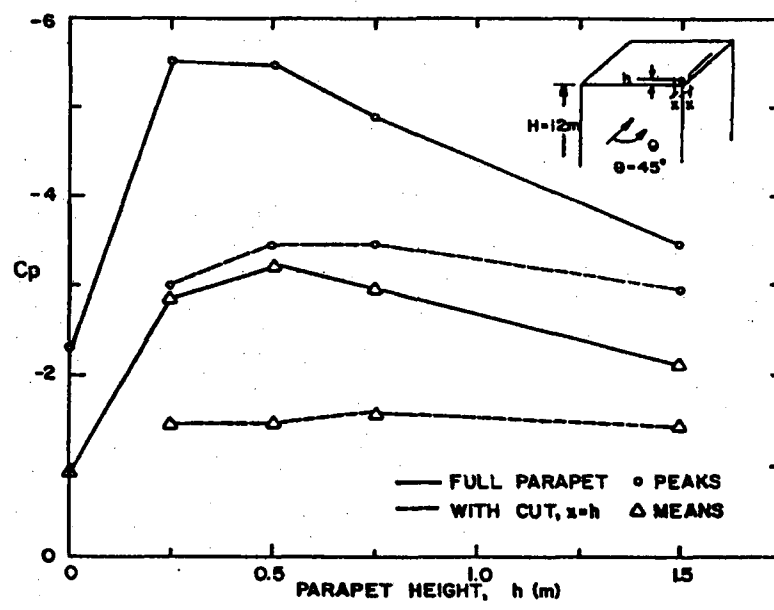


Figure 2.3: Roof corner pressure coefficients for cut-parapet configurations

(Stathopoulos and Baskaran, 1988-b)

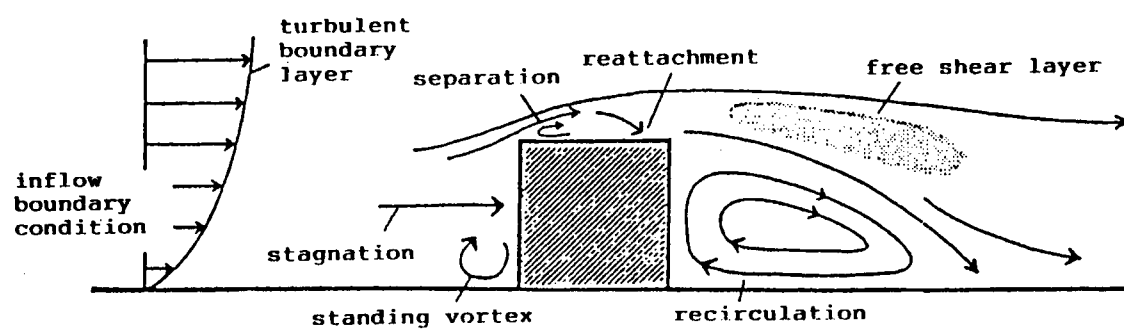
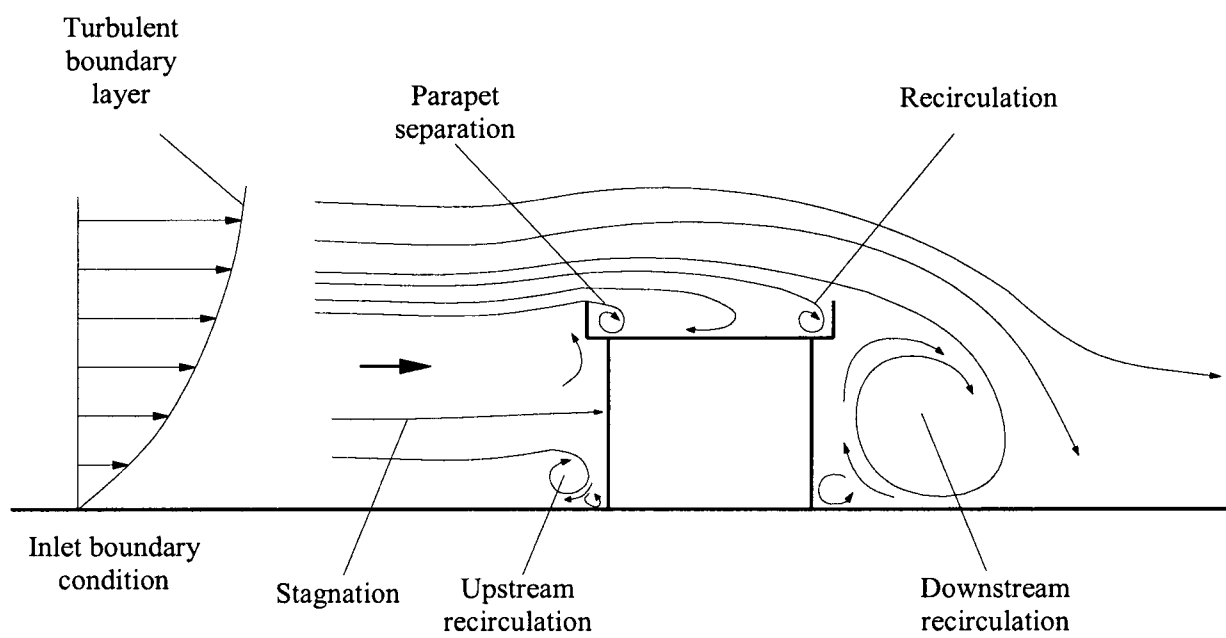
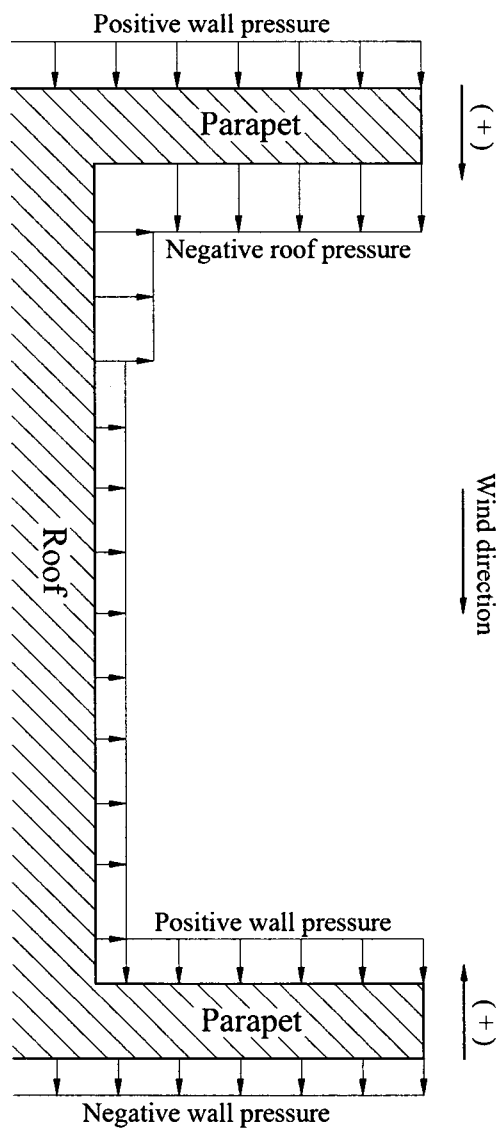


Figure 2.4: Turbulent air flow field around a cube (Murakami, 1990)



**Figure 2.5: Mean stream lines expected around the center line of the current building**

**Figure 2.6: Assumed load acting on the parapet (ASCE-7, 2005).**



## *Chapter Three*

### **NUMERICAL SIMULATION**

Accurate computer predictions are very useful since numerical methods can be less expensive and less time consuming than comparable field or wind tunnel testing. Numerical simulation of wind flow over the test building model with parapets is performed using the commercial Computational Fluid Dynamics (CFD) code Fluent 6.1.22. The steady-state Reynolds-Averaged Navier-Stokes (RANS) equations are solved using modified  $k-\varepsilon$  turbulence models. This chapter presents the numerical simulation procedure and explains the revised turbulence models that were used. The computation has been conducted for wind flow perpendicular to the building face (i.e. zero wind azimuth). Three-dimensional calculations of air flow are essential to obtain accurate results for flow simulation around buildings. The numerical simulation was adopted for the same configurations of the building model; thus wind flow characteristics for the wind tunnel are used.

#### **3.1 Introduction to Fluent**

Fluent is based on a finite-volume discretization of the equations of motion and is utilized for modeling fluid flow and heat transfer in complex geometries. Fluent can identify key areas of the flow such as building geometries, stack configurations and incident flow

combinations which create areas of flow (Flowe and Kumar, 2000). A complete description of the code, many validation examples, and a number of published papers and reports may be found on the web at <http://www.fluent.com>. The program provides complete mesh flexibility, solving flow problems with unstructured meshes. Fluent package consists of many tools for defining a separate flow problem, setting boundary and initial conditions and solving a set of complex equations for conservation of mass, momentum and energy. A steady-state Reynolds averaged turbulence model,  $k-\varepsilon$ , has been used. Therefore, the output of the computation consists only of mean values.

### 3.2 Governing Equations

The governing equations of incompressible turbulent wind flow around a bluff body are the Continuity equation and the steady-state Reynolds-averaged Navier-Stokes (RANS) equations:

$$\frac{\partial U_j}{\partial x_i} = 0 \quad 3.1$$

$$\frac{\partial}{\partial x_j} (\rho U_j U_i) = -\frac{\partial p}{\partial x_i} + \frac{\partial}{\partial x_j} \left[ \mu \left( \frac{\partial U_i}{\partial x_j} + \frac{\partial U_j}{\partial x_i} \right) - \overline{\rho u_i u_j} \right] \quad 3.2$$

where:  $i, j = 1, 2, 3$ ,  $U$  and  $u'$  are mean and fluctuating velocity, respectively,  $\rho$  is air density,  $\mu$  is the dynamic viscosity and  $p$  is the mean pressure. The conservative general form of all flow equations under steady state conditions, including equations for the scalar quantities such as  $k$  and  $\varepsilon$ , when derived for a flow property,  $\phi$ , which represents the unknown variables ( $u, p, etc.$ ), can be expressed in the following form:

$$\underbrace{\frac{\partial(\rho U\Phi)}{\partial x} + \frac{\partial(\rho V\Phi)}{\partial y}}_{\text{Convection terms}} = \underbrace{\frac{\partial}{\partial x} \left[ \Gamma \frac{\partial\Phi}{\partial x} \right] + \frac{\partial}{\partial y} \left[ \Gamma \frac{\partial\Phi}{\partial y} \right]}_{\text{diffusion terms}} + \underbrace{S}_{\text{source term}} \quad 3.3$$

Equation 3.3 is known as Transport equation and is used as the starting point for computational procedures in finite volume method for developing CFD codes. The key step is integrating Transport equation over a three-dimensional control volume.

For the continuity equation (3.1):  $\Phi = 1$ ,  $\Gamma_\phi = 0$  and  $S_\phi = 0$

For the momentum equation (3.2):  $\Phi = U_i$ ,  $\Gamma_\phi = (\mu + \mu_t)$  and  $S_\phi = \frac{\partial}{\partial x_i}(-P)$

### 3.3 Turbulence Models

There are many types of turbulent models utilized in CFD codes. Fluent provide different turbulent models, which explained in detail in Fluent 6.1.22 User's Guide (2005), Volume-2. Three types of kinetic energy-dissipation rate ( $k$ - $\varepsilon$ ) models are described below namely: the Standard  $k$ - $\varepsilon$  model, the Realizable (RLZ)  $k$ - $\varepsilon$  model and the Renormalization Group Theory (RNG)  $k$ - $\varepsilon$  model. A major difference between these models is the method of calculating turbulent viscosity. The current simulation uses both RLZ  $k$ - $\varepsilon$  and RNG  $k$ - $\varepsilon$  models since the standard  $k$ - $\varepsilon$  model was found not effective in predicting the recirculation zones accurately.

### 3.3.1 Standard $k$ - $\varepsilon$ model

The standard  $k$ - $\varepsilon$  model includes some simplifying assumptions, such as a turbulent equilibrium assumption near the wall and the use of various constants in the turbulent transport equations. Due to these assumptions, the model needs the least computer resources comparing with the other models. However the validity of such method is limited. The turbulent kinetic energy ( $k$ ) and its dissipation rate ( $\varepsilon$ ) are obtained from the following transport equations (Launder & Spalding, 1972):

$$\rho \frac{Dk}{Dt} = \frac{\partial}{\partial x_i} \left[ \left( \mu + \frac{\mu_t}{\sigma_k} \right) \frac{\partial k}{\partial x_i} \right] + G_k - \rho \varepsilon \quad 3.4$$

$$\rho \frac{D\varepsilon}{Dt} = \frac{\partial}{\partial x_i} \left[ \left( \mu + \frac{\mu_t}{\sigma_\varepsilon} \right) \frac{\partial \varepsilon}{\partial x_i} \right] + C_{1\varepsilon} \frac{\varepsilon}{k} G_k - C_{2\varepsilon} \rho \frac{\varepsilon^2}{k} \quad 3.5$$

where:  $\mu_t = \rho C_\mu \frac{k^2}{\varepsilon}$  ,  $G_k = -\overline{\rho u_i' u_j'} \frac{\partial U_j}{\partial x_i}$  representing the generation of turbulent

kinetic energy due to the mean velocity gradients.

### 3.3.2 Realizable $k$ - $\varepsilon$ model (RLZ)

To improve the simulation results of the standard  $k$ - $\varepsilon$  model for cases in which the flow includes strong streamline curvature, vortices and rotation, Shih et al. (1995) applied some modifications, which include making  $C_\mu$  variable and adding a new equation for  $\varepsilon$  based on the dynamic equation of the mean square velocity fluctuation. This modified

model called Realizable  $k$ - $\varepsilon$ . The dissipation equation in this model represents, very well, the spectral energy transfer. Meanwhile, the destruction term does not have any singularity even if  $k$  vanishes or becomes negative. Shih et al. (1995) found that the RLZ  $k$ - $\varepsilon$  model performs well, comparing to the standard  $k$ - $\varepsilon$  model, for a variety of flows including the recirculation in the wake. The transport equations for this model can be obtained as follows:

$$\rho \frac{Dk}{Dt} = \frac{\partial}{\partial x_i} \left[ \left( \mu + \frac{\mu_t}{\sigma_k} \right) \frac{\partial k}{\partial x_j} \right] + G_k - \rho \varepsilon \quad 3.6$$

$$\rho \frac{D\varepsilon}{Dt} = \frac{\partial}{\partial x_j} \left[ \left( \mu + \frac{\mu_t}{\sigma_\varepsilon} \right) \frac{\partial \varepsilon}{\partial x_j} \right] + \rho C_1 S \varepsilon - \rho C_2 \rho \frac{\varepsilon^2}{k + \sqrt{\nu \varepsilon}} \quad 3.7$$

where:  $C_1 = \max \left[ 0.43, \frac{\eta}{\eta + 5} \right]$ ,  $\eta = S \frac{k}{\varepsilon}$ ,  $S = \sqrt{2S_{ij}S_{ij}}$ ,

$$C_2 = 1.9, \sigma_k = 1, \sigma_\varepsilon = 1.2.$$

### 3.3.3 RNG $k$ - $\varepsilon$ model

The RNG  $k$ - $\varepsilon$  model used in Fluent is based on a mathematical technique called Renormalization Group. Choudhury, 1993, provided more detailed description of RNG theory and its application to turbulent flow. The transport equations have a similar form as those of the standard  $k$ - $\varepsilon$  model and can be written as follows:

$$\rho \frac{Dk}{Dt} = \frac{\partial}{\partial x_i} \left( a_k \mu_{eff} \frac{\partial k}{\partial x_j} \right) + G_k - \rho \varepsilon \quad 3.8$$

$$\rho \frac{D\varepsilon}{Dt} = \frac{\partial}{\partial x_i} \left( a_\varepsilon \mu_{eff} \frac{\partial \varepsilon}{\partial x_j} \right) + C_{1\varepsilon} \frac{\varepsilon}{k} G_k - C_{2\varepsilon} \rho \frac{\varepsilon^2}{k} \quad 3.9$$

where:  $C_{1\varepsilon} = 1.42$ ,  $C_{2\varepsilon} = 1.68$ ,  $\mu_{eff}$  is the effective viscosity,  $a_k$  and  $a_\varepsilon$  are the inverse effective Prandtl numbers for  $k$  and  $\varepsilon$  respectively.

### 3.4 Numerical Simulation Procedure

The main steps during a numerical simulation consist of: pre-processing, solving and post-processing.

**Pre-processing** is to prepare the work for numerical calculations including: selection of the related physical phenomena that need to be numerically solved (i.e. wind-induced pressures on the building roof and parapet), setting up the geometry of the region of interest (i.e. computational domain), creating proper mesh generations for that domain (i.e. grid formation) and setting up the boundary conditions for the governing equations.

**Solving** contains the procedures to get the solution of the equations. Fluent provides two solvers: a segregated solver and a coupled solver. The current study uses the segregated solver, which is appropriate for incompressible flow. The Semi-Implicit Method for Pressure-Linked Equations (SIMPLE) scheme (Van Doormal and Raithby, 1984) is used for introducing pressure into the continuity equation. The numerical simulation of wind

flow conditions around a low rectangular building is carried out until the residues of all equations reach the round-off limit of machine accuracy. The residue is the difference between the results of two successive steps and the relative residue is defined as the ratio of the current residue to the residue after the first iteration. The relative residue is used as the convergence criterion and is set to  $10^{-6}$  for all simulations. The pressure and velocity distribution are obtained when the residues reach the convergence limit.

**Post-processing** implies retrieving graphical and numerical information about the variables from the solution. Wind-induced pressures on the building roof and parapet are expressed in the form of pressure coefficient ( $C_p$ ) as follows:

$$C_p = \frac{(p_{mean} - p_o)}{\frac{1}{2}\rho U_H^2} \quad 3.10$$

where  $p_o$  is the static pressure at free stream,  $\frac{1}{2}\rho U_H^2$  is the dynamic pressure in which  $U_H$  is the mean wind speed at roof height. Figure 3.1 presents a flow chart of the numerical solution method.

### 3.4.1 Computational domain

The wind flow is simulated in three dimensions over the building at 1/50 scale model. The dimensions of the building model are  $L \times B \times H = 0.08 \times 0.065 \times 0.06 \text{ m}^3$ . The building model with roof overhang was also tested. The computational domain was selected to be large enough compared with the building model, so the small building set in a large open field does not affect the mean wind flow conditions at the boundary of the domain. The length of upstream field is  $6H$ , where  $H$  is the building height. The

downstream field length must be long enough to ensure that the flow at the outlet boundary is not affected by the building;  $30H$  down-stream from the leeward face of the building model is selected. The upper boundary is about  $8H$  from roof surface and the domain width is extended about  $8H$  from each sideward face. The computational domain has dimensions  $2.24 \times 1 \times 0.5 \text{ m}^3$ . Figure 3.2 shows the details of computational domain and building configuration. The figure also shows the configurations of the building model with overhang

#### **3.4.2 Grid generation**

Some of previous numerical studies have attributed poor prediction of wind pressure of flat roofs because of coarse grid arrangement (Murakami, 1990). of a non-staggered grid system is easier than that of a staggered system; however the pressures near solid surfaces had to be obtained by extrapolation. Also, a non-staggered grid system is not recommended to predict the roof pressures of low-rise buildings (Selvam, 1992). The grid scheme used in the current computation is the rectangular staggered grid system, since this is considered as the most 'body-fitted' system for buildings of rectangular shapes. Grid arrangements are generated with dense grid lines near solid boundaries and relatively coarse grid lines far from solid boundaries. The flow properties significantly change near the windward corners of building roof, because of the high vorticity behind them. The distances between the first grid line to the roof surface and to the windward wall are very important parameters for the numerical evaluation of roof pressures, in order to achieve good prediction (Stathopoulos and Zhou, 1993). Very small distances

from the first grid line to the roof, upstream wall and parapet have been chosen (0.0007 m). For down stream and side walls of the building and the parapet 0.002 m is set, since surface pressures are not sensitive to the mesh at these locations the (Stathopoulos and Baskaran, 1990-b; Stathopoulos and Zhou, 1993). Figure 3.3 presents the current grid arrangement for the computational domain.

### 3.4.3 Boundary conditions

Adequate boundary conditions for turbulent flow should be applied in order to obtain good estimation of wind pressures on buildings. ‘*No-slip wall*’ boundary conditions are set for ground surface (i.e. bottom of the computational domain). The standard wall function approach (Launder and Spalding, 1974) with sand-grain-based roughness modification (Cebeci and Bradshaw, 1977) is used to model the near-wall region for bottom boundary. In Fluent 6.1 the equivalent sand-grain roughness height,  $k_s$ , can be obtained as follows (Blocken et al., 2007):

$$k_s = \frac{9.793z_0}{C_s} \quad 3.11$$

where  $z_0 = 0.0016$  m is the aerodynamic roughness length, obtained from wind tunnel data, and  $C_s$  is the roughness constant. Considering the default  $C_s = 0.5$ ,  $k_s$  should be 0.031 m. However, Fluent Inc. (2005) warns the users to obey the requirement  $z_p > k_s$ , where  $z_p$  is the distance from the bottom boundary to the center point of the wall adjacent cell. The value of  $z_p = 0.002$  m is selected since accurate solutions for near-ground flow can only be obtained with high grid resolution near the bottom of the domain. Therefore,  $k_s$  will be limited to 0.002 m at the bottom of the computational domain. In this case,  $C_s$

should be 7.83. However, Fluent Inc. (2005) recommends considering a value between 0.5 and 1.0 for  $C_s$ ; therefore the default  $C_s = 0.5$  is used. It should be noted that if the upstream length in the computational domain is about the same as that between the start of the turntable and the building model in the wind tunnel, which is the case of this study, then taking a lower  $C_s$  value, in comparison with that satisfying equation 3.11, is allowed. This can be related to the very low roughness of the turntable, where no roughness elements are present during the tests.

Note that, using incorrect roughness height can lead to stream-wise changes (horizontal inhomogeneity) in the vertical profiles of wind speed and turbulent parameters as the flow travels through the computational domain. Blocken et al. (2007) explain the inconsistency in the requirement for the Atmospheric Boundary Layer (ABL) flow simulation and provide different solutions such as using a small, as possible, upstream distance (which is limited to 0.36 m in this study).

The value of  $z_p$  can be obtained from the following equation:

$$Z^+ = \frac{u^* z_p}{\nu} \tag{3.12}$$

where:  $Z^+$  is normalized wall distance,  $u^*$  is friction velocity,  $\nu$  is the kinematic viscosity ( $\nu = \mu/\rho$ ) and  $p$  is the center point of the wall-adjacent cell. The logarithmic law for mean velocity is known to be valid for  $30 < Z^+ < 60$ . In Fluent, the log law is employed when  $Z^+ > 11.225$ . When the mesh is such that  $Z^+ < 11.225$  at the wall adjacent cells, Fluent applies the laminar stress-strain relationship. The velocity profile of the turbulent flow in the recirculation region behind a backward facing step was measured by Adams

and Johnston (1998). Zhou (1995) compared the velocity profile measured by Adams with the log-law velocity profile and found that the measured velocity distribution deviates significantly from the logarithmic part of the wall function when:  $Z^+ > 7$ .

The inlet profiles of mean velocity ( $U$ ) and turbulence parameters ( $k$  and  $\varepsilon$ ) were interpreted in Fluent as User Defined Functions (UDF) and the wind tunnel measured data was used. The ‘*Inlet-velocity*’ boundary condition was taken at the inlet of the computational domain. The mean wind speed profile was modeled by the power law with exponent  $\alpha = 0.29$  and maximum  $U_g = 12$  m/s at gradient height  $z_g = 0.6$  m; turbulence quantities are given by Richards and Hoxey (1993) as follows:

$$\frac{\bar{U}}{U_g} = \left( \frac{z}{z_g} \right)^\alpha \quad 3.13$$

$$k = \frac{u^{*2}}{\sqrt{C_\mu}} \quad 3.14$$

$$\varepsilon = \frac{u^{*3}}{\kappa z} \quad 3.15$$

where  $u^*$  is the friction velocity (0.56 m/s) for an aerodynamic roughness length  $z_0 = 0.0016$  m,  $\kappa$  is von Karman constant (0.42). ‘*No-slip wall*’ boundary conditions are assumed for building and parapet surfaces with  $C_s = 0.5$  and  $k_s = 0$ . ‘*Symmetry*’ boundary conditions (i.e. with zero shear slip) are applied to the sides of the computational domain; while ‘*outflow*’ boundary condition, assumes no stream-wise gradients at this location, is set to the outlet of the computational domain. To avoid additional stream-wise gradients, at the top of the domain, the values of the mean velocity and turbulent parameters are

fixed by using the inlet profiles values at this height. These values are:  $U = 7.95$  m/s,  $k = 1.044$  m<sup>2</sup>/s<sup>2</sup> and  $\varepsilon = 0.104$  m<sup>2</sup>/s<sup>3</sup> (Blocken et al. 2007).

A 3-D simulation is made in an empty domain, with grid distribution similar to the domain with the building model, to evaluate the extent of stream-wise changes. Comparisons between the inlet ( $x = 0$ ) and incident (building position,  $x = 0.36$ ) profiles of mean velocity and turbulent quantities is presented in Figure 3.4. The first 0.2 m from ground surface is considered. Figure 3-c shows the vertical profile of  $k$  obtained from the wind tunnel testing. The numerical profile agrees with the experimental one. In general, minor differences occurring between the two positions for all parameters; which means that the stream-wise changes are successfully limited.

### **3.5 Sensitivity Study of the Numerical Solution**

Any numerical solution is considered to be converged when the difference between the final solution and the successive approximation tends to approach zero as the number of iterations increased. Sensitivity is defined from the behavior of the system output for variations in the system input. Sensitivity is one of the factors that characterize the performance of the iterative procedure for a steady-state condition. This issue is studied by considering two main factors: extent of computational domain and utilizing different number of nodes. Figure 3.5 shows the computational domain cluster for the considered study in plan ( $x$ - $y$ ) and sectional ( $x$ - $z$ ) views. An Upstream Distance ( $USD$ ) from the windward wall and a Downstream Distance ( $DSD$ ) from the leeward wall define the

boundaries of the computational domain along  $x$ -direction. Distances  $DS$  and  $DT$  are used for  $y$ - and  $z$ -directions respectively. Four domain sets are considered in the present analysis. The extent of the computational domain along  $x$ -,  $y$ - and  $z$ -direction has been chosen based on the study of Paterson, 1986, and Murakami and Mochida, 1988. Table 3.1 lists the specifications of all domain sets. Note that, in this analysis the total number of nodes (195,000) is kept constant. Considering D1 as the base, the effects on computed results by increasing or decreasing the domain size are analyzed.

The induced pressure values are evaluated for the variation in the domain distance as shown in Figure 3.6. The induced suction along the center line of the roof are presented. Increasing the size of the domain by keeping the number of grid points constant, increases the grid spacing. When comparing the observations of the figure including the experimental results, D1 domain specifications appears as a good choice. This domain was used in the present simulation. The analysis shows that an increase in the size of the domain without increasing the number of nodes may reduce the accuracy of the computed results.

**Table 3.1: Specification of computational domain sets used in the current analysis**

<b>SET</b>	<b>x-direction</b>		<b>y-direction</b>	<b>z-direction</b>
	<b>USD</b>	<b>DSD</b>	<b>DS</b>	<b>DT</b>
<b>D1</b>	<b>6H</b>	<b>30H</b>	<b>8H</b>	<b>8H</b>
D2	13H	26H	10H	8H
D3	17H	34H	13H	12H

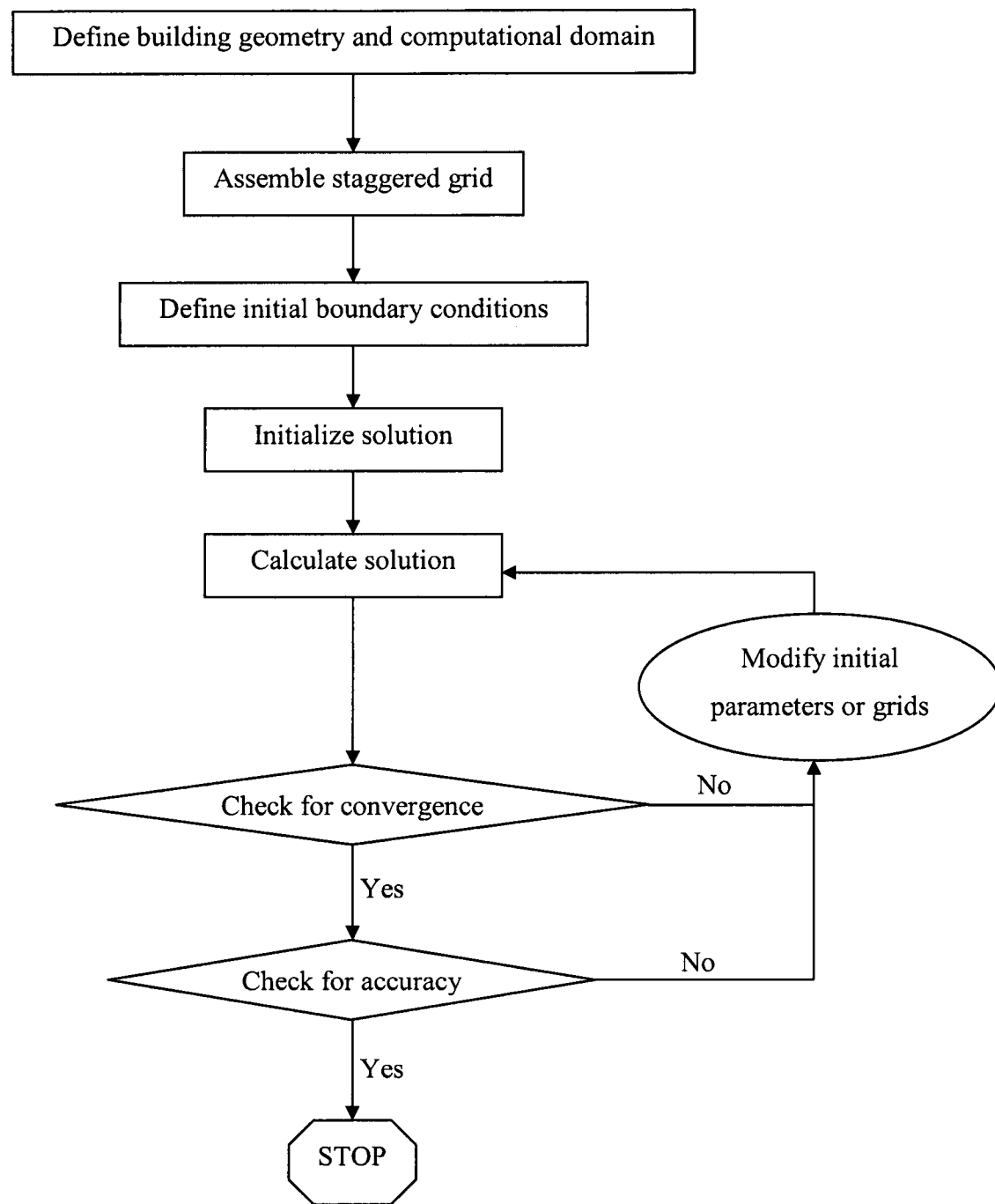


**Figure 3.1: Flow chart of numerical computation method**

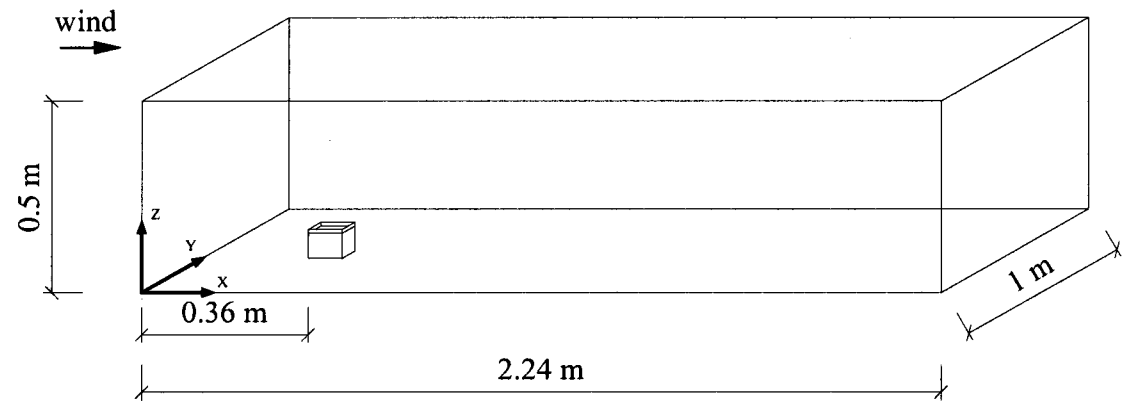
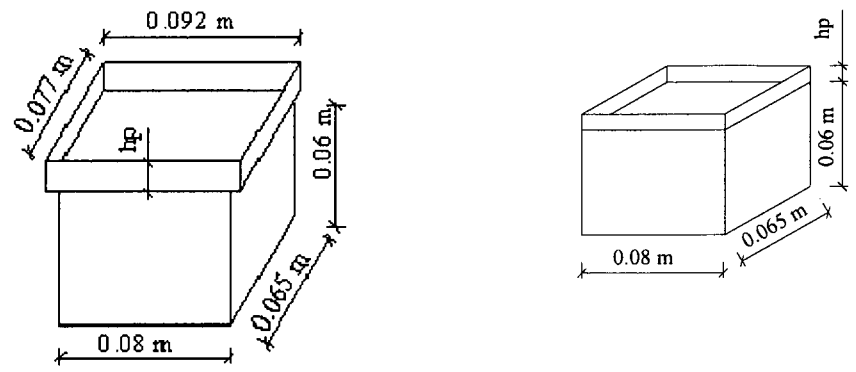


**Figure 3.2: Building configurations and computational domain (not to scale)**

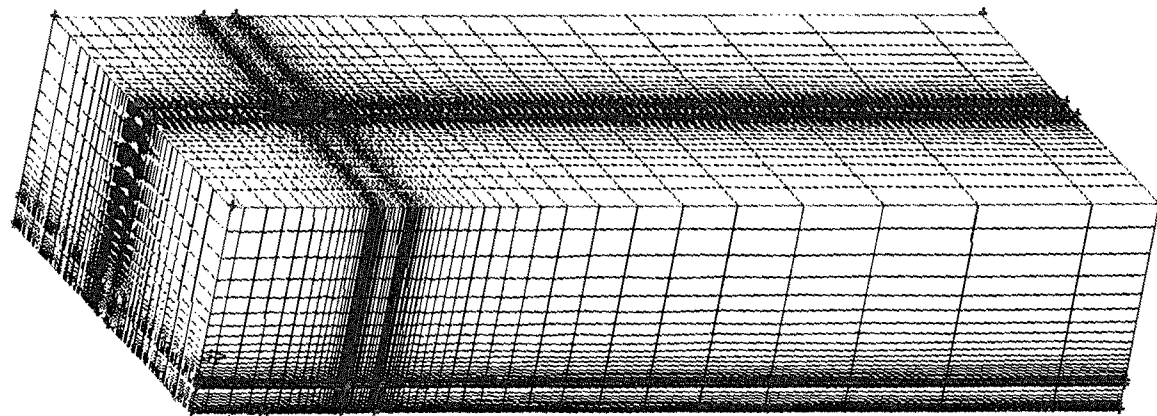
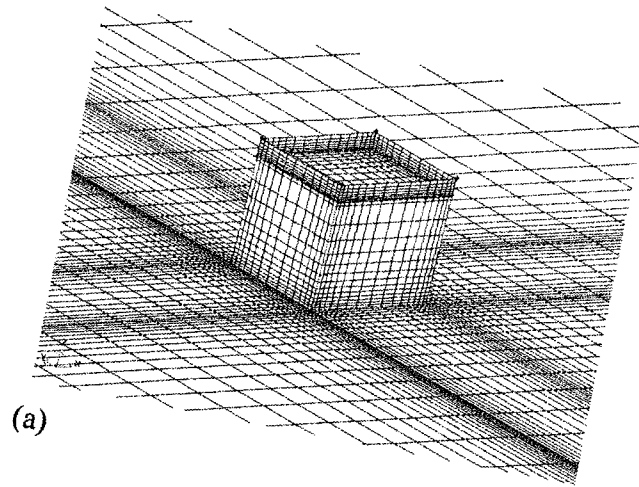
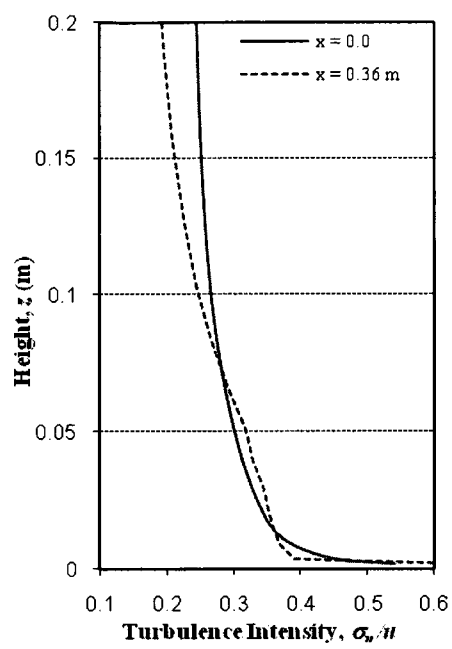
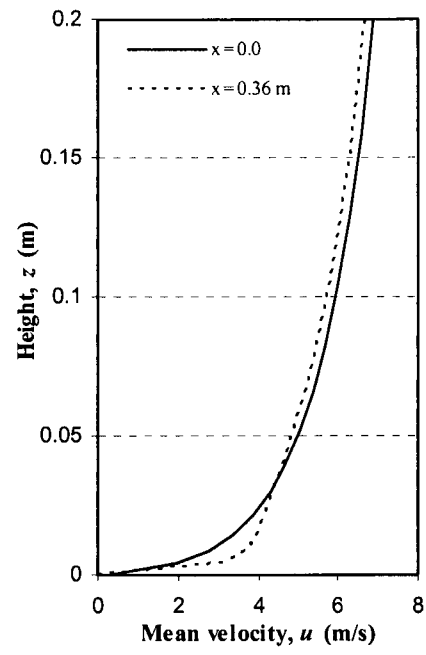


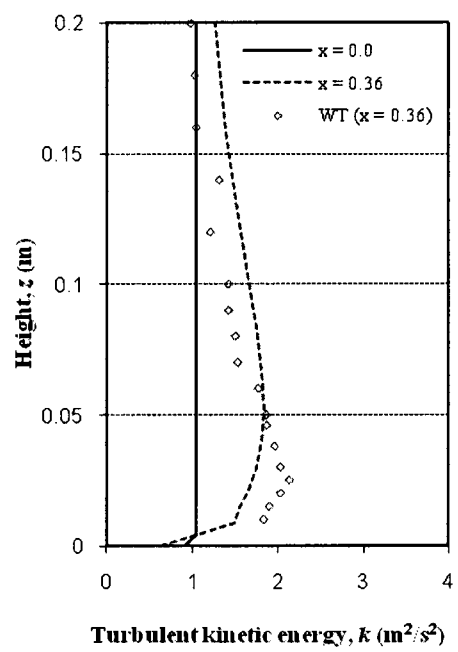
**Figure 3.3: Grid arrangement in the computational domain: (a) near the building model and (b) for the whole domain.**



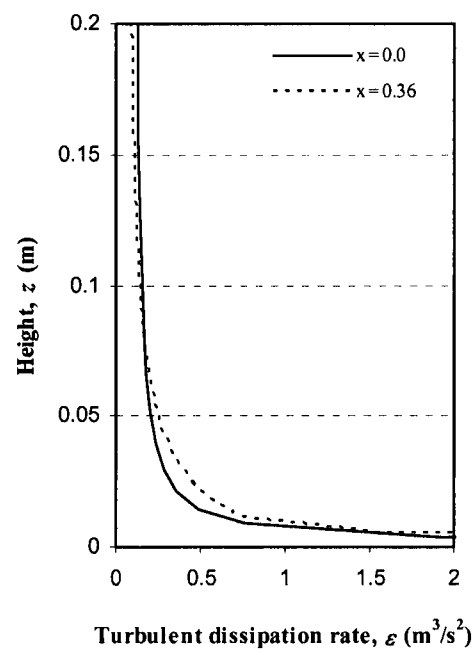
(a)



(b)



(c)



(d)

**Figure 3.4: Inlet and incident vertical profiles of (a) Turbulence intensity, (b) Mean velocity, (c) Turbulent kinetic energy, (d) Turbulent dissipation rate**

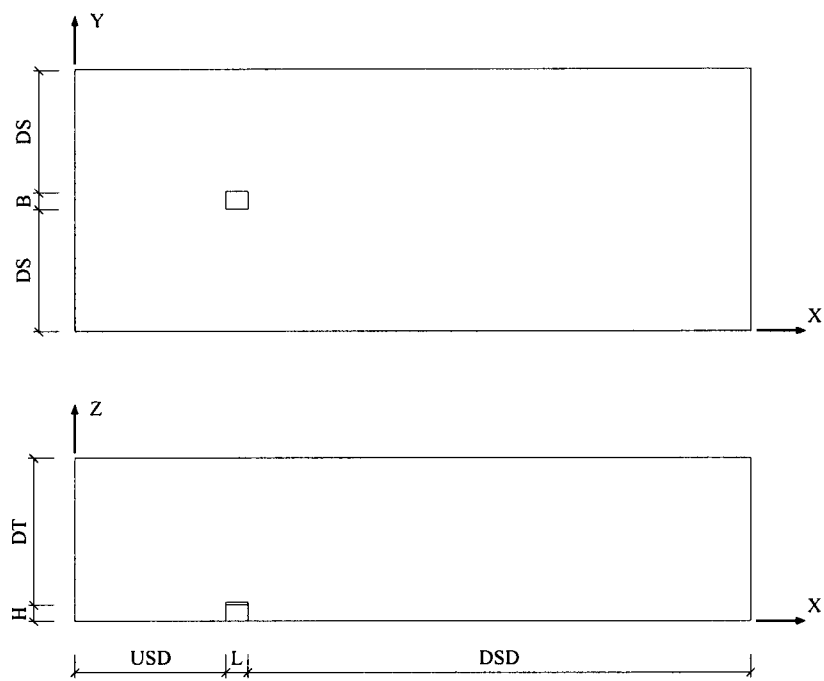


**Figure 3.5: Computational domain used in sensitivity analysis**

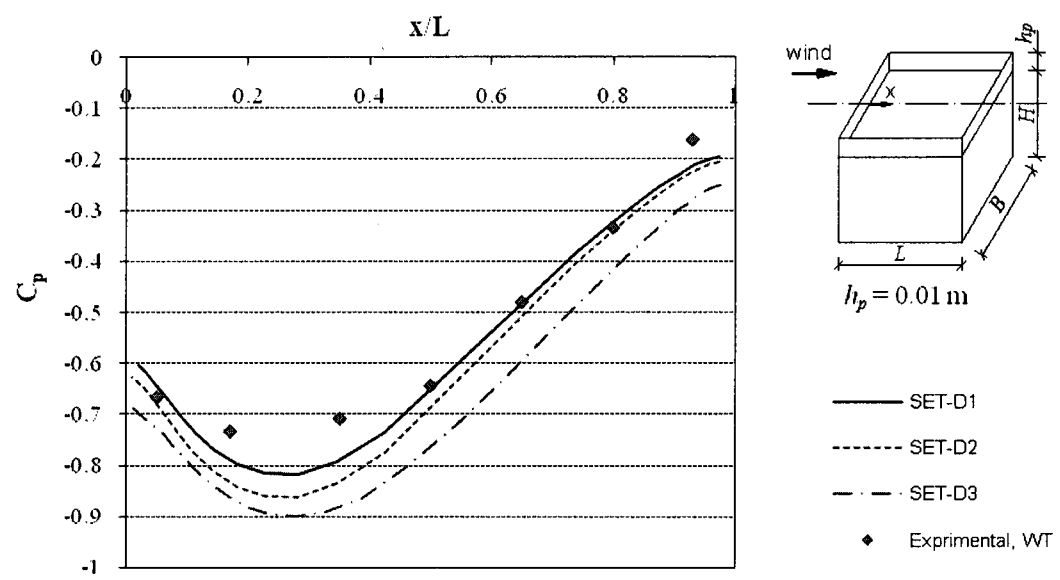


**Figure 3.6: Experimental and computational pressure coefficients with different computational domains**

## *Chapter Four*

### **EXPERIMENTAL WORK**

This chapter presents the details of the full-scale experimental building and field measurements. In addition, a complete wind tunnel simulation of wind flow over a model of that building is presented

#### **4.1 Full-Scale Testing**

Full-scale testing has been completed to examine surface parapet pressures. The test site should be subjected to adequately strong winds for most part of the year to facilitate having maximum number of observations and good response of the instruments. The city of Montreal experiences strong winds in the winter season. However, because of severe winter conditions, it is difficult to carry out field experiments between December and April. The measurements of this work had been carried out between May and November of three consecutive years.

##### **4.1.1 Experimental building**

The ideal type of terrain for testing low-rise buildings is the open country i.e. with no tall trees, buildings and other obstructions in the surrounding area. A small low-rise building

with a perimeter parapet was used to measure wind-induced pressures on parapet surfaces. The building is located at the corner of the soccer field of the Loyola Campus (about 8 km west from downtown Montreal) of Concordia University and housed the instruments required for the experimentation. The exposure of the test site can be classified into two categories, open country and suburban, depending on the wind direction. Two sides of the building are exposed to a suburban type of terrain, with small buildings and high trees, for winds from North-East and South-East. The other two sides are exposed to open country type of terrain for winds from North-West and South-West. The basic direction for the strongest winds in the Montreal area is South-West, thus the basic exposure of the experimental building is considered as open country terrain.

Figure 4.1 shows the upstream of the building, facing South-West. The building is a made of brick and is 3.10 m high, 4.00 m long and 3.25 m wide. The roof is larger than the base, 4.45 m long and 3.70 m wide (Figure 4.2). More details about this experimental station can be found in Stathopoulos et al. (1999). A perimeter parapet with a height of 0.5 m is attached to the roof. The parapet is made out of wood, 11 mm (7/16") aspenite board, separated by a 13 mm stud. The parapet section is 0.16 m thick and is fixed to the roof by plate connection fastened with screws to hold them together. The interior, exterior and top parapet surfaces are drilled for tapping. Each pressure tap had 3.2 mm inside diameter and is connected by a steel pipe to a plastic tube. Figure 4.3 shows the locations of all tapping and the definition of wind angles. The subscripts  $e$ ,  $i$  and  $t$  refer to the exterior, interior and top surface tapping respectively, while the subscript  $r$  refers to the roof tapping.

#### 4.1.2 Measurement of wind speed and direction

For measuring wind speed, a three-cup anemometer, from Teledyne Geotech, is used. This anemometer provides an output voltage proportional to wind velocity. A wind vane is attached to the same tower with the anemometer to indicate the azimuth of the incident winds (See Figure 4.2). In the current study, the acquisition of accurate records of wind speed and direction is very important. The anemometer has to be placed in a spot near the location of measurement that is not affected by the wind flow around the building. Therefore, it is mounted on a metal tower on the top of the building. According to the ASHRAE (1999) recommendations the anemometer should be placed at a height of  $1.5R$  above the building, in which  $R$  is scaling length and is calculated as follows:

$$R = B_S^{0.67} B_L^{0.33} \quad 4.1$$

where:  $B_S$  = smaller of  $H$  and  $B$ ,  $B_L$  = larger of  $H$  and  $B$ . At this height the building does not influence the flow (Figure 4.4). Considering  $B_S = 3.6$  m ( $H + hp$ ) and  $B_L = 4.5$  then,  $1.5R = 5.8$  m and the minimum height for placing the three cups is equal to 9.4 m from the ground surface. The height of the tower is 6.7 m and the height of the anemometer from the base of the building is about 10 m. The output of the anemometer is given in volts and is directly proportional to the wind speed. The anemometer was calibrated in the Boundary Layer Wind Tunnel (BLWT) of Concordia University. Calibration details are presented at Appendix A. Wind vane is attached on the same tower with the anemometer for the purpose of azimuth measurements for the incident winds. The wind speed and direction are indicated on a compact box. For calibration purposes, the wind vane is pointed to a particular direction, e.g. north, and the output in volts is measured.

The present calibration was checked repeatedly at regular intervals during the experimentation, to confirm its steadiness.

#### **4.1.3 Upstream wind flow parameters**

According to the NBCC (2005), the exposure of the test site can be classified as category C (open country terrain). The standard recommends roughness length  $z_o = 0.02$  m and power law exponent  $\alpha = 0.16$  for such terrain. Other standards recommended even higher values; for example, ESDU (1983) considers  $z_o = 0.03$  m for open country terrain. Although, field observations of the complete mean wind profile were not available, the upwind flow parameters could be estimated based on the recorded turbulence intensity in the site. The current field observations showed that the average turbulence intensity at the anemometer height was 22 %, during the entire period of test records. Consequently, the average turbulence intensity at the roof height was 28 % and the average roughness length was 0.11 m. These values were estimated according to the charts provided by Tieleman, 2003, who proposed a method derived from basic flow relations to estimate the upwind roughness parameters. Considering  $\alpha = 0.16$ , the velocity at the roof height was found about 17 % lower than that measured at the anemometer height. Another commonly used measure of the variability of the wind is the *gust factor*,  $G_u$ , which had an average value of 1.64 during the measurement period. A complete description for calculating the wind flow parameters is presented in Appendix A.

As already mentioned, due to severe winter conditions in Montreal area, all field measurements were carried out during the summer and fall seasons, when the strongest winds blow from West and South-West. Therefore, limited data were recorded for wind azimuth  $90^\circ - 180^\circ$ . The randomness of the natural wind leads to a significant variability in wind direction, thus higher variation of wind direction occurs on the site comparing with the wind tunnel conditions. The US Nuclear Regulatory Commission (USNRC) recommended '*the standard deviation of the wind direction*' ( $\sigma_\theta$ ) method to simply classify the atmospheric stability (Mohan and Siddiqui, 1998). Stability is an expression applied qualitatively to the property of the atmosphere, which governs the acceleration of the vertical motion of air (Snaebjornsson, 2002). Table 4.1 presents the classification of atmospheric stability as used by Sedefian and Bennet (1980). In the present study, data was only considered when  $\sigma_\theta < 7.5^\circ$ , which classified the atmosphere as '*moderately stable*' (Group E). In order to obtain reliable response of the instruments, data was collected at windy days and was only considered when the wind velocity is higher than 5.6 m/s (20 km/hr) at the anemometer height. Table 4.2 summarizes the field testing parameters of upstream wind flow during the entire period of the experimentation.

#### **4.1.4 Reference static pressure**

In full-scale testing special consideration is required to obtain adequate reference pressure. Atmospheric static pressure is used as reference pressure, as it provides the most useful data for experiments on building aerodynamics (Levitan, 1993). Placement of the static pressure point is critical; it should be placed at a sufficient distance away

from the building so that it is not affected by the static pressure field of the building. The reference pressure has to be steady in order to obtain reliable field pressure data (Levitan and Mehta, 1992). At the initial stages of measurements, the reference pressure was measured at various locations around the building to ensure stability and negligible effects on the measured pressures. Reference pressure was measured at the ground level at a distance of 22 m west from the test building. The pressure at this location was transmitted to the test building using PVC flexible tube of 4 mm inner and 11.2 mm outer diameter. A common way of checking the reference pressure fluctuations is to connect the reference pressure to both ends of a transducer and measure the difference to ensure that reference pressure value is not fluctuating.

#### **4.1.5 Pressure measurements**

Pressures were measured with 10 differential pressure transducers, 160 PC,1 psi (6895 Pa) range, manufactured by Micro-Switch (a Honeywell Division) operated from a single positive supply voltage ranging from 6 to 12 volts DC. The instruments were calibrated, periodically, in the wind tunnel. For collecting mean wind pressures, the transducers were connected to pressure tapping with 4.5 m long PVC flexible. All tubes were collected in a 0.1 m diameter hole through the building roof and thus, the tubes were easily connected to the transducers. For measuring instantaneous peak pressures, four transducers were mounted inside the parapet section next to the tap being monitored, and could easily be moved from one tap to another (see Figure 4.3). Each tapping point was connected to a transducer by a 0.15 m long PVC flexible tube with 3.2 mm internal

diameter. The length and diameter of the tubes control the frequency response of the pressure system (Holmes, 1984). The tube diameter should not be less than 3 mm to avoid condensation problems (Levitan, 1993). The length of the tube should be as short as possible to maximize the frequency resolution of the system (Gumley, 1983). Therefore, 0.15 m was decided to be a reasonable compromise between placing the pressure taps on all parapet surfaces, while obtaining satisfactory frequency resolution. In this case, only one side (side *B*) of the perimeter parapet was examined, due to technical restrictions. When no measurements are taken, all pressure taps have been sealed to avoid concentration of moisture inside the tubes. Using a compressor, air was blown inside each tube before starting measurements to ensure that all tubes are completely dry. A Hydra Data Logger unit (Model 2635-A) from Fluke and Philips was used for data acquisition during the experimentation. The instrument is a 21-channel data acquisition unit with maximum sampling rate of 1 Hz. Data is subsequently transferred to a portable PC unit. Two channels are connected to the anemometer and the vane for collecting wind speed and direction through a data acquisition unit. The other channels are connected to the pressure transducers for collecting pressure difference records. Although it is recognized that the sampling frequency of 1 Hz may be on the low side, this was the only instrumentation available at the time of field measurements.

Wind-induced pressure acting on the building surfaces is a function of wind speed and direction, air density ( $\rho$ ), barometric pressure, building geometry and surrounding terrain. While wind speed and air density can vary significantly between experiments, it is not possible to compare wind-induced pressure directly from one experiment to another.

Therefore, a dimensionless form of pressure measurement, pressure coefficient (Simiu and Scanlan, 1986) is commonly used:

$$C_p = \frac{P - P_o}{\frac{1}{2} \rho U^2} \quad 4.2$$

The denominator in this equation is equal to the mean dynamic pressure. In the current study pressure coefficients were referenced to the mean dynamic pressure at the building height (roof level).

#### 4.1.6 Verification of the collected data

The first step in full-scale experimental analysis is verification of the collected data. The wind speed and direction, measured by the anemometer, had been compared to the data provided by the Meteorological Service of Canada (MSC), which is available on the web at [www.ec.gc.ca](http://www.ec.gc.ca). The wind parameters are observed at Trudeau Airport (10 m above the ground) where the exposure is considered as flat open terrain. Figure 4.5 shows a sample of the data collected in two different days in order to check the correctness of readings for both exposures considered. The difference in wind speed could be attributed to the difference of geographical features for each site. Power law is used for converting the data obtained from MSC to match the results measured at the experimental site (Loyola) in terms of height and roughness:

$$\frac{U_{z_1}}{U_{z_2}} = \left( \frac{z_1}{z_{G_1}} \right)^{\alpha_1} \left( \frac{z_{G_2}}{z_2} \right)^{\alpha_2} \quad 4.3$$

where:  $U_Z$  is the velocity measured at a height  $Z$ ,  $Z_G$  is the gradient height and  $\alpha$  is power law exponent. Note that, the subscript 1 refers at data of Dorval location, while the subscript 2 refers at current data of Loyola site.

Verification of the field measurements required a visual inspection of time history plots. Checks are performed to ensure that the time series data have been recorded properly. For each record time history plot is carefully examined to see if there are any immediate problems. The time histories are also compared for similar wind speeds and directions to see if the observations are consistent. Figure 4.6 shows the wind speed and wind direction for a 10-minute sampling period, while Figure 4.7 shows the time history for the exterior and interior surface parapet pressure at a corner tap (*BI*) for the same record. Visual inspections of wind stationary were also completed for all records.

## **4.2 Wind Tunnel Modeling**

The experimental building has been modeled to be tested in the BLWT of Concordia University. The wind tunnel has a 12.2 m long working section 1.8 m wide with variable height (1.6 m high at the measurements location). All information about the design and fabrication of this wind tunnel is given by Stathopoulos (1984). The boundary layer develops naturally over a rough floor with the assistance of some passive devices. Roughness blocks with different heights and arrangements were used. This implies that different wind tunnel floor roughness develop conditions representative of different terrain exposures. The heights and arrangements of these blocks were adjusted to create

simulated wind velocity and turbulence profiles comparable with those of the ESDU standards. The inlet screen (Figure 4.8-a) was installed behind 6 horizontal rods (metal pipes) of different diameters and a mounted board with boxes was placed next to the inlet screen, which produced the inlet setting. Figure 4.8-b shows an inside view of the wind tunnel with the current roughness configuration.

#### **4.2.1 Modeling the experimental building**

The modeling in wind tunnel is extremely complex particularly when dealing with small structural elements, such as parapets. The accuracy of the results and the capability of comparison with full-scale data depend mainly on the correctness of the modeling of building geometry and the simulation of the atmospheric boundary layer characteristics. Extensive measurements were carried out by Stathopoulos, 1984, to evaluate the simulation characteristics of the BLWT of Concordia University including velocity profile, intensity, scale and spectrum of the longitudinal turbulence component. The study indicated that a 1:400 geometric scale is most appropriate. However, the experimental building is a small low-rise building; its eave height is 3.1 m, which would be modeled to 8 mm in 1:400 length scale. This small model is not of sufficient size to develop parapet details to study the aerodynamic forces. Moreover, it is too small to allow adequate level of small-scale turbulence in the incident flow at roof level and leads to relatively low Reynolds number (Tieleman, 2003).

To overcome the problems of modeling small details, a geometric model scale of 1:50 is utilized in the present study. The choice of modeling scale was based on the importance of correctly modeling the turbulence intensity at the roof height, which was indeed similar with that measured in the field. The model is made out of plexi-glass with two sets of perimeter parapets: 0.01 m and 0.02 m, of an equivalent full-scale height of 0.5 m and 1 m respectively, attached to the roof (see Figure 4.9). Pressure taps were drilled on the exterior and the interior as well as the top surface of the parapet. The parapet thickness is 3 mm and the tapping has an inside diameter of 1mm. Figure 4.10 illustrates the pressure tapping layout of the model. The definition of wind approach angle is also shown in the figure. The number of pressure taps located on the parapet itself varied with parapet height. A total of 48 taps were located on the 0.5 m parapet and 96 taps on the 1 m parapet. In addition, 42 pressure taps were placed on the roof surface.

#### **4.2.2 Boundary layer simulation**

In order to correctly model the wind flow, both velocity and turbulence characteristics of the natural wind should be accurately simulated in the wind tunnel. Wang et al, 1996, suggested that correct modeling of roughness length leads to correct pressure coefficients even with a mismatch of the scale ratio. However, the wind engineering vision now moves toward considering correct simulation of the turbulence characteristics in testing low-rise buildings with larger length scale, while the mean flow profile parameters may not require exact simulation (Tieleman, 1998). Increasing the upstream ground roughness acts to retard the wind flow close to the ground and hence reduces mean wind

speed at the roof level. On the other hand, higher turbulence will be obtained. In this case, it will be possible to examine larger building models. However, this is restricted by the wind tunnel blockage, which should be less than 5% (Laneville, 1990). In order to examine low-rise buildings with larger length scale, researchers in the Boundary Layer Wind Tunnel II of the UWO used additional turbulence generating devices, including spires and a tall barrier, which were added across the wind tunnel at the entrance (Ho et al., 2005 and St. Pierre et al., 2005). These devices were used to create turbulence characteristics consistent with larger length scales, 1:100 and 1:50.

Following the same concept, the current study applies a different approach to attain correct matching of the turbulence characteristics as well as roughness length with those in the field. In this case a length scale of 1/50 was used and the wind tunnel blockage was 0.2%. To achieve higher turbulence intensity at roof height, which is the most important to be matched since the pressure coefficients are normalized by this height (Ho, 1992); turbulent shear flows are generated over different upstream roughness configurations. For each arrangement, turbulence intensity and mean velocity profiles are obtained. Essentially, the required roughness blocks are higher than in full-scale, but they are placed 1.2 m upstream of the center of the turntable where the model is located see Figure 4.8-b). Table 4.3 shows the experimental parameters measured in the wind tunnel using different arrangements of the upstream roughness elements. By comparing each parameter with the corresponding full-scale value, it was found that Terrain-4 is the most appropriate. Note that, the selected simulated exposure shows reasonable match of

Jensen number ( $J_e = H / z_o$ ), which is one of the important dimensionless parameters in similarity requirements.

Figure 4.11-a depicts the turbulence intensity profile for the simulated exposure compared with the ESDU (1983) profile, which is described in Appendix B. The turbulence intensity measured at the test site is also shown at the anemometer and the roof heights. Clearly, the measured profile agrees with the ESDU profile below 5 m height, while a clear difference occurs above this height. Since the main goal of the current wind tunnel simulation is to match the turbulence intensity at the roof height, this discrepancy may be acceptable. The full-scale turbulence values agree well with ESDU profile at both roof and anemometer heights, considering their variability resulting from natural wind. Mean wind velocity profiles are shown in Figure 4.11-b, where the velocity was normalized by the reference velocity at the wind tunnel (12 m/s). The wind tunnel profile agrees well with that of ESDU. By fitting power law profile, an exponent  $\alpha = 0.29$  was found. The vertical profiles of mean wind speed and turbulence intensity for all other tested exposures are presented in Appendix A.

Spectral density function has been determined at roof height using the velocity time histories (Figure 4.11-c). The spectra are normalized by the square of velocity fluctuation at roof height and the frequency is normalized by the mean velocity at roof height. By fitting the Von Karman equation (Simiu and Scanlan, 1996) to the spectra, it was found that the length scale of turbulence,  $L_x = 0.22$  m at the roof height and 0.28 m at 10 m level (see Appendix A for more details).

Wind tunnel measurements are made at a gradient speed of 12 m/s. The velocity profile is recorded at the centre of the turntable without the model in place. A general-purpose program was developed (Wang, 2005) in a host PC computer that controlled the scan frequency and duration of a hot-wire device via a multiplexer. This program reported statistics data on-line and recorded data for off-line process. The scan frequency is set at 1000 Hz and the scan duration is set routinely at 32,768 seconds. The hot-wire probe is attached to a traversing gear system, which could be moved up and down mechanically. At each measurement height, the mean and standard deviation of the tunnel speed is recorded, providing the mean velocity and turbulence intensity profiles. Roughness length,  $z_o = 0.08$  m, was obtained by fitting the logarithmic law. Velocity time histories were recorded for roof height ( $z = 0.062$  m) and for 10 m elevation in full-scale or anemometer height ( $z = 0.2$  m).

#### 4.2.3 Wind-induced pressure

The accuracy of the measured pressures depends on the achieved dynamic similarity. Correct dynamic similarity requires matching of the Reynolds number in full-scale and wind tunnel. However, this is not possible in conventional wind tunnels. The Reynolds number is defined as:

$$R_e = \frac{UD}{\nu} \quad 4.4$$

where  $U$  is the oncoming velocity,  $D$  is the characteristic length and  $\nu$  is the kinematic viscosity of the air. A previously held view considered that bluff-body aerodynamics is Reynolds number insensitive for sharp edge elements (Simiu and Scanlan, 1996), where

points of flow separation are more or less fixed. However, recent investigations demonstrate that relaxing the Reynolds number in wind engineering might cause minor systematic errors (Larose and D'Auteuil, 2006). The Reynolds number for the current full-scale building is  $2.2 \times 10^6$  and for the wind tunnel model is  $5 \times 10^4$  with a length scale of 1/50 and  $6.2 \times 10^3$  with a length scale of 1/400, where  $D$  is the building length and  $U$  is the mean hourly wind speed at 10 m height. It can be noted that using larger model act to minimize the difference in Reynolds number between full and model scale.

#### **4.2.3.1 Pressure measurements**

Pressure fluctuations were measured with a Scanivalve's Digital Service Module (DSM-3000 system) that was connected to two Zero-Calibrate-Operate (ZOC-33) pressure transducers, each of which was factory-designed to scan 64 pressure taps simultaneously. The DSM system was controlled by a host computer. The installation and operation of this measuring system, as well as the calculations of scanning time and frequency, are presented in Appendix A. To correspond to acceptable wind tunnel testing practices on the bases of the assumed time scale, the scanning frequency is 250 Hz and the scanning duration is 24 sec (details are presented in Appendix A). The scanning frequency in the wind tunnel is higher than the corresponding full-scale frequency. Therefore, an attempt was made to compare the measured peak pressures with those obtained using 50 Hz scanning frequency. The comparison reveals an average difference not more than 10% for all cases.

Tubing system of 645.4 mm length leads from the surface tap to the scanivalve. This system consists of 10 mm length steel tube of 0.8 mm internal diameter, drilled into the model; connected to 365 mm long and 1.6 mm internal diameter flexible PVC tube; leads to 25.4 mm long steel restrictor, of 0.16 mm internal diameter to keep the frequency response flat; leads to 245 mm long tube connected to the scanivalve. The resulting system responds to pressure fluctuations on the model up to about 100 Hz with negligible attenuation or distortion (Stathopoulos and Saathoff, 1992).

Pressure time histories were recorded simultaneously at all tap locations and statistics pressure coefficients (maximum, minimum, mean and rms) were determined. Pressure coefficients ( $C_p$ ) were referenced to the mean dynamic pressure ( $1/2\rho U^2$ ) at the building height. Measurements were repeated for 13 wind angles, ranging from  $0^\circ$  to  $180^\circ$ . Therefore, due to building symmetry, a complete data set was obtained.

#### **4.2.3.2 Extreme value analysis**

The peak point pressure and area-averaged load coefficients presented in this study are not the absolute worst coefficients recorded within the sample time. Extreme values of time series data are significant for selection of the pressure peaks. As an application of the Gumbel distribution (Gumbel, 1958), extreme value 'Type I' is used for peak selection (also applied by Suresh Kumar, 1998; Holmes and Moriarty, 1999). In this case, the total time history of 6000 data-point is broken down into ten segments each of 600 data-point then ten segmental peaks are selected and fitted by Gumbel Plot (see

Appendix A for more details) with a cumulative probability of 0.975 (Uematsu and Isyumov 1998). The resulting mode ( $m$ ) and dispersion ( $s$ ) are used to determine the expected peak value for each pressure coefficient. Such peaks are believed to be more statistically stable quantities in comparison to the absolute worst recorded peaks. A sample for one case of Tap  $BI_e$  and for wind direction  $\theta = 0^\circ$  is presented in Figure 4.12 showing the time history for the first segment, i.e. 600 data-point, (Figure 4.12-a) and the Gumbel plot for this segment (Figure 4.12-b).

**Table 4.1: Stability classification (Sedefian and Bennet, 1980)**

<b>Stability classes</b>	<b>Group</b>	<b><math>\sigma_\theta</math> (°)</b>
Highly unstable or convective	A	$22.5 < \sigma_\theta$
Moderately unstable	B	$17.5 < \sigma_\theta < 22.5$
Slightly unstable	C	$12.5 < \sigma_\theta < 17.5$
Neutral	D	$7.5 < \sigma_\theta < 12.5$
<b>Moderately stable</b>	<b>E</b>	<b><math>3.75 &lt; \sigma_\theta &lt; 7.5</math></b>
Extremely stable	F	$2.0 < \sigma_\theta < 3.75$
Low wind night time stable	G	$\sigma_\theta < 2.0$

**Table 4.2: Full-scale testing parameters**

<b>Parameters</b>	<b>Data range (average)</b>
Upstream exposure (NBCC, 2005)	C, open country
Eave height, $H$ (m)	3.1
Parapet height, $h_p$ (m)	0.5
Anemometer height, $z_a$ (m)	10
Roof dimensions, $L \times B$ (m)	4.45 x 3.7
Power exponent parameter, $\alpha$	0.16
Roughness length, $z_o$ (m)	0.035 – 0.21 (0.11)
Mean wind velocity at $z_a$ , $U_a$ (m/s)	5.6 – 11.4 (9.5)
Mean wind velocity at $H$ , $U_{roof}$ (m/s)	4.6 – 9.5 (8.1)
Turbulence intensity at $z_a$ , $I_a$ (%)	18 – 29 (22)
Turbulence intensity at $H$ , $I_{roof}$ (%)	23 – 36 (28)
Length scale of turbulence at $z_a$ , $L_{x,a}$ (m)	36 – 83 (72)
Gust factor, $G_u$	1.55 – 1.95 (1.64)
Mean wind direction, $\theta$ (°)	5 – 177
Standard deviation of wind direction, $\sigma_\theta$ (°)	3.6 – 7.5 (6.3)

**Table 4.3: Wind tunnel modeling parameters for different simulated exposures**

Parameter	Full-scale	Simulated wind tunnel exposures <sup>m</sup> (scale 1:50)				
		Terrain-1	Terrain-2	Terrain-3	Terrain-4	Terrain-5
$\alpha$	0.16 <sup>e</sup>	0.15	0.24	0.28	<b>0.29</b>	0.34
$z_a$ (m)	10	0.2	0.2	0.2	<b>0.2</b>	0.2
$z_o$ (m)	0.035 – 0.21 <sup>e</sup>	0.005 <sup>f</sup>	0.04 <sup>f</sup>	0.07 <sup>f</sup>	<b>0.08<sup>f</sup></b>	1.05 <sup>f</sup>
$u^*$ (m/s)		0.50	0.63	0.7	<b>0.73</b>	0.8
$H / z_o$	14.76 – 88.5 <sup>e</sup>	620	77	44	<b>39</b>	3
$U_a$ (m/s)	5.6 – 11.4 <sup>m</sup>	11	10.6	10.4	<b>10.2</b>	10
$U_{roof}$ (m/s)	4.6 – 9.5 <sup>e</sup>	9	7	6.7	<b>6.3</b>	6.1
$I_a$ (%)	18 – 29 <sup>e</sup>	10	12	15	<b>19</b>	20
$I_{roof}$ (%)	23 – 36 <sup>e</sup>	14	28	25	<b>28</b>	30
$L_{x, a}$ (m)	36 – 83 <sup>e</sup>	0.40	0.35	0.33	<b>0.28</b>	0.26
$L_{x, roof}$ (m)		0.32	0.28	0.25	<b>0.22</b>	0.2

$f$  : full-scale equivalent  
 $e$  : estimated (Simiu and Scanlan 1996)  
 $m$ : measured

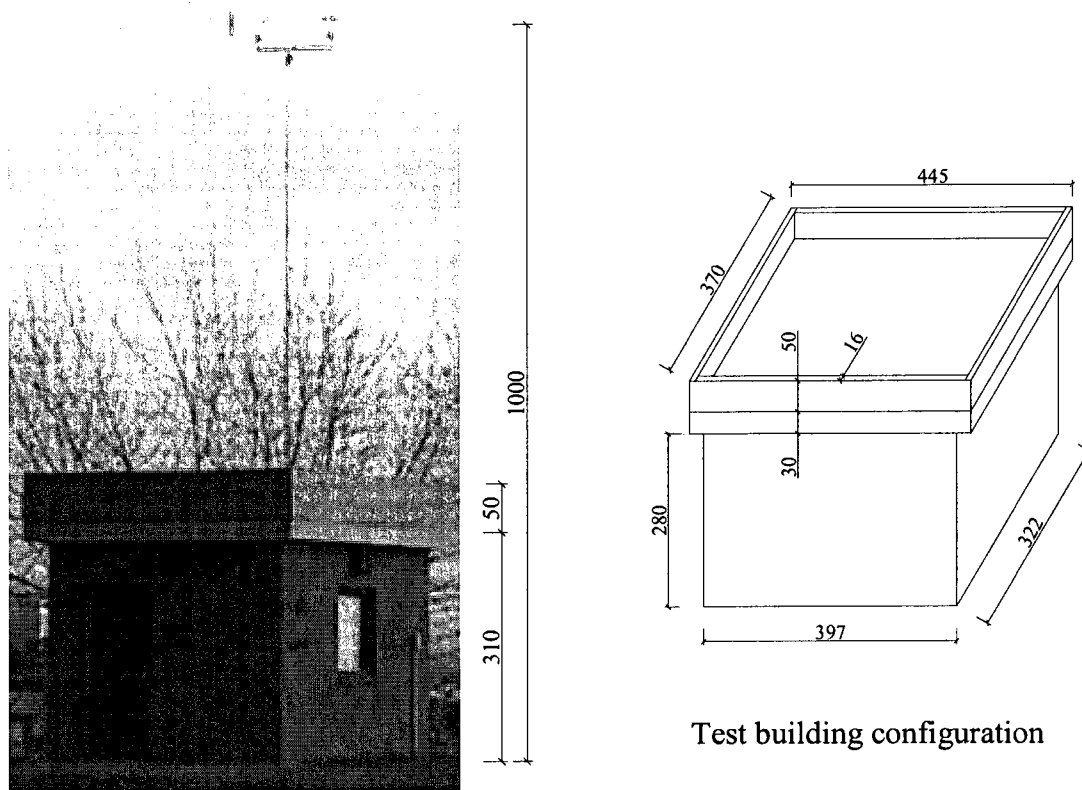
**Table 4.4: Wind tunnel modeling parameters used in the current study**

<b>Parameters</b>	<b>Measured values</b>
Model scale	1:50
Parapet height, $h_p$ (m)	0.01, 0.02
Reference height, $z_{ref}$ (m)	0.2
Power exponent parameter, $\alpha$	0.29
Roughness length, $z_o$ (m)	$0.08^f$
Gradient wind speed, $U_G$ (m/s)	12
Wind speed at roof height, $U_{roof}$ (m/s)	6.3
Turbulence intensity at $z_{ref}$ , $I_{ref}$ (%)	19
Turbulence intensity at roof height $I_{roof}$ (%)	28
Length scale of turbulence at $z_{ref}$ , $L_{x, ref}$ (m)	0.28
Length scale of turbulence at roof height, $L_{x, roof}$ (m)	0.22

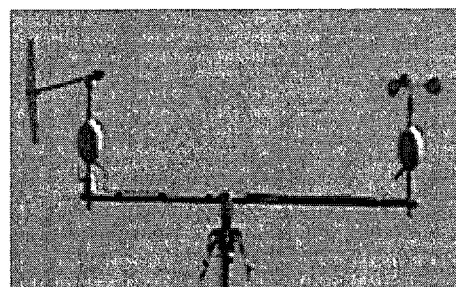
$f$  : full-scale equivalent



**Figure 4.1: Basic exposure of the experimental station (South-West)**

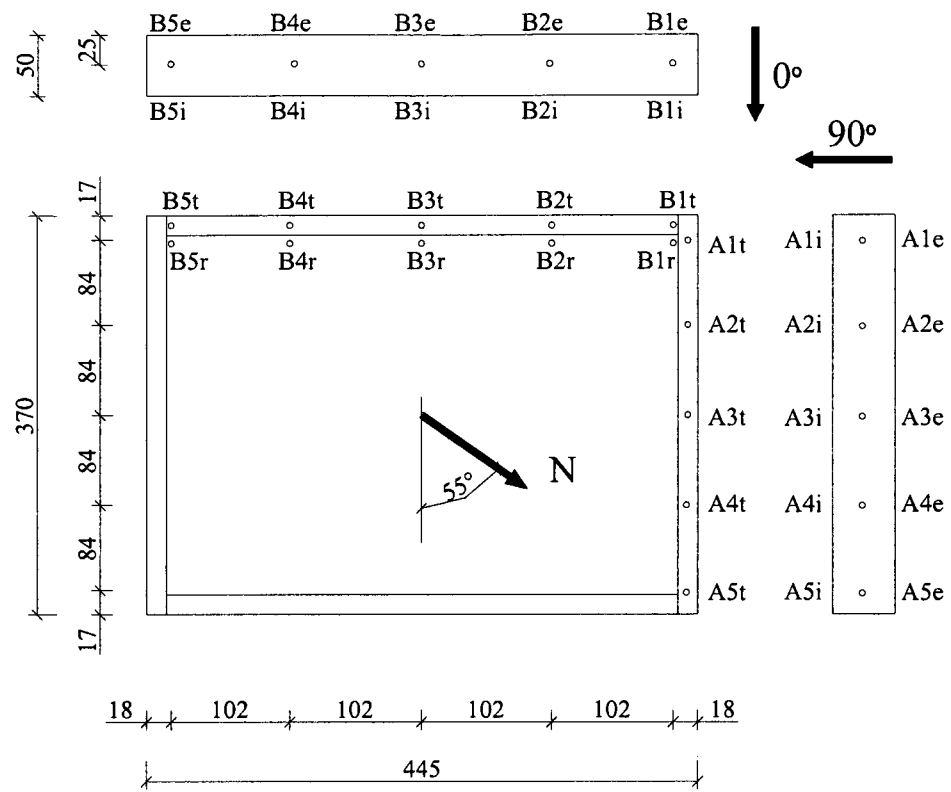


(Dimensions in cm.)

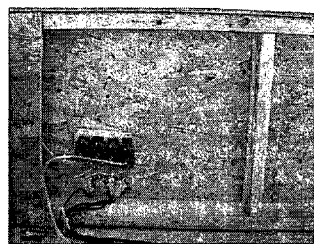


Anemometer and wind vane

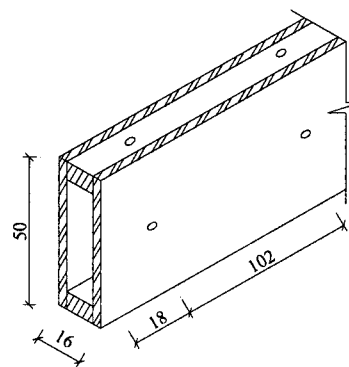
**Figure 4.2: Details of the test building.**



Tap locations



Pressure transducers



Parapet section

(Dimensions in cm)

Figure 4.3: Details of parapet section and tap locations.

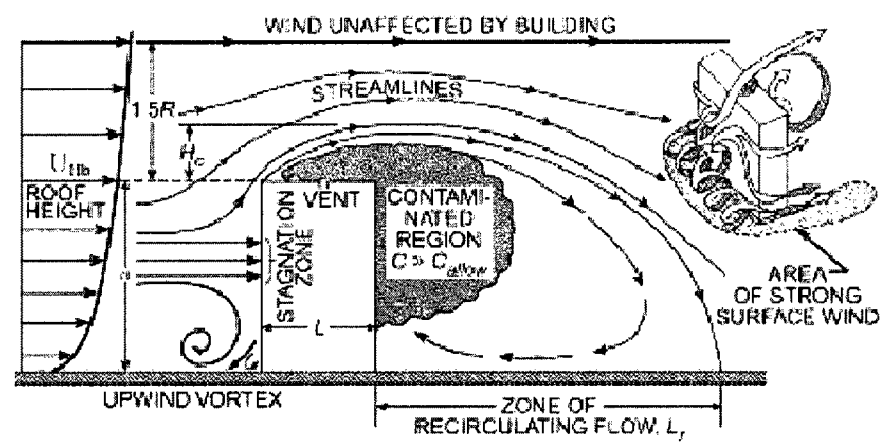
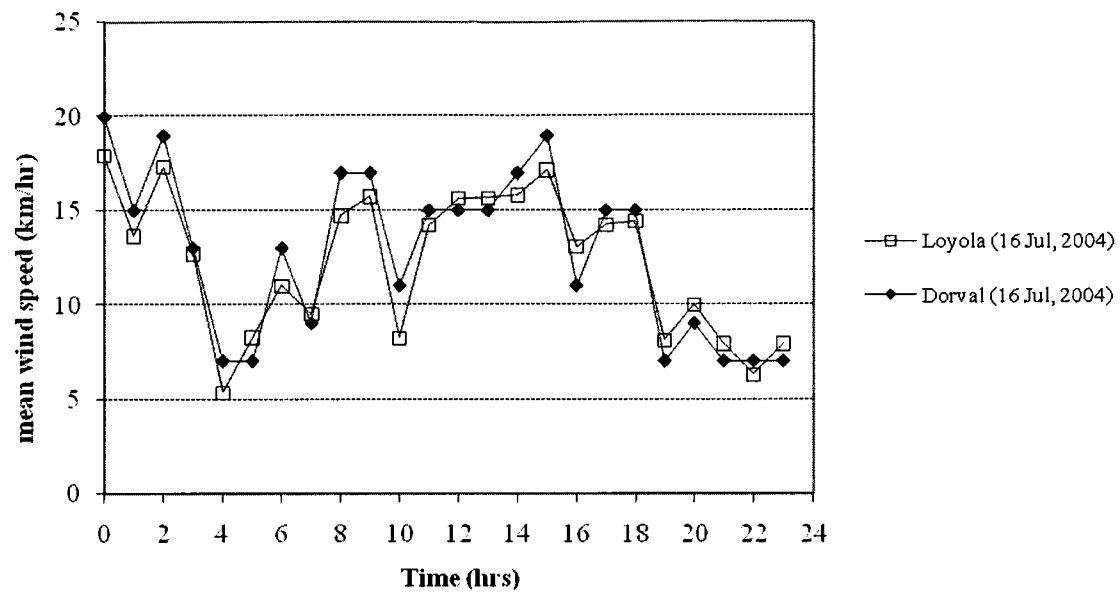
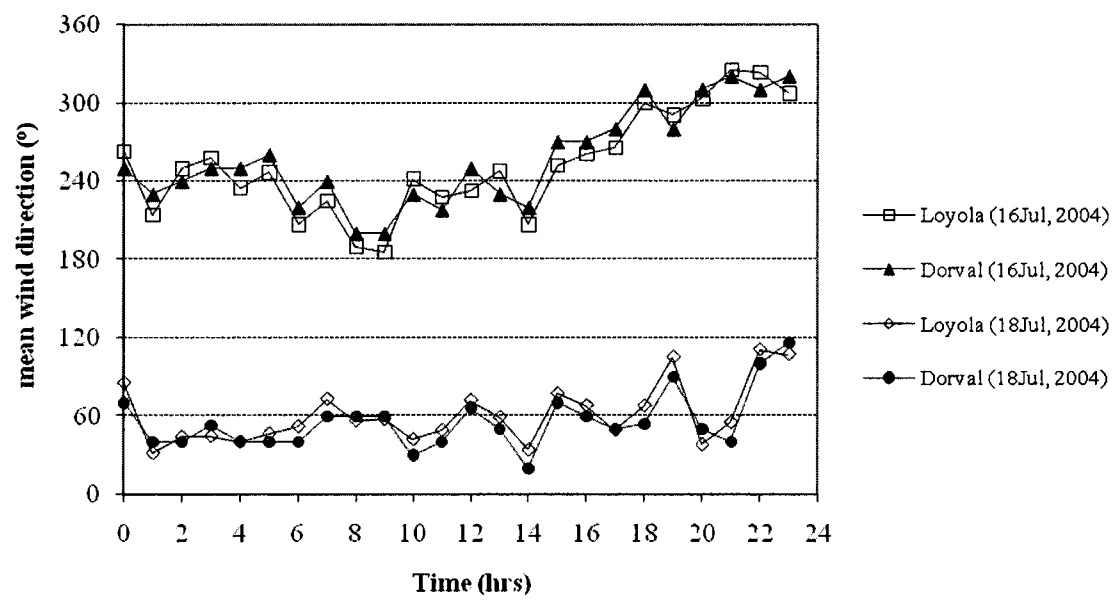


Figure 4.4: Flow patterns around a rectangular building (ASHRAE, 1999)

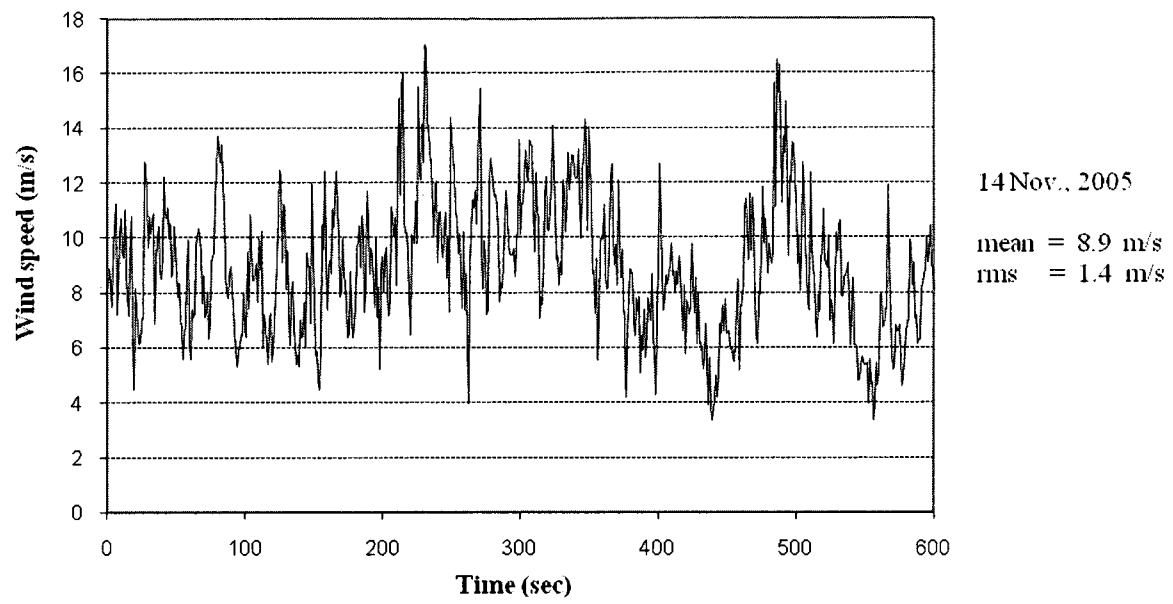


(a) Wind speed

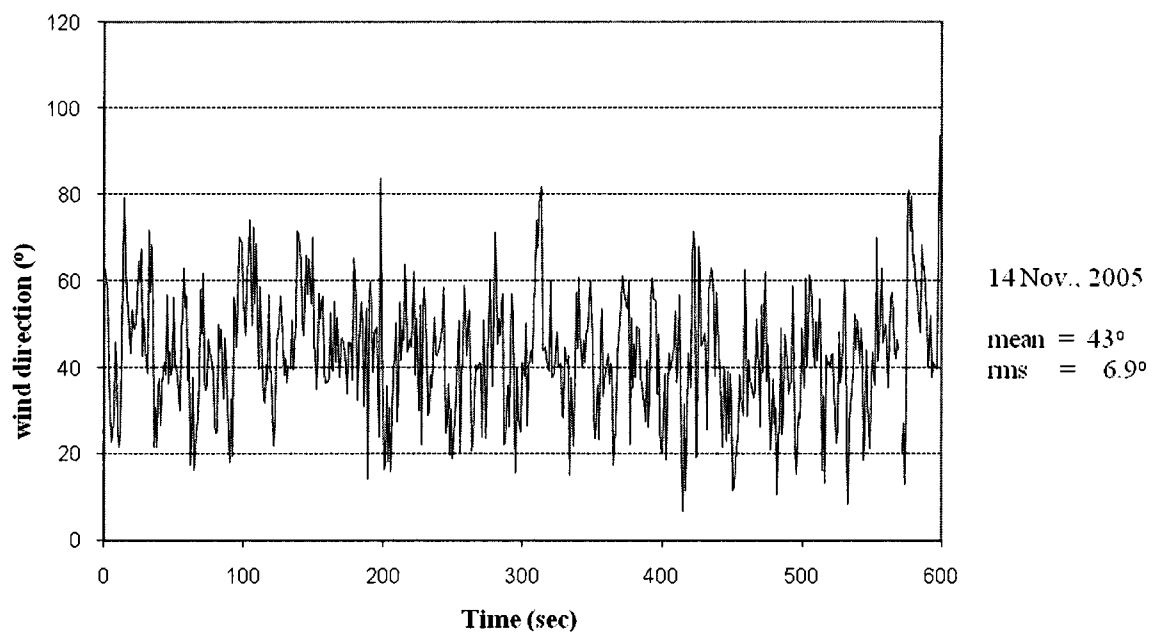


(b) Wind direction

**Figure 4.5: Mean wind speed and direction at the anemometer height, measured during 24 hours**

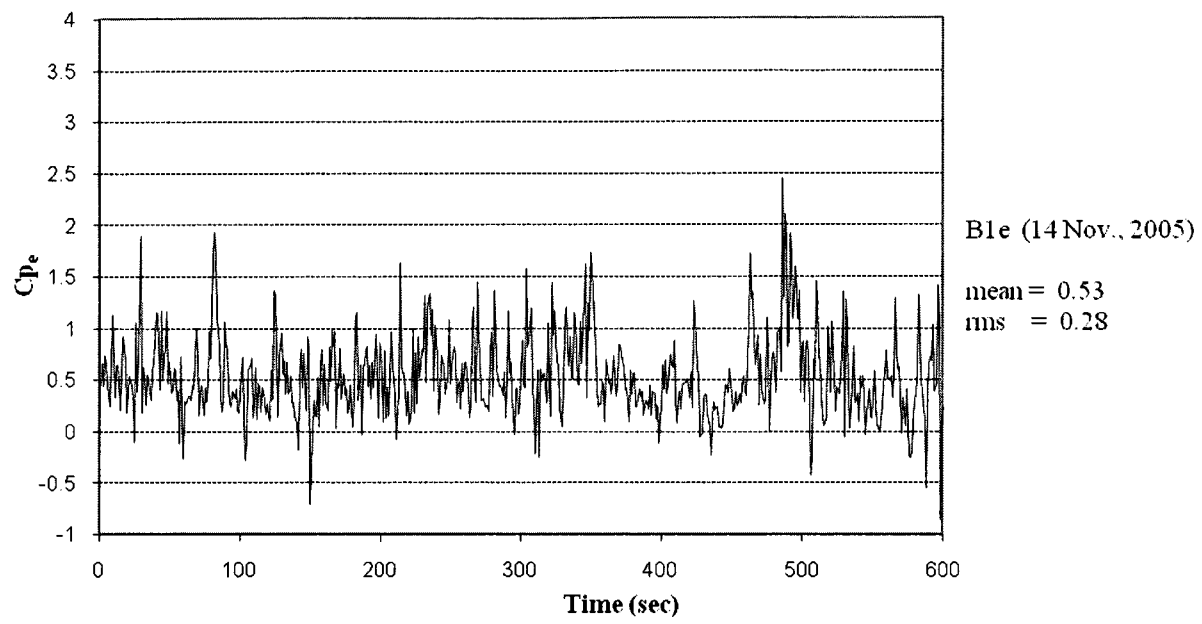


**(a) Wind speed**

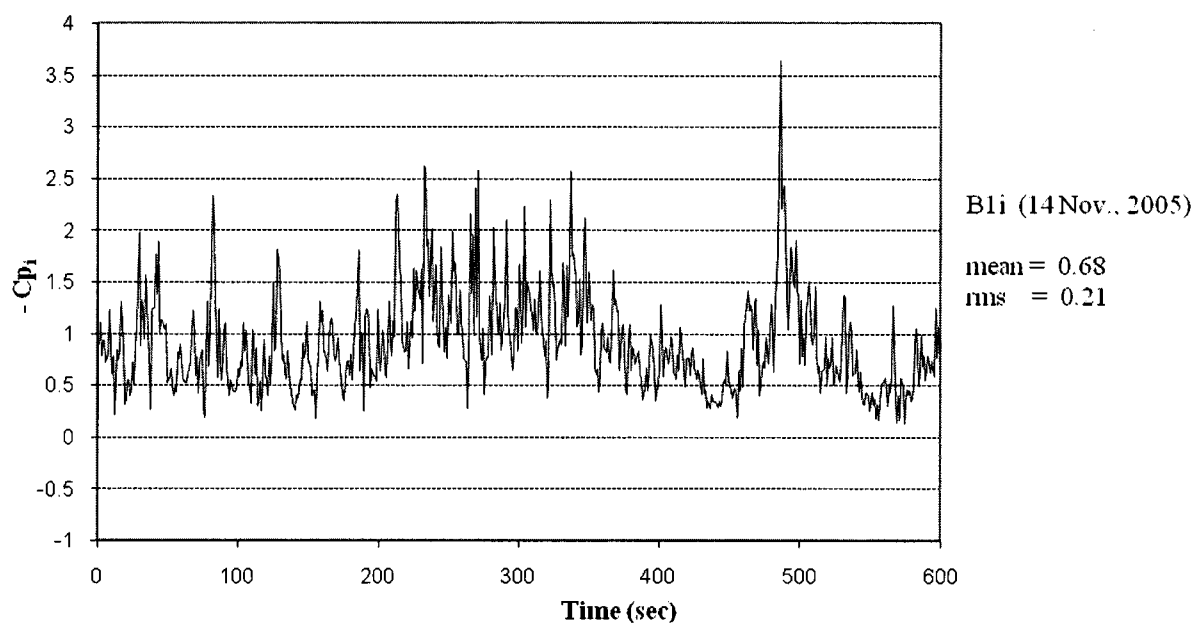


**(b) Wind direction**

**Figure 4.6: Typical time histories for wind speed and wind direction measured at the anemometer height**

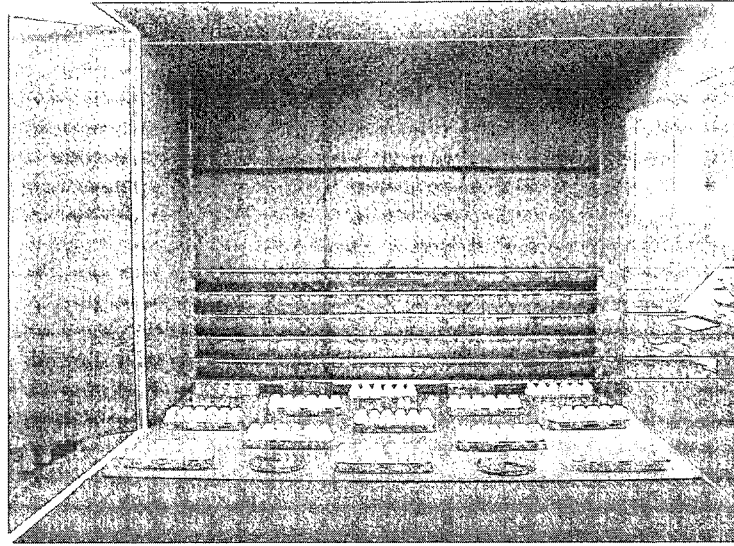


**(a) Exterior parapet surface pressure coefficient**

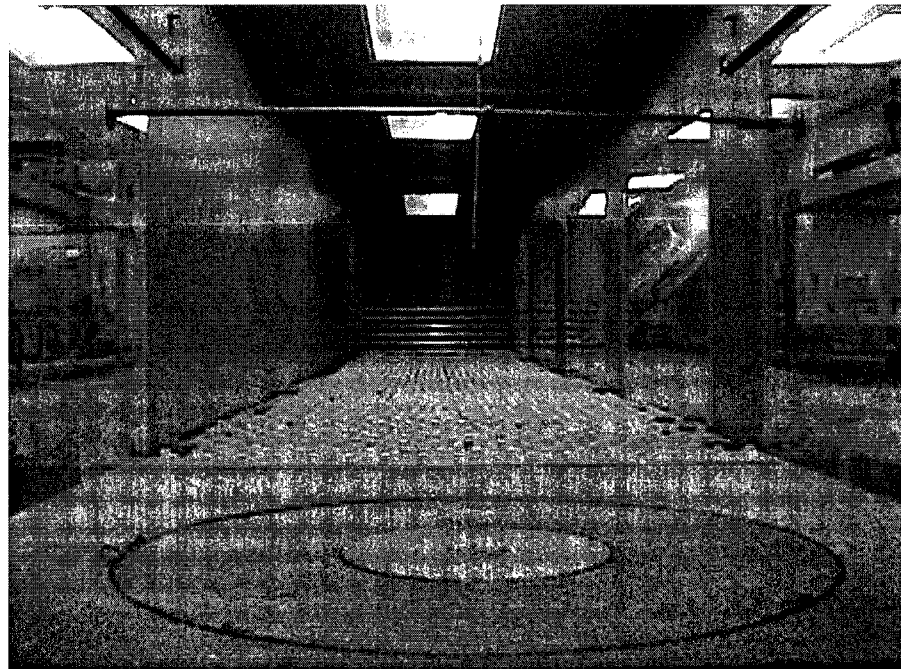


**(b) Interior parapet surface pressure coefficient**

**Figure 4.7: Typical time histories for parapet surface pressure coefficients**

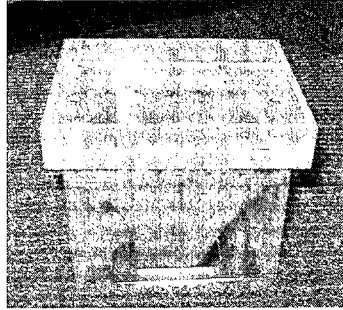


**(a) Wind tunnel inlet**

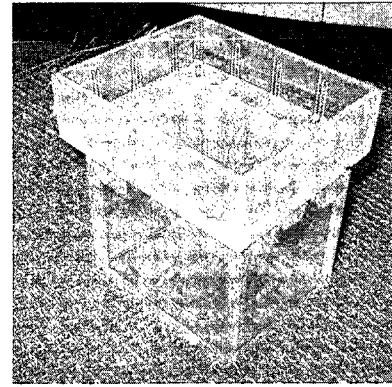


**(b) Inside view of the tunnel**

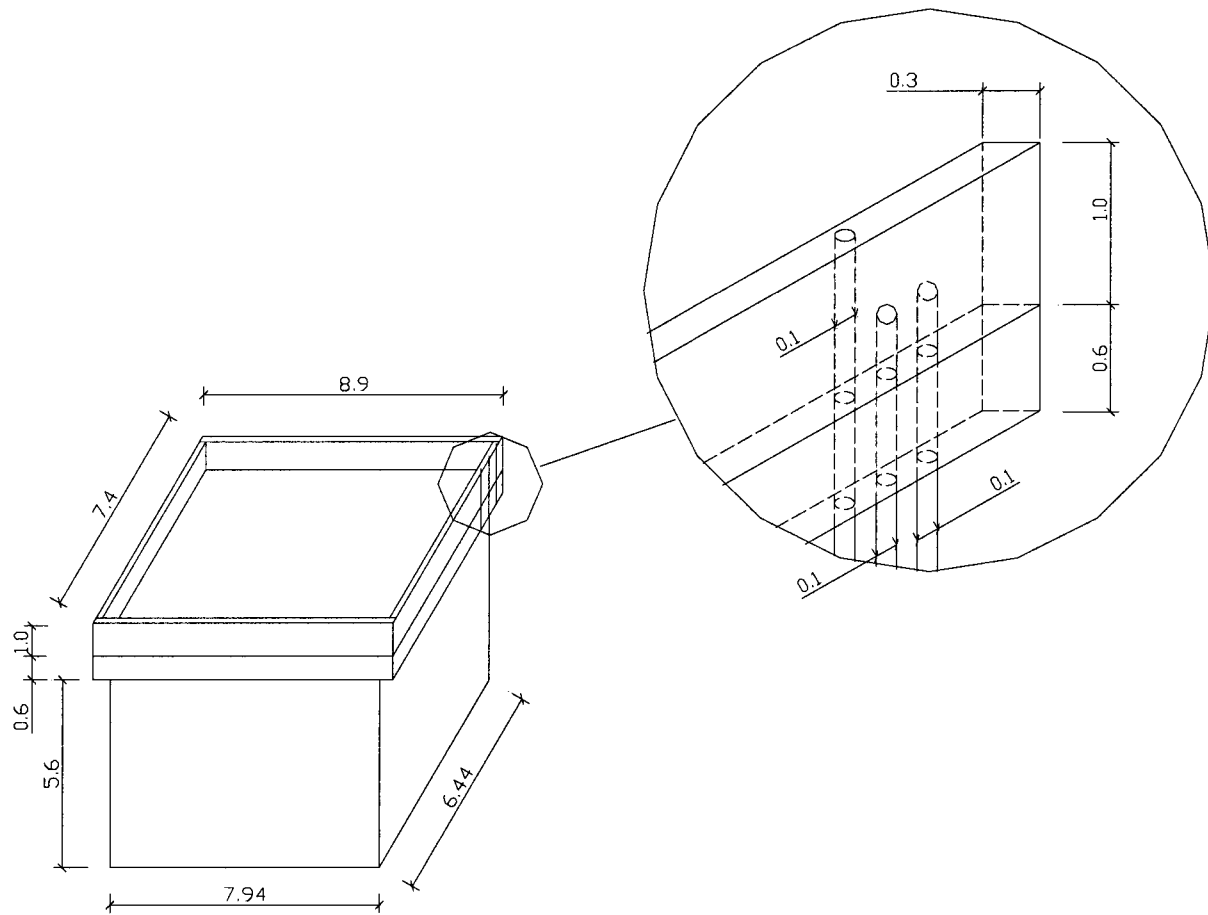
**Figure 4.8: The wind tunnel in simulated terrain**



**1 m high equivalent parapet**



**2 m high equivalent parapet**



(Dimensions in cm)

**Figure 4.9: Building models with different parapet heights**

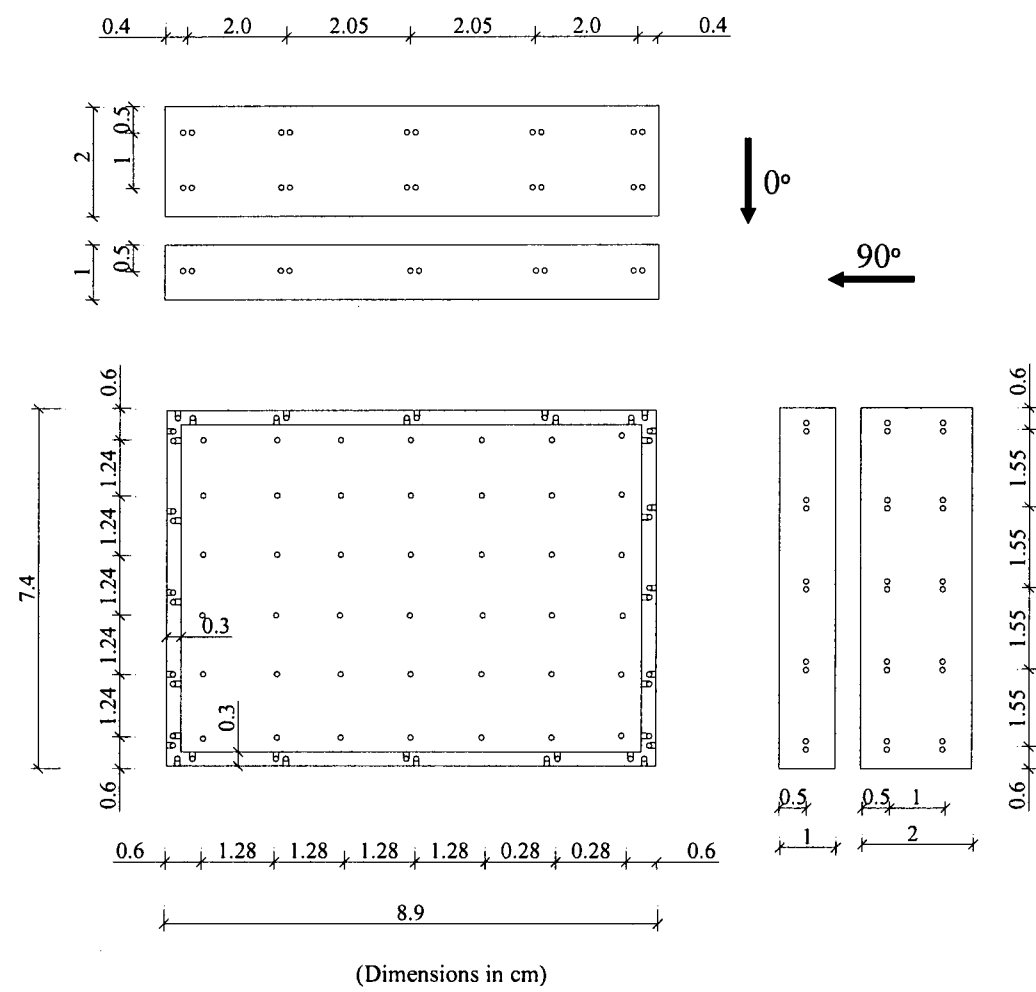
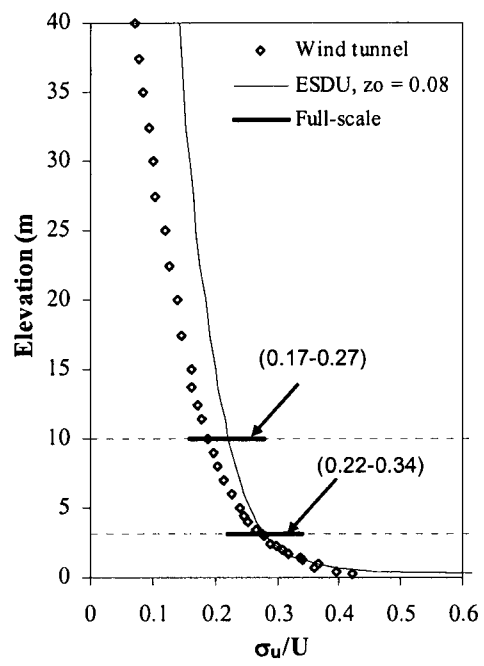
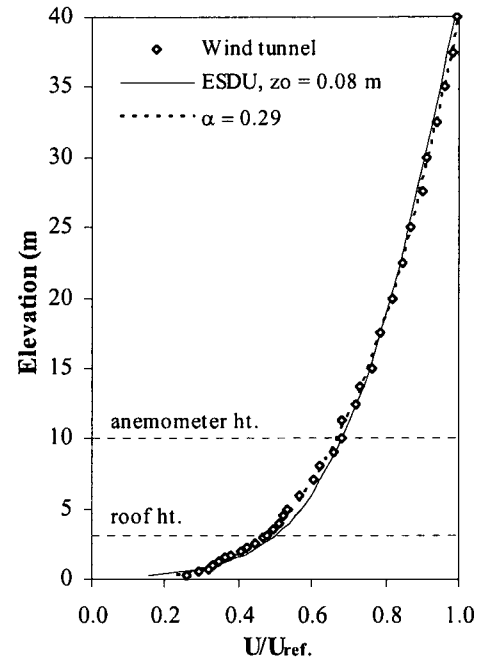


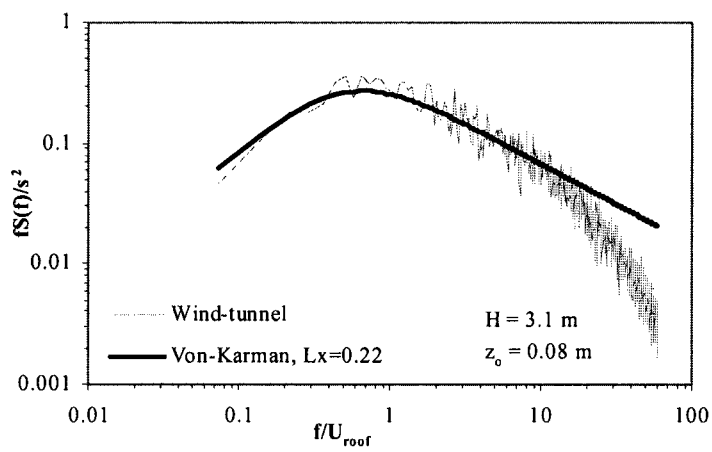
**Figure 4.10: Details of pressure tap layout of the building model**



(a) Turbulence intensity

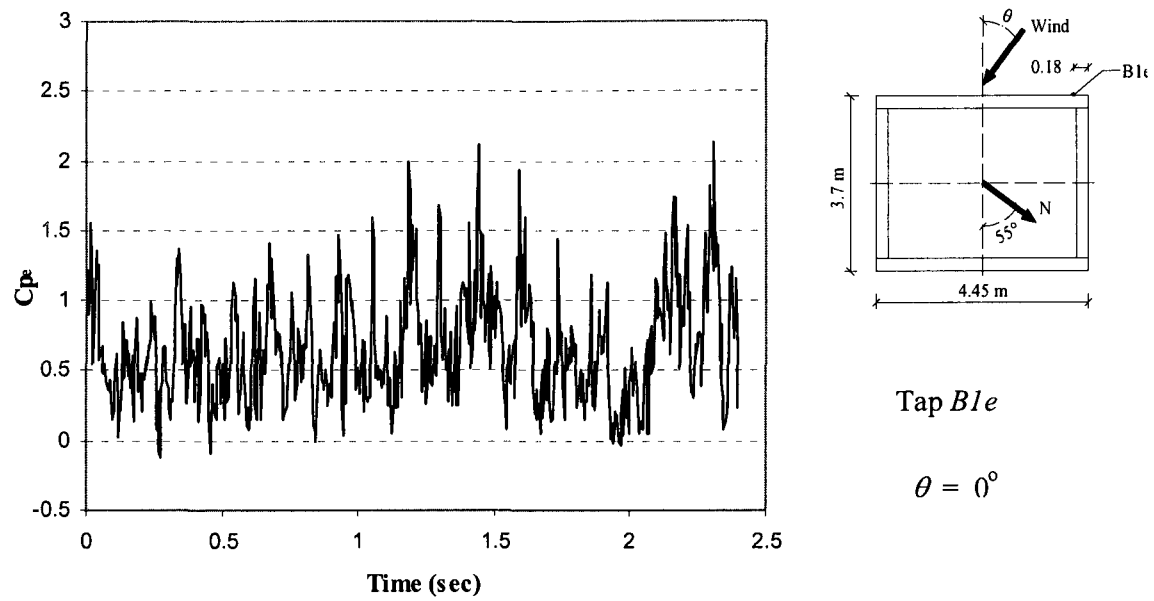


(b) Mean wind velocity

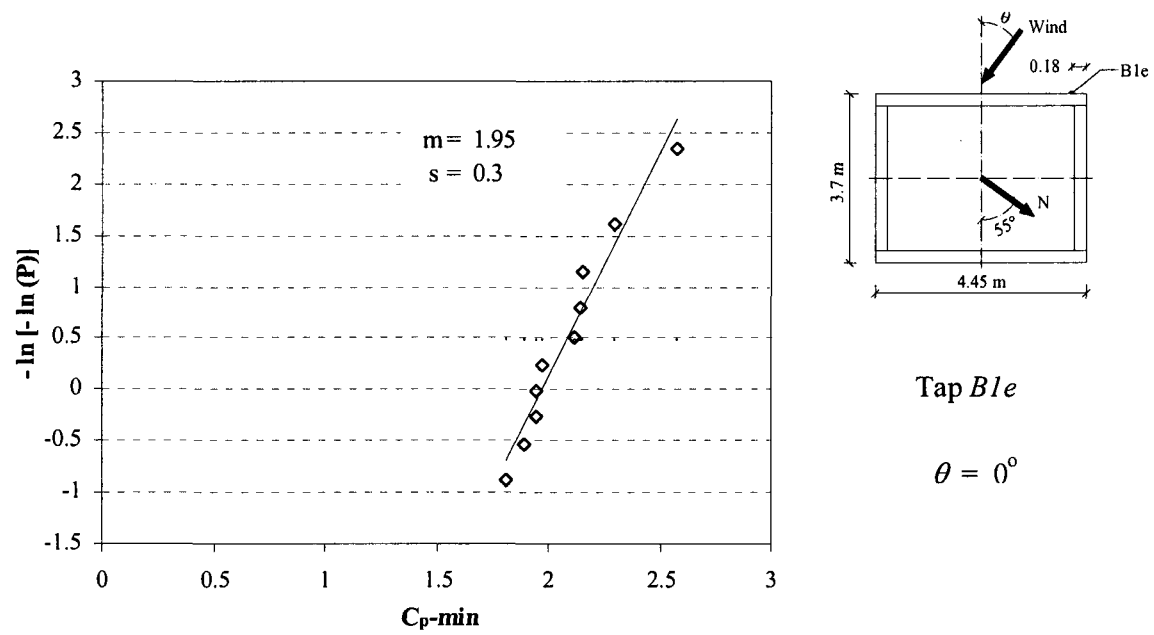


(c) Wind spectrum at the roof height

Figure 4.11: Profiles of turbulence intensity and mean velocity, and the spectrum at the roof height for Terrain-4



(a) Time history (600 data points)



(b) Gumbel plot

**Figure 4.12: Extreme value behavior for a segment of the  $C_p$  time history of Tap B1i for perpendicular wind direction.**

## *Chapter Five*

### **EXPERIMENTAL RESULTS AND COMPARISONS**

This chapter includes an analysis for all experimental results obtained from the wind tunnel (WT) and the full-scale (FS). Note that, all pressure data are presented in the form of pressure coefficients, normalized by using the dynamic pressure at roof height. Local surface pressures are measured on both exterior and interior parapet faces as well as on the roof edge surface. Area-average loading is recorded for different tributary effective areas. The wind tunnel results have been systematically compared with the full-scale collected data throughout the analysis of parapet surface pressure coefficients. Full-scale records for both positive and negative instantaneous peak pressures are displayed in a form of data ranges (error bars) and their averages. These divergences are due to unsteadiness of the direction of natural wind and the repeatability of the collected data. Note that, the lines connecting the data points for different wind angles have only been added for clarify purposes.

#### **5.1 Local Loading Coefficients**

The design of a parapet may require three feasible load cases: wind loads on the exterior parapet surface, the interior parapet surface and the net load on the parapet. The local fluctuating wind pressures on different parapet surfaces may be either towards the surface

(positive pressures) or away from the surface (negative pressures or suction). The net load on the parapet is defined as positive when it acts to push the parapet toward the roof surface and negative for the reverse.

Examining the individual surface pressures, Figure 5.1 presents instantaneous maximum and minimum pressure coefficients, as well as mean values, on both exterior and interior surfaces. Data are presented for exterior and interior taps,  $Bl_e$  and  $Bl_i$  respectively, which are located at the mid-height of the parapet and at a distance of 0.18 m from the leading corner.

Figure 5.1-a shows the effect of wind direction on local pressure coefficients on the exterior surface ( $C_{pe}$ ). For both wind tunnel and full-scale results, the maximum positive peak pressure occurred for winds approaching perpendicular to the parapet, while the minimum negative peak pressure occurred for winds approaching parallel to the parapet. The maximum full-scale positive peak coefficient of 2.4 occurred near  $\theta = 15^\circ$ , which is about 10 % higher than the wind tunnel pressure coefficient at the same wind angle. On the other hand, the maximum full-scale negative peak coefficient of  $-2.79$  occurred near  $\theta = 90^\circ$  in the separation zone down stream of the leading corner of the building. This value is about 15 % higher than the wind tunnel value.

Figure 5.1-b shows the effect of wind direction on local pressure coefficients on the interior parapet surface ( $C_{pi}$ ). The maximum negative peak pressure coefficient was found to occur at wind angles near  $\theta = 45^\circ$  to the face of the parapet. A full-scale

pressure coefficient of  $-3$  is recorded near  $\theta = 45^\circ$ , which is about 10 % more than the wind tunnel value. The high suction recorded on the interior parapet surface was due to the formation of sturdy vortices at the leading corner of the building, which is expected for this cornering wind. The maximum positive peak pressure generally occurred for wind perpendicular to the interior surface of the parapet (i.e.  $\theta = 180^\circ$ ). A full-scale positive peak  $C_{pi}$  of 2 was recorded in near  $\theta = 180^\circ$ .

Pressures were also measured at mid-span location on the exterior and interior parapet surfaces, tap  $B3_e$  and  $B3_i$  respectively. Figure 5.2-a shows that the maximum positive peak pressure on the exterior surface occurred, also, for winds approaching perpendicular to the parapet. A full-scale peak positive coefficient of 2.28 occurred near  $\theta = 0^\circ$ , which is about 5 % lower than the wind tunnel pressure coefficient. The maximum negative peak pressure occurred for winds approaching parallel to the parapet. A peak negative coefficient of  $-2.43$  occurred near  $\theta = 90^\circ$ . This value is approximately equal to the wind tunnel result.

Figure 5.2-b shows that the maximum negative peak pressure coefficient on the interior surface occurred for winds parallel to the face of the parapet. A full-scale value of  $-2.3$  was recorded near  $\theta = 90^\circ$ , which is matching the wind tunnel results. A maximum positive peak pressure of 2.2 occurred near  $\theta = 135^\circ$ , approximately 10 % higher than the wind tunnel value. Generally, mean pressure coefficients measured in the wind tunnel show very good agreement with the full-scale results except some discrepancies at wind angle of  $180^\circ$ . Considering peak pressure coefficients, a difference of 10 - 15% is

observed particularly at critical wind directions. However, the overall data shows good agreement between wind tunnel and full-scale.

As mentioned in Chapter two, the method used by some standards for estimating parapet loads is to assume the inside local pressure on the parapet is equivalent to the local roof pressure obtained at a tap next to the parapet edge. In the present field testing, roof tapings are installed along side *B* at a distance of 0.025 m from the edge of the parapet section. Mean and peak pressure coefficients on the roof ( $C_{p,r}$ ) and the inside surface of the parapet ( $C_{p,i}$ ) are compared. Figure 5.3 shows the results at the corner, while Figure 5.4 shows the results at mid-span. For both locations, the mean pressures on the roof and inside parapet tapping are almost equal for all wind azimuths, while some discrepancy is found in both positive and negative peak pressures for specific wind directions. The negative peak pressures at the corner measured on the roof are approximately 10 - 15 % higher than those on the inside parapet surface. At mid-span location, negative peak pressures on the roof were also 10 -15 % higher than those on the inside parapet surface. Positive peak pressures are almost very close, for both locations, although a discrepancy up to 50 % was found for wind angles of 135° and 180°, while the pressures on the inside surface of the parapet are relatively high.

#### **5.1.1 Correlation of pressures on the roof and the interior parapet surface**

In the absence of design loads for parapets, a designer might use roof edge or corner design loads to estimate the suction on the inside surface of the parapet. However, this

may significantly overestimate the peak suction since the roof design point loads are the maximum loads in a corner or edge region and thus may not correspond to the load very close to the edge. Another factor that may be important when using roof edge pressure to evaluate the wind load on a parapet, is the correlation of the roof pressure fluctuations with those on the inside surface of the parapet. The total fluctuating load on the parapet is obtained from the pressure difference between the outside and inside faces of the parapet, measured simultaneously. Perfect correlation between pressures on the inside surface of the parapet and the roof edge pressures would be necessary to replace the one with the other and keep equivalence.

Figure 5.5 shows cross-correlation coefficient,  $R$ , between pressures measured on the roof edge and interior parapet surface at corner and mid-span locations, respectively for wind directions of  $0^\circ - 180^\circ$ . The present data (equivalent full-scale  $h_p = 0.5$  m;  $h_p/H = 0.16$ ;  $x/L = 0.04$ ) are compared with those from Stathopoulos et al., 2002-a (equivalent full-scale  $h_p = 1$  m;  $h_p/H = 0.13$ ;  $x/L = 0.08$ ), see table 5.1. The present data indicates that the correlation is relatively high, approximately 0.9 for both locations, at  $90^\circ$ . However, the correlation decreases to a minimum of 0.75 and 0.63 at  $60^\circ$  for corner mid-span locations, respectively. It is likely that the correlation between roof and interior parapet surface pressures depends somewhat on the location of the roof tapping. The vortices that produce the significant pressure fluctuations travel downstream from the separation point at some fraction of the free stream velocity. Thus, there will be a time lag between a pressure drops near the edge compared to that occurring some distance away from the edge. This will result in some loss of correlation between parapet and roof pressures.

Furthermore, for oblique wind angles ( $30^\circ$ - $60^\circ$ ) a time lag is expected between parapet and roof instantaneous pressures due to lateral movement of the delta-wing vortices. This time lag will reduce the correlation of the pressure signals. At the corner location, the lateral movement is small and thus the correlation is relatively high. On the other hand, at the mid-span location, the vortices have large lateral movement and the correlation is relatively low. It should be noted that, similar performance was found by Stathopoulos et al, 2002-a as shown in Figure 5.5. However, for oblique wind angle the correlation reduces to 0.7 and 0.57 for corner and mid-span locations, respectively. As the correlation values depend on the tap location, it is expected that higher correlation can be obtained for roof tapping closer to the edge, i.e. parapet, which is the case of the present testing. This may explain the difference in correlation between the two studies

### **5.1.2 Correlation of pressures on the exterior and interior parapet surface**

The local fluctuating wind load on a parapet may be either toward the roof (exterior parapet surface pressure) or away from the roof (interior parapet surface pressure). As a first approximation, the peak local load on a parapet  $\Delta C_p$  may be estimated by taking the difference between peak pressure values on both surfaces. However, this requires that these peak values occur simultaneously, i.e. very good correlation between the measured pressure on the inside and outside parapet surfaces is assumed. Therefore, the correlation coefficients of  $C_{Pe}$  and  $C_{Pi}$  for all wind directions, at five tap locations along the parapet, are evaluated below.

Figure 5.6-a shows wind tunnel results while Figure 5.6-b shows full-scale data. The overall correlation between  $C_{Pe}$  and  $C_{Pi}$  is relatively low. Maximum positive value of 0.5 was found for wind direction perpendicular to the parapet surface ( $\theta = 0^\circ$ ) for all tap locations; i.e. the absolute maximum peak pressures do not occur simultaneously on the exterior and interior parapet surfaces. Therefore, net peak pressure coefficients may be calculated only by taking the simultaneous difference between  $C_{Pe}$  and  $C_{Pi}$ . Generally, although there are some differences in the individual values, the correlation coefficients between exterior and interior pressures measured in wind tunnel shows good agreement with the respective set of full-scale data.

### 5.1.3 Total local loading coefficients on parapets

The net peak pressure coefficients ( $\Delta C_p$ ) on a parapet were estimated by taking the difference between peak pressure values on the outside and inside surfaces of the parapet. For positive and negative load respectively:  $\Delta C_p \sim (C_{Pe\_max} - C_{Pi\_min})$  and  $(C_{Pe\_min} - C_{Pi\_max})$ . This approximate value of  $\Delta C_p$  is expected to be larger than the actual value since the maximum and minimum pressure coefficients do not occur simultaneously. The most representative evaluation of  $\Delta C_p$  is obtained by taking the simultaneous peak pressure difference between the exterior and the interior surface of a parapet as follows:

$$\Delta C_p = (C_{Pe\_max-inst.} - C_{Pi\_min-inst.})_{simultaneous} \quad (5.1)$$

Figures 5.8-a and 5.8-b show the variation of both inward (positive) and outward (negative)  $\Delta C_p$  with wind direction at the corner and mid-span locations, respectively. Two curves are shown for each peak pressures, one was obtained with the simultaneous

peak pressure difference and the other was obtained with the non-simultaneous peak pressure difference calculated from the data shown in Figures 5.1 and 5.2. As expected, data shows significant differences between simultaneous and non-simultaneous  $\Delta C_P$  values. Considering the simultaneous peak pressures at the corner (Figure 5.7-a), the maximum positive (inward) pressure coefficient occurred near  $\theta = 45^\circ$  while the maximum negative (outward) pressure coefficient occurred near  $\theta = 180^\circ$ . Clearly, the maximum negative and positive coefficients occur at the same azimuth as the coefficients of interior parapet surface. This indicates that the pressure on the interior surface dominates the net loading at this point of the parapet. However, the positive pressures on the exterior surface make an important contribution, since the net windward coefficients are 35 % higher than those on the interior surface. Figure 5.7-b shows that the maximum positive peak coefficients ( $\Delta C_{P, \text{ simultaneous}}$ ) occurs near  $\theta = 30^\circ$ , while the maximum negative peak coefficient occurred near  $\theta = 135^\circ$ .

#### 5.1.4 Parapet pressures: full-scale versus wind tunnel

A comparison between the pressure coefficients measured in full-scale and the corresponding data obtained from the wind tunnel is shown in Figure 5.8. Mean and peak pressure coefficients for all taps and critical wind directions are plotted in the figure, which represents 265 data points all together. The solid line represents the linear regression line for  $C_p$ , FS and WT, ( $y = 1.012 x + 0.019$ ), while the dotted line represents the  $45^\circ$  line ( $y = x$ ). The figure shows the agreement between full-scale and wind tunnel results. Although, there is some dispersion near  $45^\circ$  and  $135^\circ$  wind directions, the overall

agreement seems to be excellent taking into consideration the unsteadiness of the direction of natural wind.

### 5.1.5 Comparisons with other studies

Figure 5.9 presents instantaneous maximum and minimum peak pressures measured at a single corner point. The current full-scale results were compared with three different studies. Table 5.1 presents the main characteristics of different models used in each study. Note that although the pressure coefficients in the study of Mans were referenced to the mean dynamic wind speed at a height of  $H + h_p$ , the data presented here were referenced to the mean dynamic wind speed at roof height to match that in the present study. Regarding tap location, for the present study  $x/L$  and  $\zeta/h_p$  were 0.04 and 0.5 respectively, where  $x$  is the distance from the leading corner and  $\zeta$  is the vertical distance from the base of the parapet. The tap locations presented in Stathopoulos, 2001 and 2002, are  $x/L = 0.08$  and  $\zeta/h_p = 0.4$ , while those presented in Mans et al, 2005, are  $x/L = 0.06$  and  $\zeta/h_p = 0.83$ .

Figure 5.9-a shows the coefficients on the exterior surface. A clear difference is shown for Mans' results (particularly for wind azimuth near  $45^\circ$ ); where positive peak coefficients are lower than those of the other three studies. This difference may be attributed to the difference in tap location (the distance from the base of the parapet). In the experiments of Mans et al. (2005) the tap is located relatively close to the top of the parapet ( $\zeta/h_p = 0.83$ ), where the pressure on the exterior surface is expected to mitigate;

while in the current study and Stathopoulos et al. (2002-a) the tap is located at the mid height of the parapet. Note that, a similar explanation was suggested in Mans et al, 2005. In contrast, negative peak coefficients of Mans are higher than the other studies. Figure 5.9-b shows peak pressure coefficients for the interior surface of the parapet. The most evident discrepancy between all studies is for the worst suction. It is clear that the current results match the Stathopoulos et al. (2002-a) study, which has also equal building length and height ( $L/H = 1$ ) and relatively high parapet with respect to building height ( $h_p/H = 0.13$ ). Moreover, Mans et al. (2005) and Stathopoulos et al. (2002-b,  $L/H = 3$ ) data show reasonable agreement for the most critical suction, although, higher coefficients than those of the current study, by a factor of 2, were found. This difference may be due to the fact that suction on the interior surface of the parapet are dependent on the minimum distance required for flow reattachment to occur, after separation at the leading edge of the parapet. The building dimensions of Mans et al. (2005) study allow for reattachment to occur on roof surface. However, flow reattachment may not occur on the roof of a building with a reduced length/width ratio and high parapet, as is the case of the present study. Consequently, most of wind flow passes above the parapet with small circulation down stream (at the interior face). This will significantly reduce the suction on the interior surface of the parapet.

The comparison, also, suggests that worst suction on the interior surface depend on the ratio of building length to its height ( $L/H$ ). Figure 5.9-c compares the net peak pressures on the parapet measured simultaneously. The worst net pressure occurs at wind azimuth  $45^\circ$  for all cases; that indicates that suction on the interior surface dominate the net

loading on the parapet, as mentioned previously. Very good agreement is shown between the current study and Stathopoulos et al. (2002-a,  $L/H = 1$ ). However, for building with ( $L/H = 3$ ) and the study of Mans et al. (2005) pressure coefficients are about 40 % and 20 %, respectively, higher than those of the current study. It is clear that Mans et al. (2005) data shows that the interior suction is controlling the net loading with almost no contribution of the external pressure, which is not the case of Stathopoulos et al. (2002-b,  $L/H = 3$ ) and the present study, as already discussed in section 5.1.2. Although, comparison results are generally good, there are some cases with some differences.

#### 5.1.6 Comparison with NBCC (2005)

Currently, no provision exists in the National Building Code of Canada (NBCC) for the design wind loads of parapets. In this case, it can be recommended that the parapet load be determined using the design wind loads for the windward wall and for the roof. Table 5.2 shows the current coefficients, measured in full-scale and wind tunnel, and those derived from the NBCC provisions using this method. The design force coefficient ( $C_F$ ) for a particular region (corner or edge) of a parapet is given by:

$$(C_F)_{parapet} = (C_p C_g)_{wall} - (C_p C_g)_{roof} \quad (5.2)$$

where  $C_p C_g$  is the design pressure coefficient.  $(C_F)_{parapet}$  for the present study is determined by multiplying the measured values of  $(C_{Pe\_max-inst.} - C_{Pi\_min-inst.})_{simultaneous}$  by 0.8 (directionality factor) as it occurs with all  $C_p C_g$  values in the NBCC. The value of  $(C_F)_{parapet}$  for the corner region, based on the NBCC provisions, is significantly greater than the measured force coefficient (about 45%), however; less difference (about 20 –

30%) is found between those values in mid-span location. The overestimation of  $(C_F)_{parapet}$  by NBCC method is due to the fact that the values of  $(C_p C_g)_{wall}$  and  $(C_p C_g)_{roof}$  are both greater than the maximum  $C_p C_g$  on either side of the parapet. This can mostly be as a result of the fluctuating pressures on the exterior and interior surfaces of the parapet are uncorrelated, as explained in section 5.1.1. Therefore, it is not practical to use the critical wall and roof values to estimate the total peak load. Based on a wind tunnel testing of different building and parapet configurations, Stathopoulos et al. (2002-a) shows similar trend.

## 5.2 Area-averaged Pressure Coefficients

Design of cladding and other structures and non-structured elements requires spatially-averaged coefficients over a variety of areas. Area-averaged coefficients were derived by simultaneously integrating the recorded pressures for a group of taps according to:

$$C_P = \frac{\sum_{j=1}^n C_{Pj} l_j h_j}{\sum l_j h_j} \quad 5.3$$

where:  $n$  is the number of taps,  $C_{Pj}$  is the pressure coefficient on the individual tap,  $l_j$  is the tributary length of the tap and  $h_j$  is the tributary height of the tap. For each loaded area coefficients were developed for all suitable tap combinations. Subsequently, the largest maximum and minimum coefficients were obtained. Coefficients were calculated separately for both exterior and interior parapet surfaces. The analysis was repeated for the combined action from both surfaces, which was calculated instantaneously using the same loaded area and location.

Figure 5.10 depicts the worst negative and positive peak coefficients for three load cases. Full-scale data were compared with the wind tunnel results of two different parapet heights. As expected, for all cases both positive and negative load coefficients tend to decrease with increasing load area. Examining area loading on the exterior surface, Figure 5.10-a shows that positive peak coefficients tend to increase with parapet height as the 1 m parapet loads are about 10 % higher than those recorded on the 0.5 m parapet. In contrast, negative peak loading coefficients on the 1 m parapet are about 10-15% less than those on the 0.5 m parapet. The positive and negative full-scale area loads were found to be approximately 18% less than the wind tunnel loads of the parapet with the same height (0.5 m).

Figure 5.10-b compares peak coefficients on the interior parapet surface as function of tributary (effective) area. For relatively small areas, less than 1 m<sup>2</sup>, the positive coefficients tend to increase with parapet height, while the negative coefficients tend to somewhat decrease with increasing parapet height. This is consistent with the results from the literature, which found that taller parapets reduce the largest suction pressure on the building roof (Kind, 1988; Kareem and Lu, 1992; Stathopoulos and Baskaran, 1987; Mans, 2003). A difference of about 10% was found. The positive and negative full-scale area loading coefficients are in good agreement with the wind tunnel coefficients.

The combined action from both parapet surfaces is presented in Figure 5.10-c. The worst peak positive loading coefficient occurs on the 1 m parapet, while the worst negative

peak occurs on the 0.5 m parapet, particularly for areas greater than 1 m<sup>2</sup>. The full-scale positive peak coefficients match well the wind tunnel results for the same parapet height, while the negative peaks are approximately 30% greater than those recorded in the wind tunnel.

### 5.2.1 Comparisons with the ASCE 7-05

In the absence of research, the ASCE 7-05 recommends the following equation for the design wind pressure on the component and cladding elements of parapets:

$$p = q_p (GC_{pe} - GC_{pi}) \quad 5.4$$

where:  $q_p$  is the velocity pressure evaluated at the top of the parapet,  $GC_{pe}$  is the external pressure coefficient and  $GC_{pi}$  is the internal pressure coefficient (see Appendix B for details). Two load cases should be considered. In Load Case A (windward parapet), the positive wall pressures are applied to the exterior surface while negative roof edge or corner pressures are applied to the interior surface. In Load Case B (leeward parapet), the positive wall pressure is applied to the interior parapet surface while the negative wall pressure is applied to the exterior surface. The measured data are referenced to the 3-sec. velocity pressure at 10 m height to be consistent with the ASCE 7-05 format according to the following form:

$$(GC_p)_{eq} = \frac{q_H}{q_{10m,3s}} \hat{C}_p \quad 5.5$$

where  $(GC_p)_{eq}$  is the equivalent measured pressure coefficient,  $\hat{C}_p$  is the peak coefficient (maxima or minima) based on the mean wind pressure at the roof height ( $q_H$ ) and  $q_{10m,3s}$  is

the basic wind pressure in the ASCE 7-05. As the code provides different factors for the edge and interior regions, the comparisons are presented in two different figures. Figure 7.10 compares the ASCE 7-05  $GC_p$  for wall edge and roof corner regions with those on the exterior and interior surfaces of the parapet edge, respectively.

In Figure 5.11-a the exterior surface loads on parapet edge are compared with the  $GC_p$  values on 'wall edge zone' obtained from ASCE 7-05 (Appendix B, Figure B1). The negative 'wall edge zone' coefficient suggested by the standard covers the negative surface pressure coefficients on parapet edge. However, the positive 'wall edge zone' coefficient underestimates the positive surface pressure coefficients by 20 %.

Figure 5.11-b shows the  $(GC_p)_{eq}$  values for the interior surface of parapet edge and those for the roof corner zone obtained from ASCE 7-05 (Appendix B, Figure B2). The negative 'roof corner zone' coefficient overestimates the negative surface pressure coefficients on parapet edge by about 40%. On the other hand, the positive 'wall edge zone' coefficient adequately envelops the positive surface pressure coefficients.

The net loading from both parapet surfaces is presented in Figure 7.11-c. The 'edge zone' coefficient for the Load Case A overestimates the net positive pressure coefficients on the edge of windward parapet by about 50%. The 'edge zone' coefficient for Load Case B overestimates the net negative pressure coefficients on the edge of leeward parapet by about 30%.

A similar comparison was made in Figure 5.12 between wall interior and roof edge regions and the parapet mid-span. In Figure 5.12-a the exterior surface loads on the parapet mid-span are compared with the  $GC_p$  values for 'wall interior zone' obtained from ASCE 7-05 (Appendix B, Figure B1). The negative 'wall interior zone' coefficient found to overestimate the negative surface pressure coefficients on parapet mid-span by 10 – 35%. However, the positive 'wall interior zone' coefficient underestimates the positive surface pressure coefficients by 10 – 30%.

Figure 5.12-b shows the equivalent  $GC_p$  values for the interior surface of parapet interior region compared with those for roof edge zone obtained from ASCE 7-05 (Appendix B, Figure B2). The negative 'roof edge zone' coefficient overestimates the negative surface pressure coefficients on parapet mid-span by 35%. In addition, the positive 'wall interior zone' coefficient overestimates the positive surface pressures by 25%.

The net loading from both parapet surfaces is presented in Figure 5.12-c. For Load Case A, the 'interior zone' coefficient overestimates the net positive pressure coefficients on the mid-span of wind-ward parapet by 25% and 40% for the higher and lower parapet, respectively. For Load Case B, the 'interior zone' coefficient overestimates the net negative pressure coefficients on the mid-span by 30% and 20% for the higher and lower parapet, respectively.

Generally, the comparisons of the results of the present study with the ASCE 7-05 provisions shows the latter to be on the conservative side for most cases. However, the

provisions underestimate the positive pressure coefficients on the exterior parapet surface. The overall approach adopted within the standards, which utilizes the area-averaged pressure coefficients from the wall and roof of the building, was found to significantly overestimate the combined effect from both surfaces. This is attributed to poor correlation between the exterior and interior surface pressures, i.e. the peak pressures on both surfaces do not occur simultaneously, as shown before.

Based on the results of the present study, the following recommendations can be proposed for wind standards and codes of practice, particularly for the ASCE 7-05 (the design wind pressure on the components and claddings of parapets):

- Wall pressure coefficients can be used as a good estimate for those on the exterior parapet surface.
- Pressure coefficients on the corner of the interior parapet surface can be reduced from + 3.8 and – 2.4 for windward and leeward parapets, respectively, to + 2.4 and – 2.0.
- Pressure coefficients on the mid-span of the interior parapet surface can be from + 2.8 and – 2.2 for windward and leeward parapets, respectively, to + 2.0 and – 1.8.

**Table 5.1: Characteristics of different models used in each study**

Study	$L/H$	$h_p/H$	$x/L$	$\zeta/h_p$
Present study	1.2	0.16	0.04	0.50
Stathopoulos et al, 2002-a	1.0	0.13	0.08	0.45
Stathopoulos et al, 2002-b	3.4	0.10	0.08	0.45
Mans et al, 2005	3.0	0.10	0.06	0.83

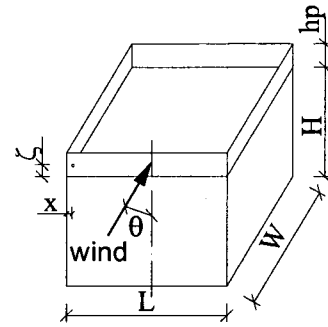
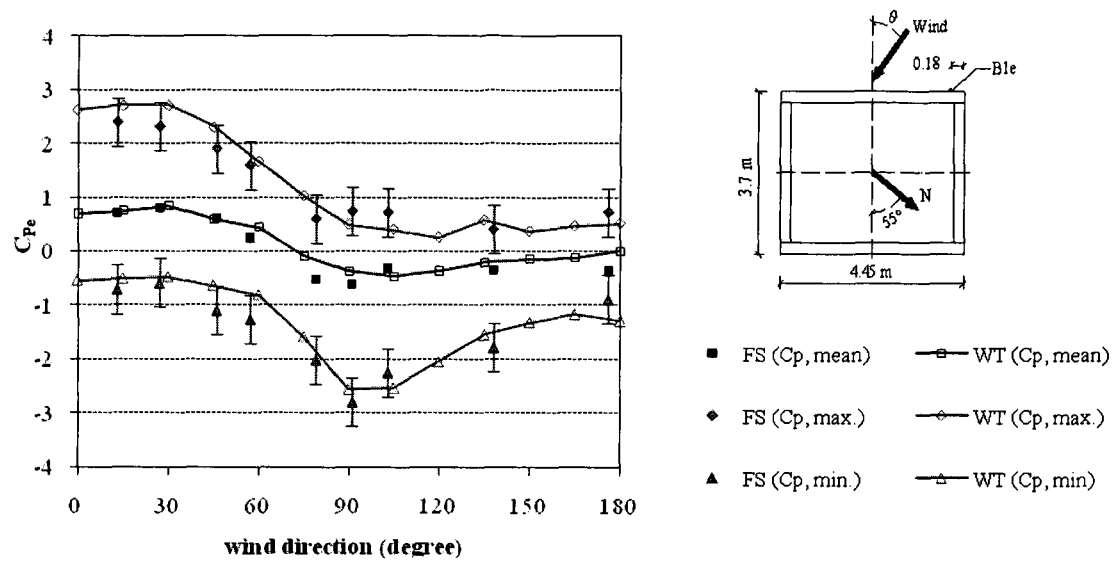


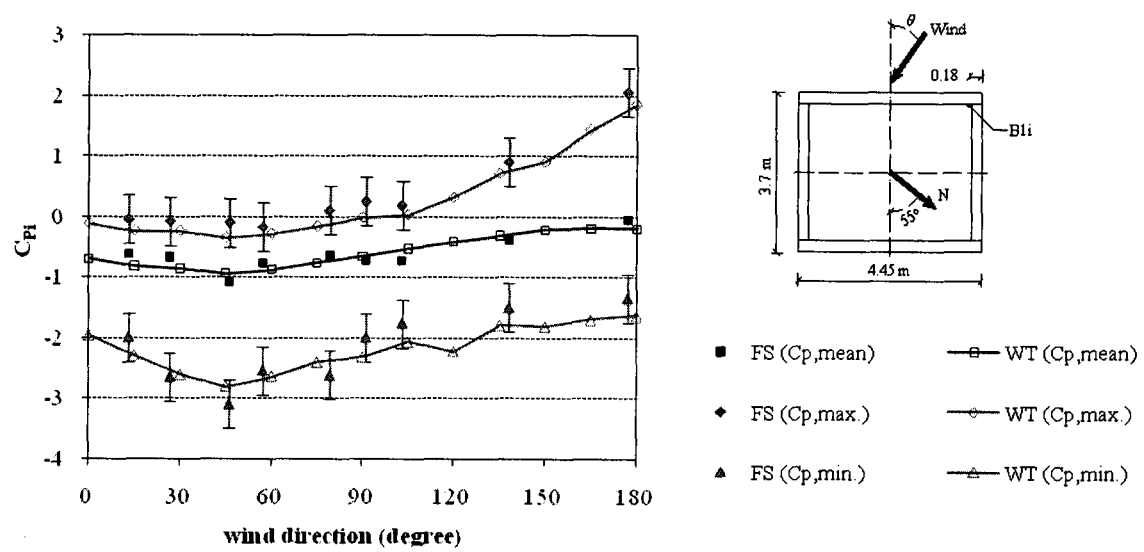
**Table 5.2: Comparison of parapet load coefficients derived from NBCC (2005) with the current measured values**

<b>Study</b>		<b>Corner</b>	<b>Mid-span</b>
$(C_p C_g)_{wall}$ (NBCC, 2005)		1.8	1.8
$(C_p C_g)_{roof}$ (NBCC, 2005)		- 5.4	- 2.5
$(C_F)_{parapet}$ (NBCC, 2005)		7.2	4.3
$(C_F)_{parapet}$ (present study)	FS	3.72	2.88
	WT	3.68	3.36

Note: these values represent the largest peak values from all wind directions

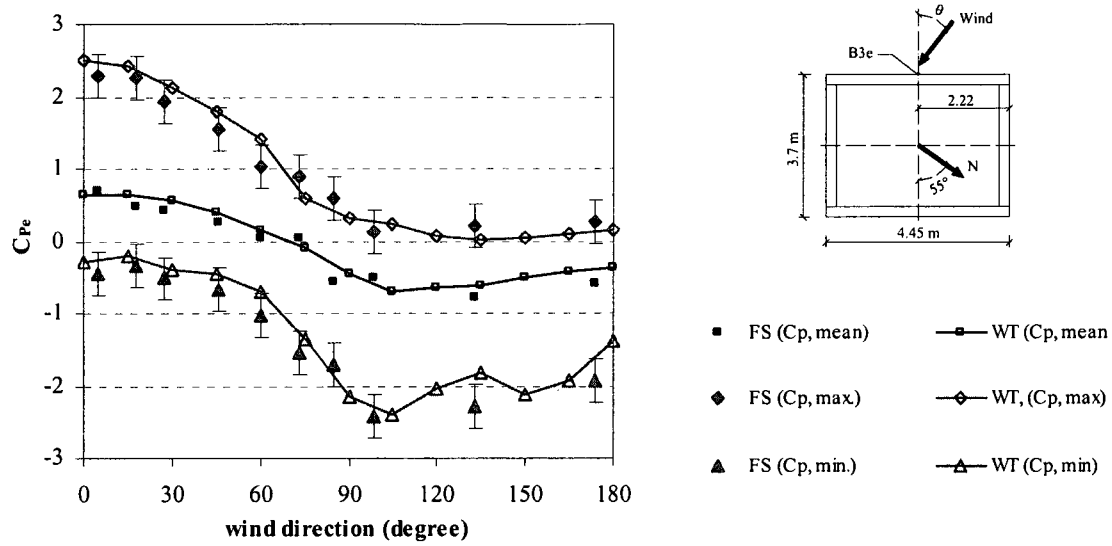


(a) Exterior surface parapet pressure coefficients

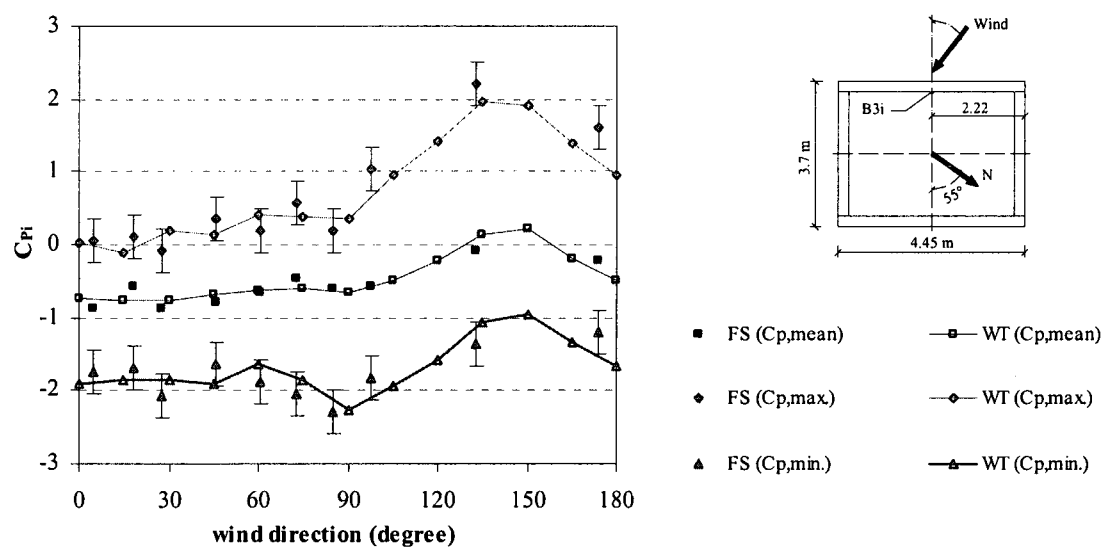


(b) Interior surface parapet pressure coefficients

Figure 5.1: Surface parapet pressure coefficients recorded near the corner (Tap B1)

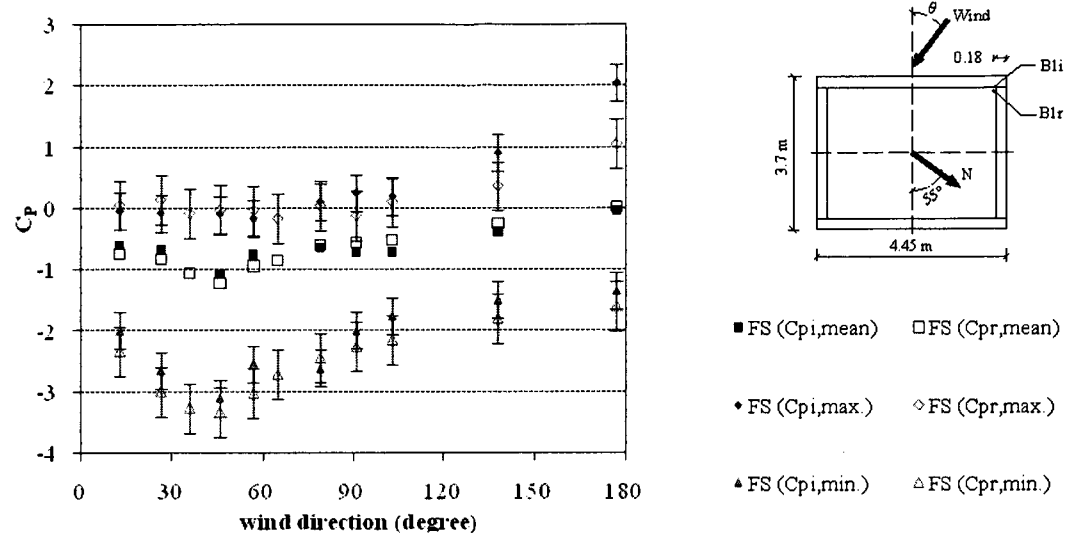


(a) Exterior surface parapet pressure coefficients

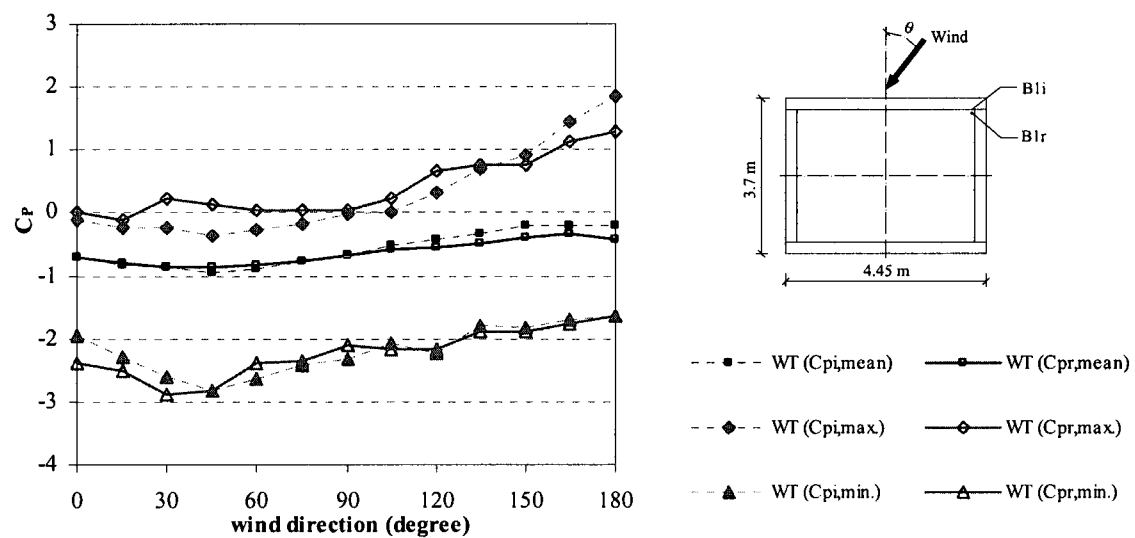


(b) Interior surface parapet pressure coefficients

Figure 5.2: Surface parapet pressure coefficients recorded at the mid-span (Tap B3)

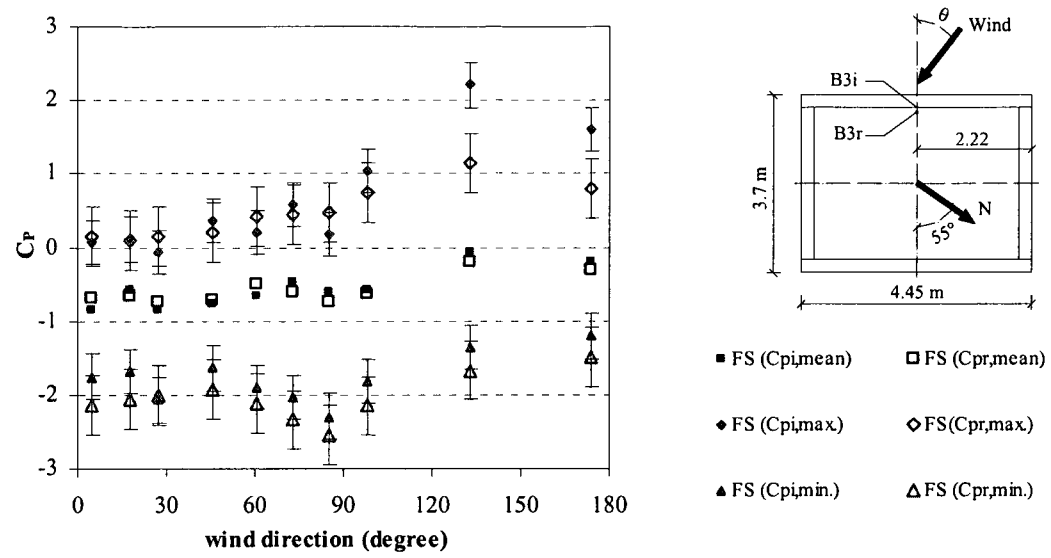


(a) Full-scale

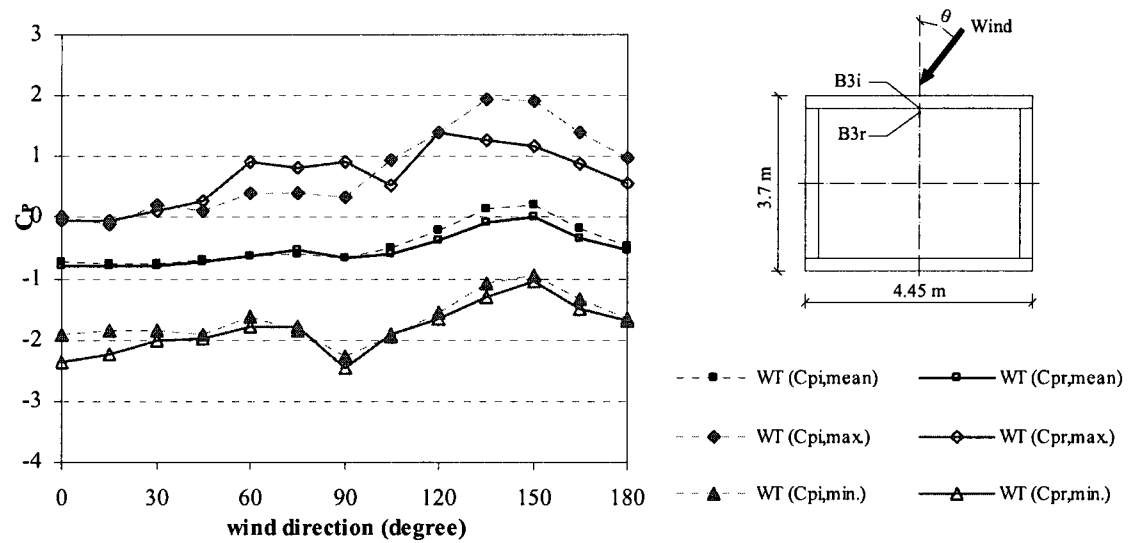


(b) Wind tunnel

**Figure 5.3: Comparison of peak pressure coefficients on the roof and the inside surface of the parapet near the corner (Tap  $B1$ )**



(a) Full-scale



(b) Wind tunnel

Figure 5.4: Comparison of peak pressure coefficients on the roof and the inside surface of the parapet at mid-span (Tap B3)

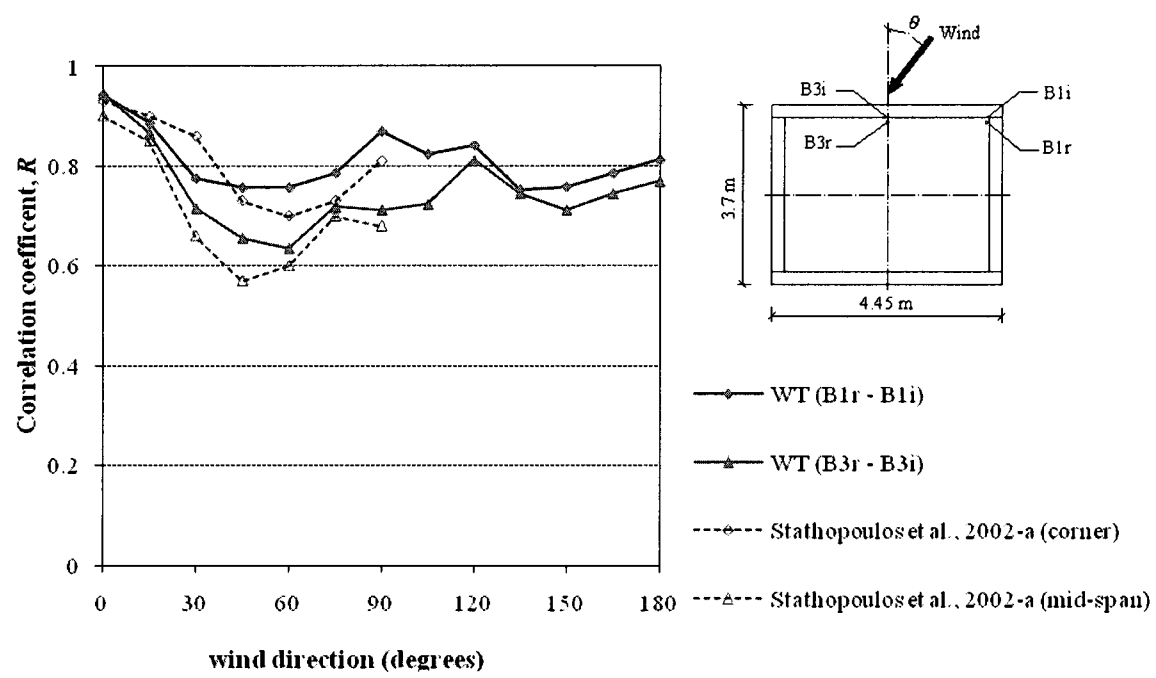
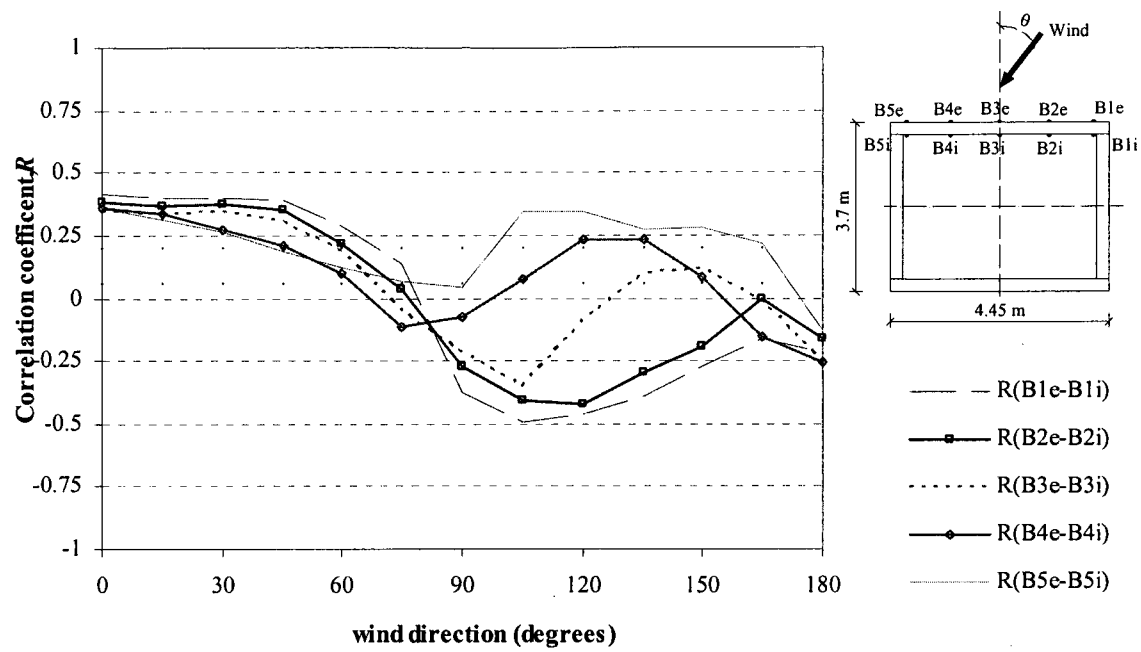
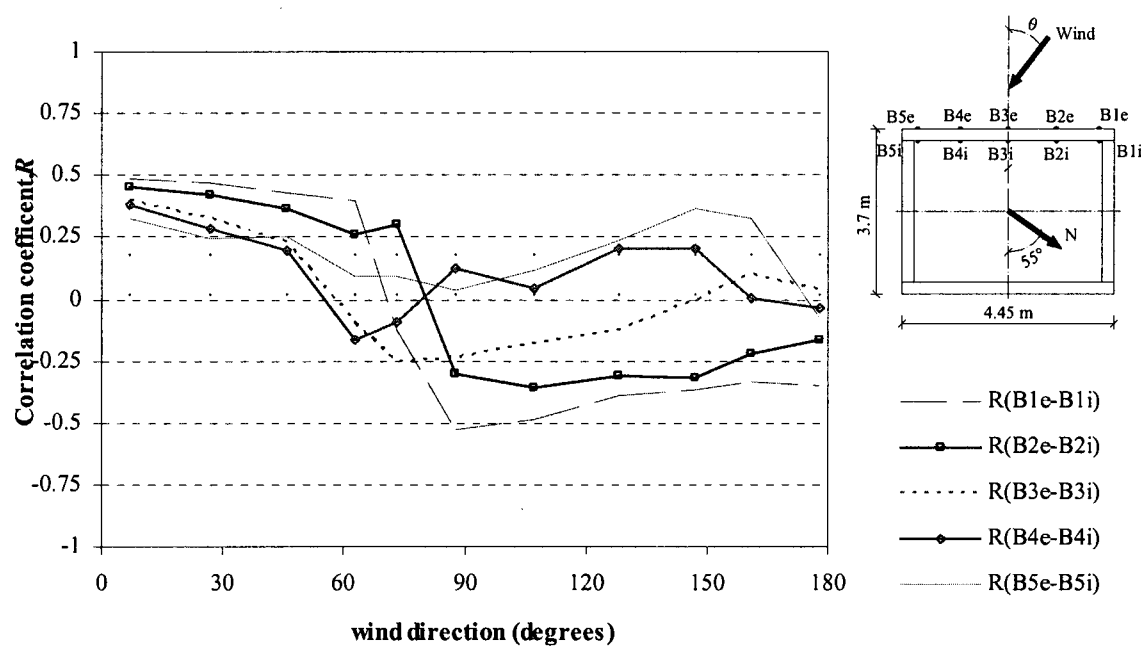


Figure 5.5: Effect of wind direction on the correlation coefficients of  $C_{Pr}$  and  $C_{Pr}$

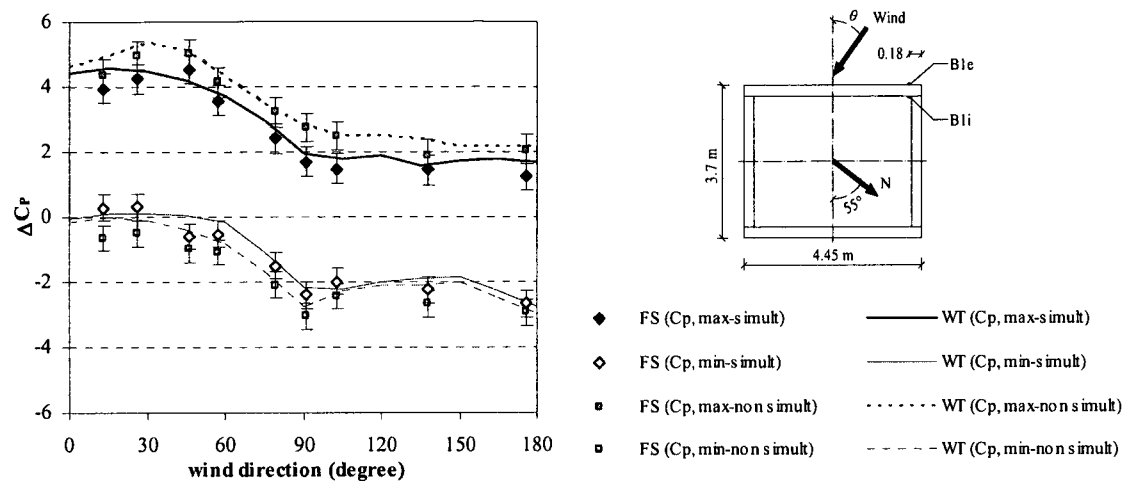


(a) Wind tunnel data

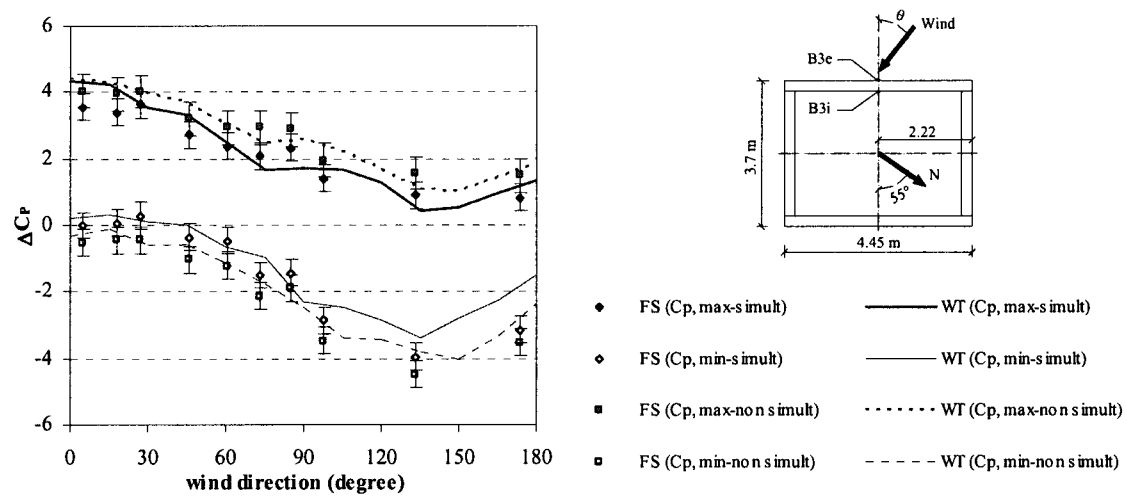


(b) Full-scale data

Figure 5.6: Effect of wind direction on the correlation coefficients of  $C_{Pe}$  and  $C_{Pi}$



(a) Pressure coefficients at the corner (Tap B1)



(b) Pressure coefficients at mid-span (Tap B3)

Figure 5.7: Peak local load coefficients on the parapet measured

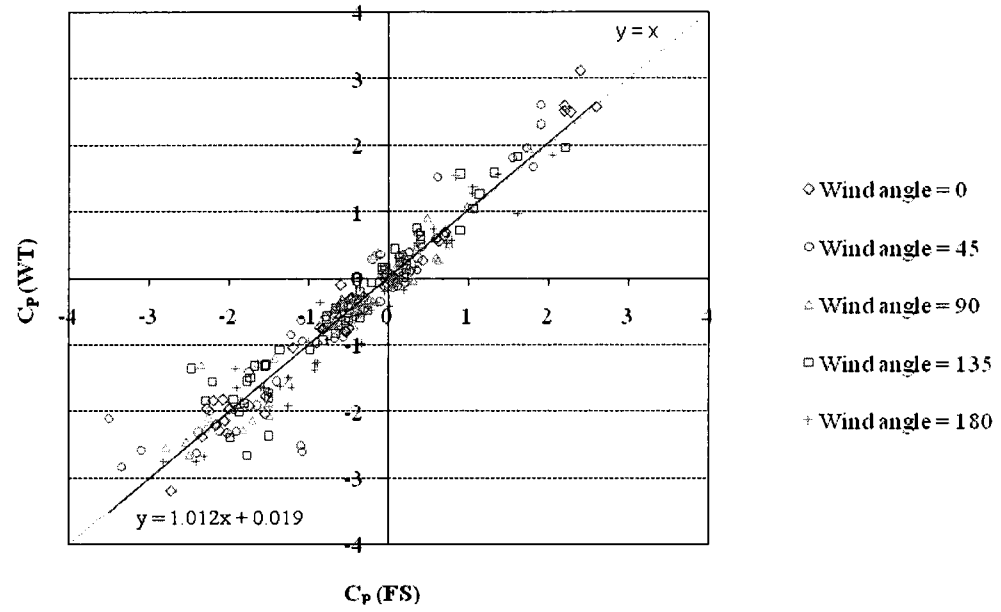
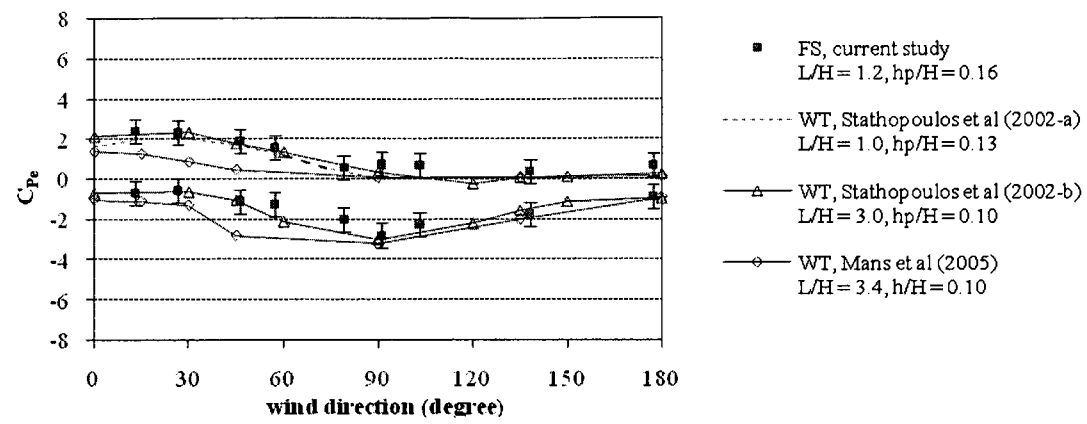
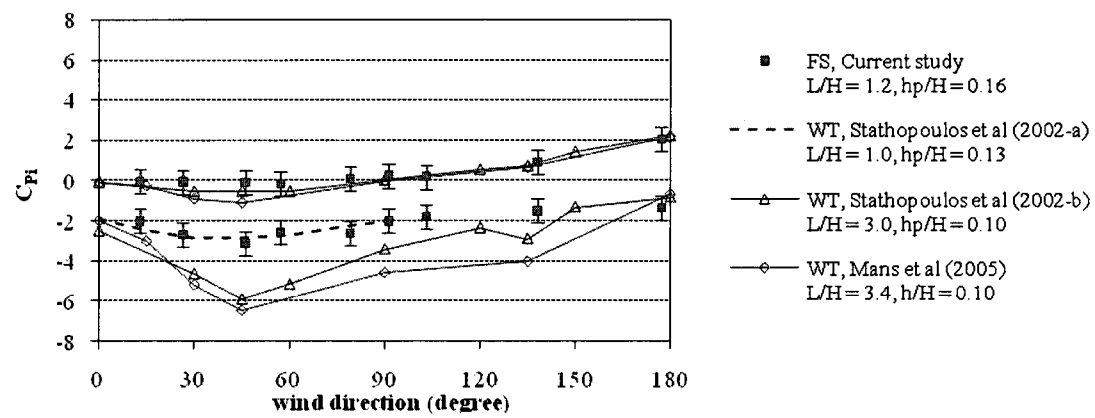


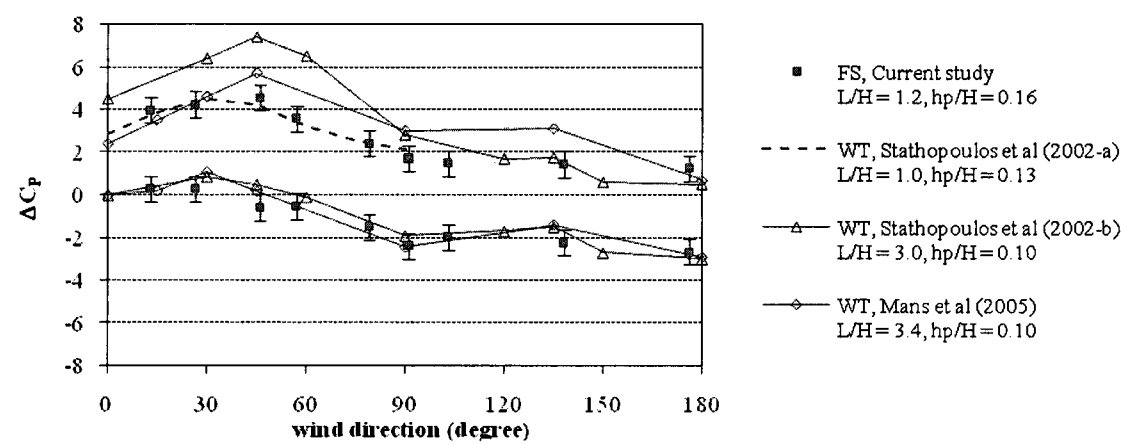
**Figure 5.8: Comparison between pressure coefficients measured in full-scale and wind tunnel**



(a) Exterior surface parapet pressure coefficients

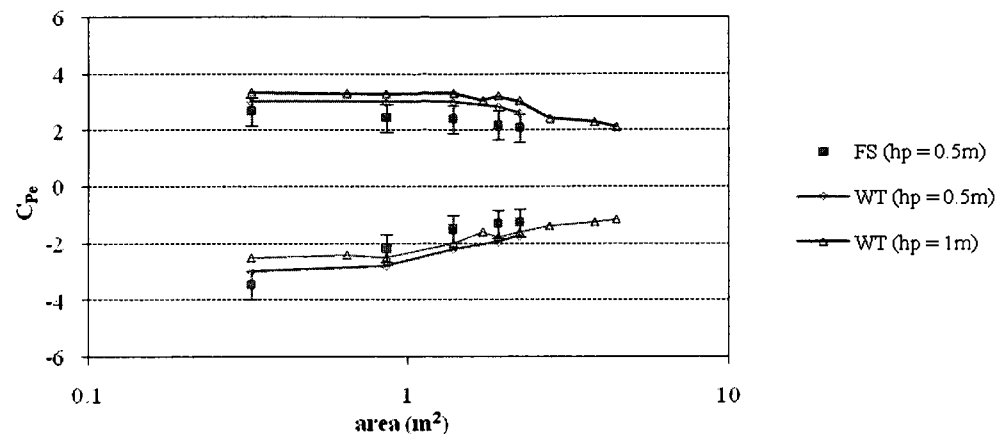


(b) Interior surface parapet pressure coefficients

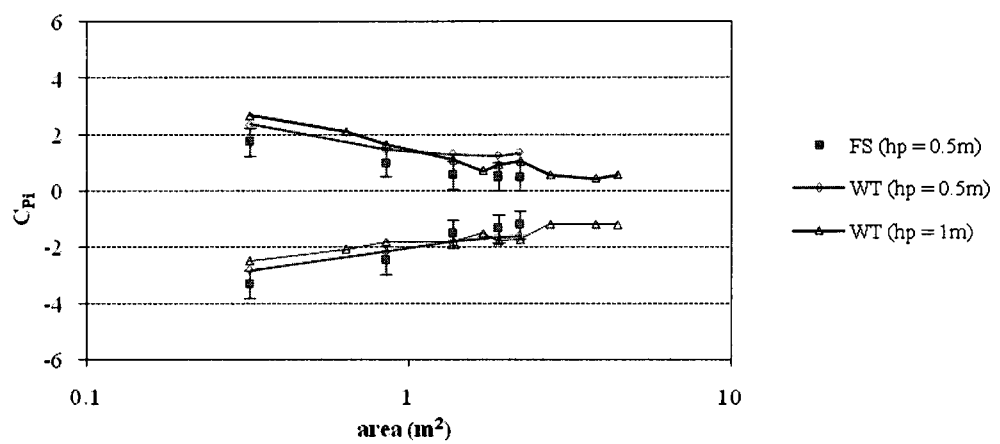


(c) Simultaneous combined pressure coefficients from both surfaces

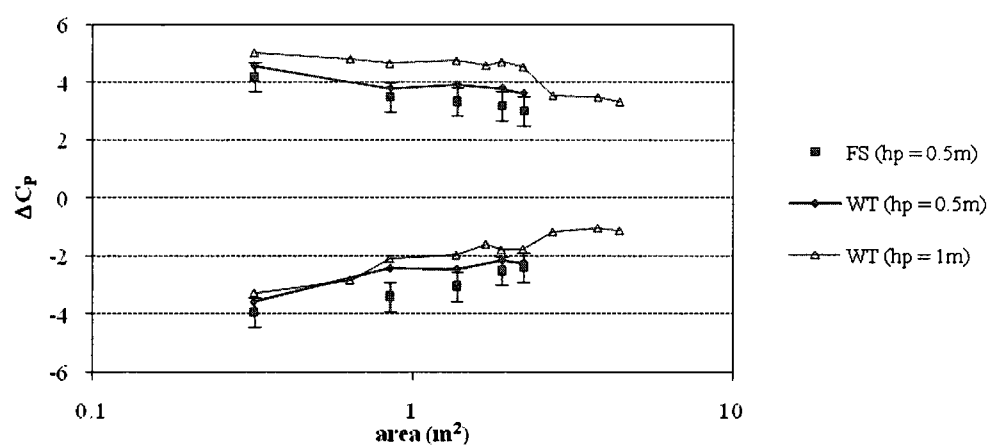
Figure 5.9: Comparison of peak pressure coefficients from different studies



(a) Exterior parapet loading coefficients

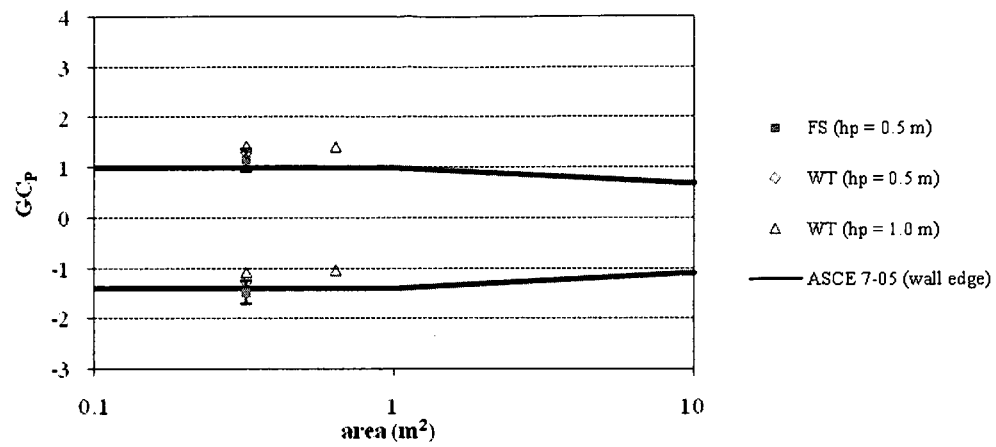


(b) Interior parapet loading coefficients

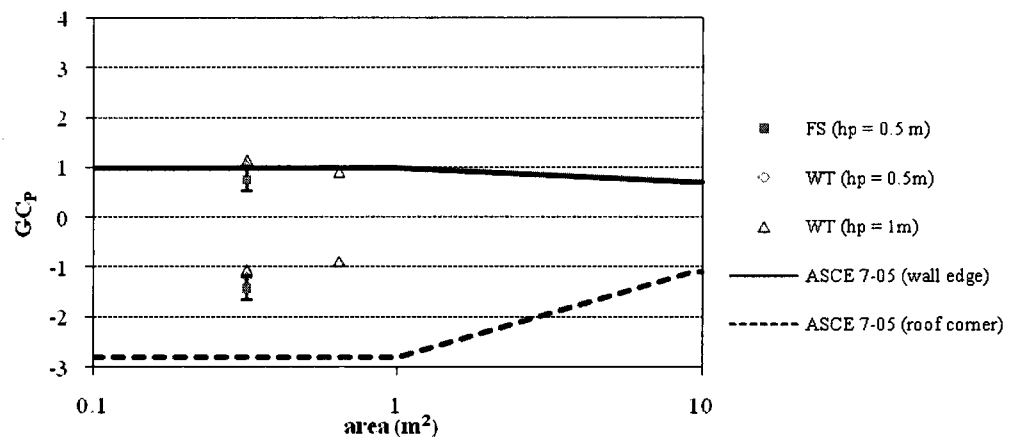


(c) Net loading from both surfaces

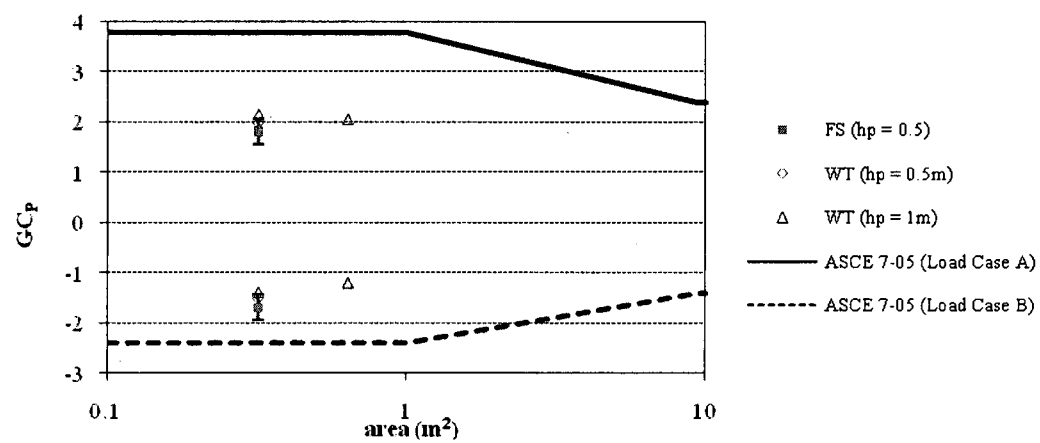
Figure 5.10: Variation of peak loading coefficients (obtained from the most critical azimuth) with different tributary areas



(a) Exterior parapet loading coefficients

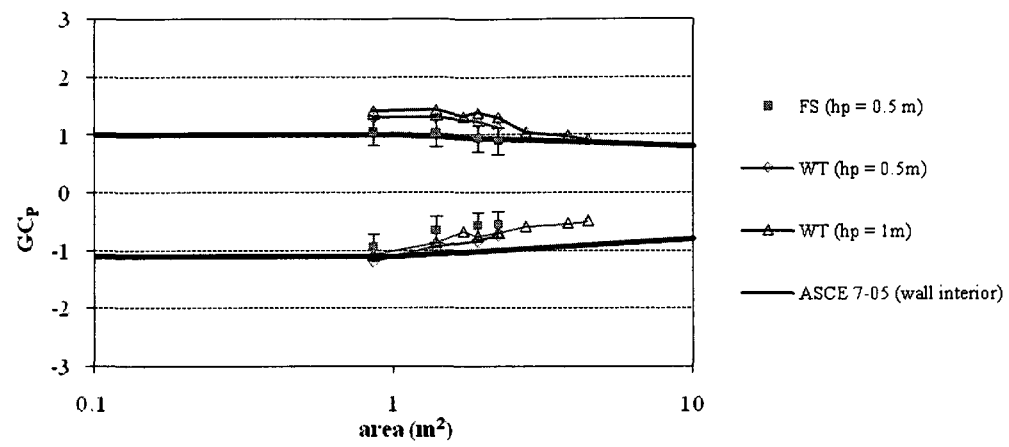


(b) Interior parapet loading coefficients

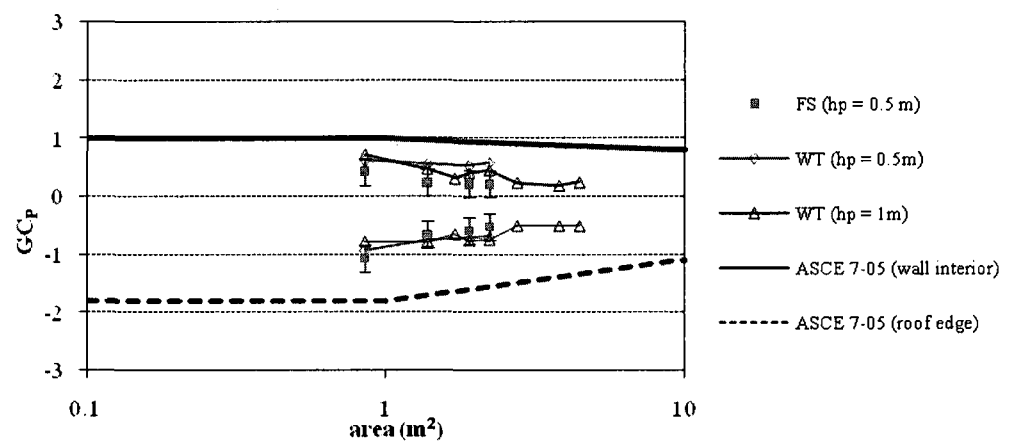


(c) Net loading from both surfaces

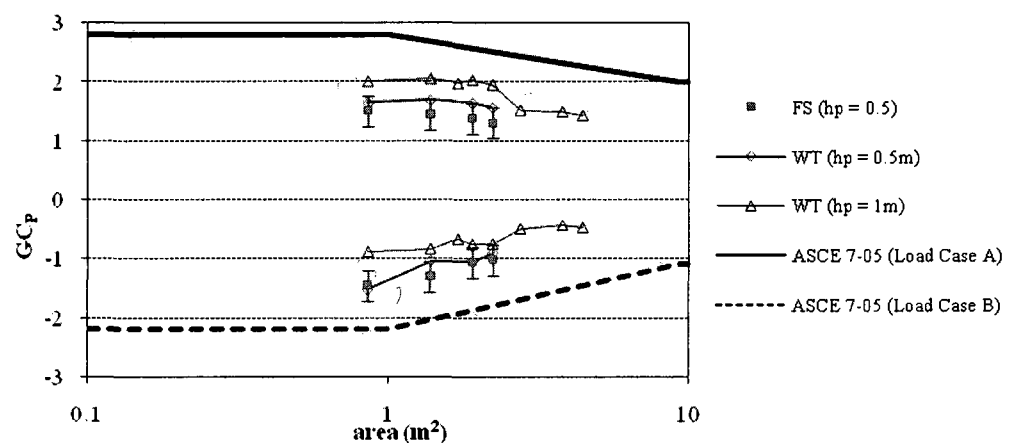
Figure 5.11: Comparison of edge region loading coefficients with ASCE 7-05



(a) Exterior parapet loading coefficients



(b) Interior parapet loading coefficients



(c) Net loading from both surfaces

Figure 5.12: Comparison of interior region loading coefficients with ASCE 7-05

## *Chapter Six*

### **NUMERICAL RESULTS AND DISCUSSION**

Numerical simulation of wind flow over the test building model with parapets is performed with the commercial CFD code Fluent 6.1.22. Simulation details were explained in Chapter three. This chapter presents an analysis and comparisons of numerical outcomes. The computation has been conducted for wind flow perpendicular on the building face (i.e. zero wind azimuth). Only mean wind-induced pressures on the roof and on parapet surfaces are computed, since peak pressures are not predicted reliably by current computational approaches. Two different turbulence models, namely: RNG and RLZ  $k-\varepsilon$  are used. The computational results are compared with the present experimental results as well as with those from previous numerical studies. Note that, all pressure data are presented in the form of pressure coefficients, normalized by using the dynamic pressure at roof height.

#### **6.1 Flow Patterns around the Building**

The wind flow conditions around the building with parapet have been numerically simulated using RNG  $k-\varepsilon$  model. Data is presented for the building with 0.01 m parapet height which corresponds to a full-scale parapet height of 0.5 m. The mean velocity vector fields in cross-section through the center of the building are presented in Figure

6.1. The reversed flows in front of the building near the ground, the upstream standing vortices (Figure 6.1-a); and the circulation flow region behind the building (the near wake recirculation region) are fully predicted (Figure 6.1-b). Very small arrows indicate very low mean velocity, which is the characteristic of the flow in such regions. Mean stream lines in the approach flow are coming closer together toward the top edge of the windward parapet and very high velocity at this edge is clearly shown (Figure 6.1-c). The presence of the parapet makes the separated flow to be raised from the roof edge and a separation region is formed behind the windward parapet. Smaller vectors in this region indicate lower velocity and hence lower pressure, comparing with the case of no parapet where the flow separates at the roof edge. Flow reattachment does not occur on the roof surface, as expected for buildings with reduced length/width ratio. Therefore, the bulk of the wind flow passes above the parapet height with a small amount of recirculation above the roof. This significantly changes the flow dynamics over the building by reducing the pressure coefficients on the roof surface. The separated flow over the leeward parapet edge continues circulating and merged with the near wake recirculation flow. The wind conditions around a plan view, at roof height, are presented in Figure 6.2. The separation regions, found in the experiments by Murakami, 1990, beside the side walls have been successfully predicted. Also, the recirculation behind the building is clearly shown.

## **6.2 Mean Pressure Distribution on the Roof**

In order to monitor the general distribution of wind pressures on the building roof without parapet, the current numerically predicted pressures in the form of pressure coefficient

contour-lines are presented in Figure 6.3-a and compared with some previous numerical and experimental results. The agreement between the current study and the numerical results of Zhou (1995), for the two-layer method, is reasonable (Figure 6.3-b), considering the differences in building geometries. Furthermore, the current study agrees with the experimental results of Hunt, 1982, (Figure 6.3-c).

Figure 6.4-a shows the results of the roof with 0.01 m parapet. It can be clearly seen that the high negative pressures (suctions) near the windward edge have been reduced by adding the parapet, which has been experimentally verified by many previous studies (Kind, 1988; Baskaran and Stathopoulos, 1988-a). In addition, the presence of parapet, also, acts to modify the pressure distribution on the roof to be more uniform, as indicated by Kareem and Lu (1992). Figure 6.4-b shows the current wind tunnel experimental results for building roof with 0.01 m parapet. Numerical results show good performance compared to those from the wind tunnel.

The computed pressure coefficients along the center line of the roof, for both RNG and RLZ k- $\epsilon$  models, are compared with the wind tunnel experimental results (Figure 6.5). The results of the building with two different parapet heights:  $h_p = 0.01$  m (Figure 6.5-a) and  $h_p = 0.02$  m (Figure 6.5-b), are presented. RLZ k- $\epsilon$  model shows significant discrepancy in the pressure coefficients comparing with the measured data. In contrast, the general agreement between numerical results of RNG k- $\epsilon$  model and experimental data is reasonable. However, the locations of maximum mean pressure coefficient along the building centerline are different. The numerical maximum pressure coefficient occurs

at a distance of  $x/L$  of 0.25 for lower parapet and of 0.35 for higher parapet. On the contrary, the experimental maximum pressure coefficient occurred closer to the roof edge,  $x/L$  of 0.15 for both parapet heights.

### **6.3 Effect of parapet height on roof pressures**

In an attempt to examine the effect of parapet height on roof pressures, the negative pressure coefficients at a point near the leading edge along the center line of the roof are plotted for different parapet heights (Figure 6.6). Numerical results are compared with the wind tunnel experimental data of Stathopoulos et al. (2002-b). The model for that study was a cube of 30 m long and has been tested for different parapet heights. Therefore, the ratio of parapet height to the building height ( $h_p/H$ ) has been used for comparison. As shown, the computed pressure values for low parapet height ( $h_p/H = 0.03$ ) tend to show higher suction near the windward edge of the roof, comparing with the case of no parapet. Increasing parapet height ( $h_p/H = 0.67, 0.13$  and  $0.2$ ) causes an evident reduction in the negative pressures near the windward edge of the roof, which had been concluded previously in many experimental studies (Bienkiewicz and Sun, 1992; Baskaran and Stathopoulos, 1988-a).

### **6.4 Mean pressures on the parapet itself**

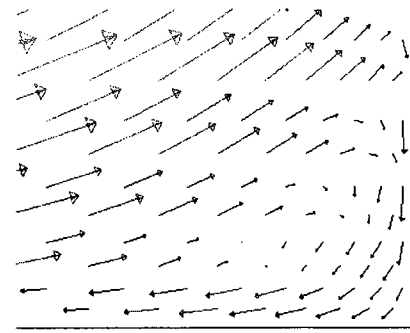
In an attempt to study the wind-induced pressures on parapets themselves the pressure coefficients on the exterior and interior parapet surfaces, along a vertical line at centerline

of the parapet, are presented in Figure 6.7-a. The computational results on the exterior surface are compared with wind tunnel data as well as those from Stathopoulos et al. (2002-b), at the same locations. Numerical and experimental data shows that exterior mean pressures reach their maximum values at the base of the parapet and gradually reduce with parapet height. With regard to the interior pressures, numerical computed coefficients seem to reach their maximum values within the mid-height of the parapet. The total pressure coefficients resulting from combined both surface coefficients are shown in Figure 6.7-b and are compared with the wind tunnel data. Generally, good agreement between the numerical and wind tunnel measurements can be shown.

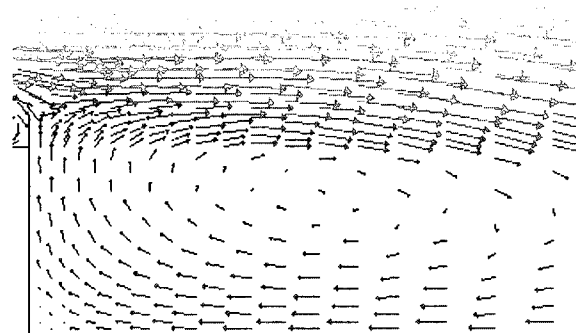
Table 6.1 compares the mean pressure coefficients on the roof ( $C_{pr}$ ) and on the inside surface of the wind-ward parapet ( $C_{pi}$ ). The full-scale parapet height is 1 m. Data were obtained at the corner region and at the mid-span location.  $C_p$  values are presented at points very close to the roof edge ( $x/l = 0.05$ ). The computed values of  $C_{pr}$  and  $C_{pi}$  at the mid-span location are approximately the same. On the other hand, at the corner region  $C_{pr}$  is approximately 10% larger than  $C_{pi}$ . The comparison with the wind tunnel experimental results, at the same points, shows that the numerical predictions fall on the lower side, except for the corner roof pressures.

**Table 6.1: Numerical and Experimental pressure coefficients**

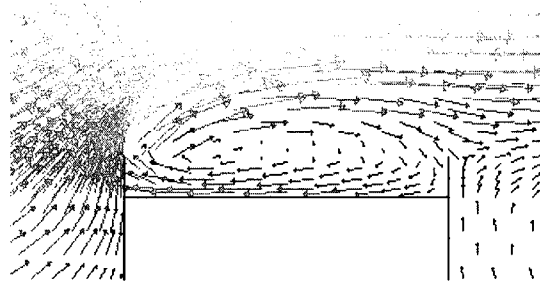
<b>Test type</b>	<b>Corner region</b>		<b>Edge mid-span</b>	
	$C_{pr}$	$C_{pi}$	$C_{pr}$	$C_{pi}$
Numerical	-1.01	-0.80	-0.91	-0.76
Experimental	-0.73	-0.71	-0.69	-0.68



(a) Upstream standing vortex



(b) Near wake recirculation



(c) Separation region

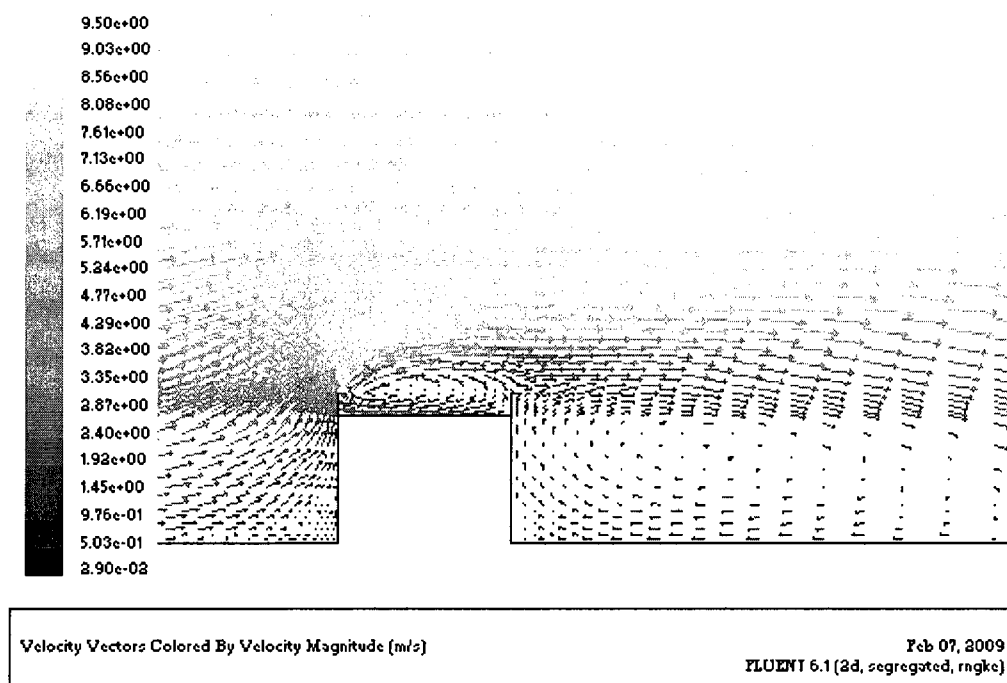
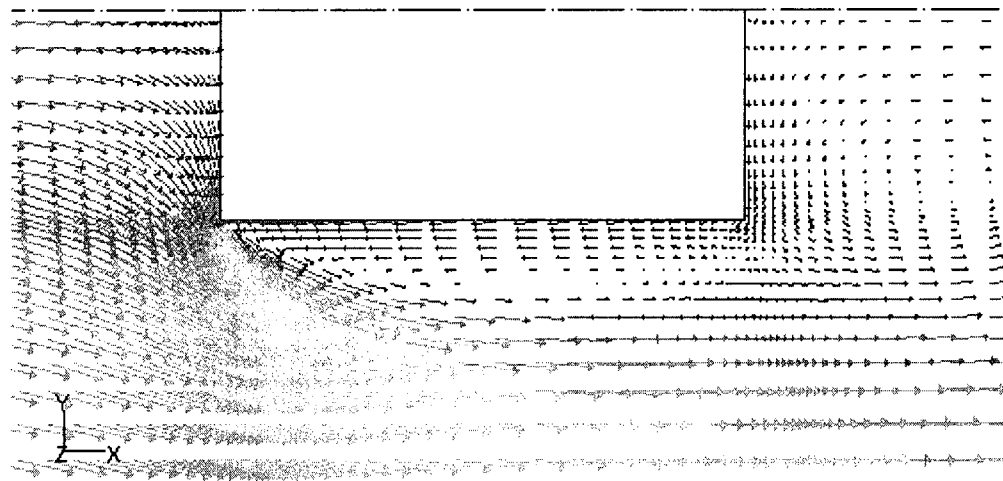
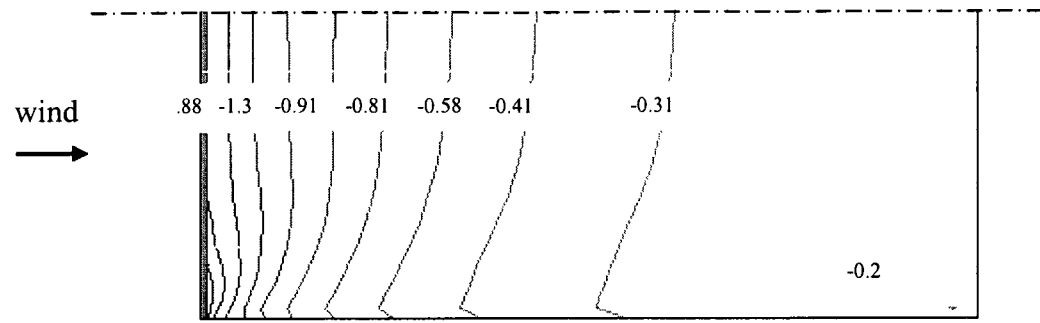


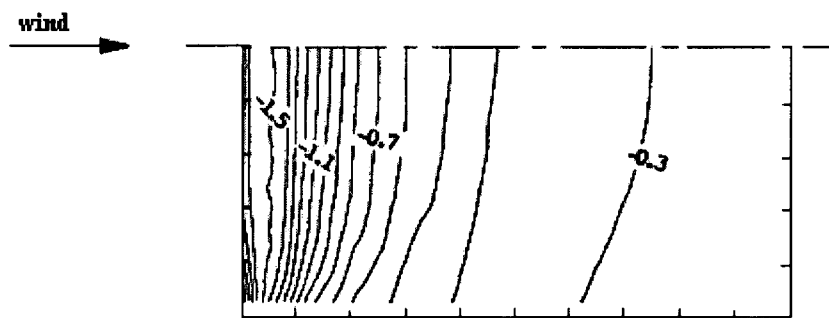
Figure 6.1: Mean velocity vector field around the building with 0.01 m parapet  
(Vertical cross-section)



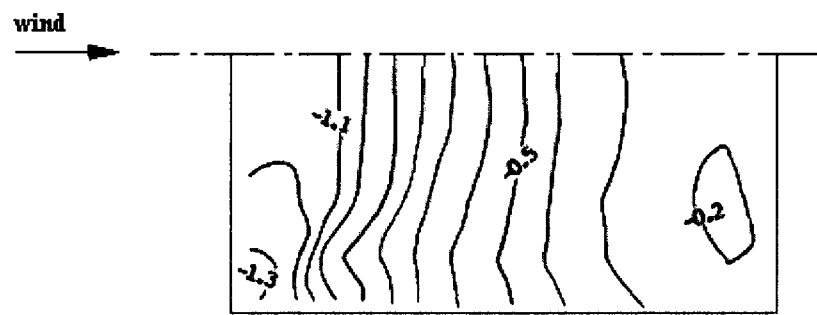
**Figure 6.2: Mean velocity vector field around the building (Plan-view)**



(a) RNG  $k-\epsilon$ , (present study)

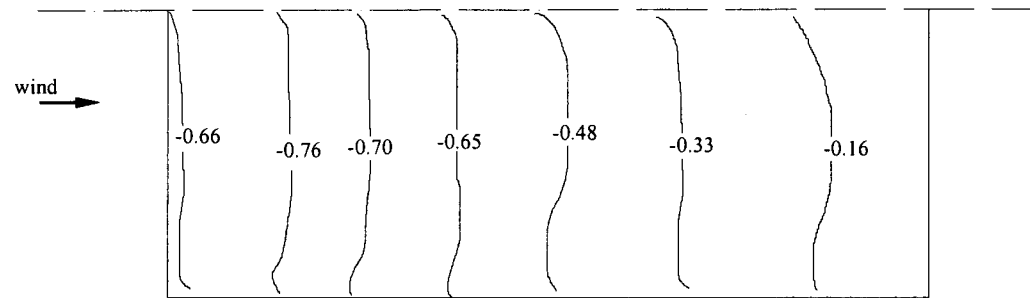


(a) N-R two layer method (Zhou, 1995)

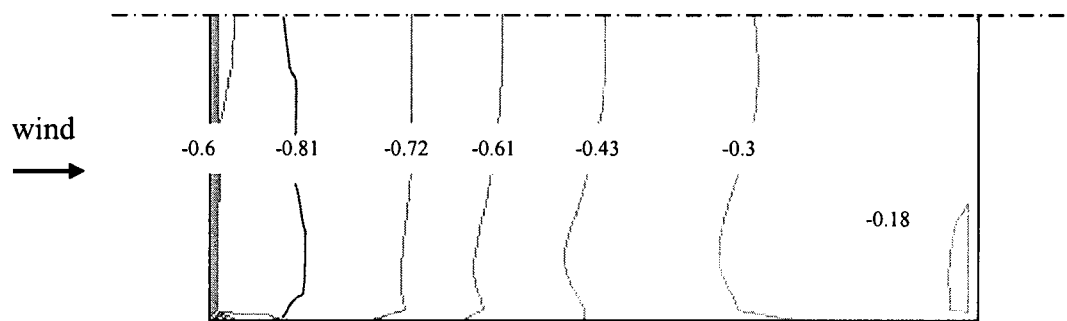


(b) Experimental (Hunt, 1982)

Figure 6.3: Contours of pressure coefficient on roof surface from different studies  
( $h_p = 0$  m)

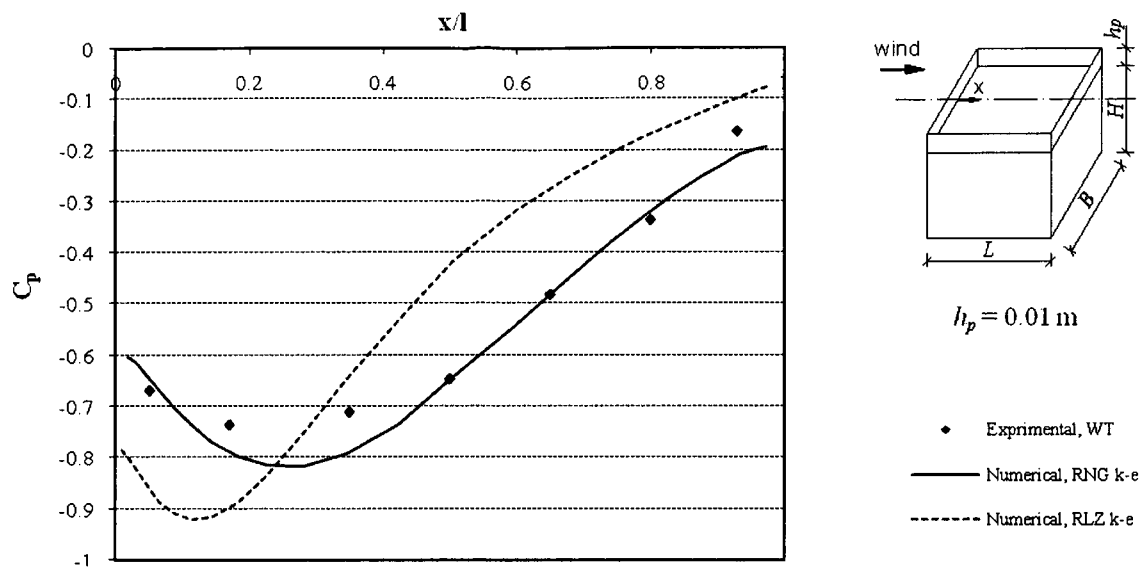


(a) Wind tunnel,  $h_p = 0.01$  m

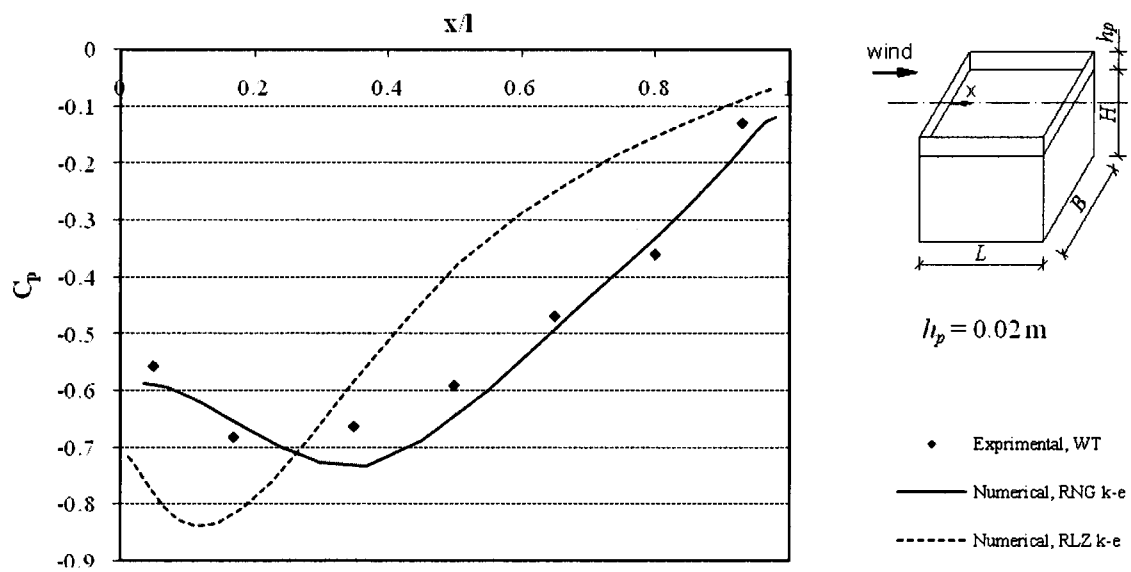


(b) RNG  $k-\epsilon$ ,  $h_p = 0.01$  m

Figure 6.4: Contours of pressure coefficients on roof surface (current study)



(a)  $h_p = 0.01$  m



(b)  $h_p = 0.02$  m

Figure 6.5: Pressure coefficient along the center line of building roof

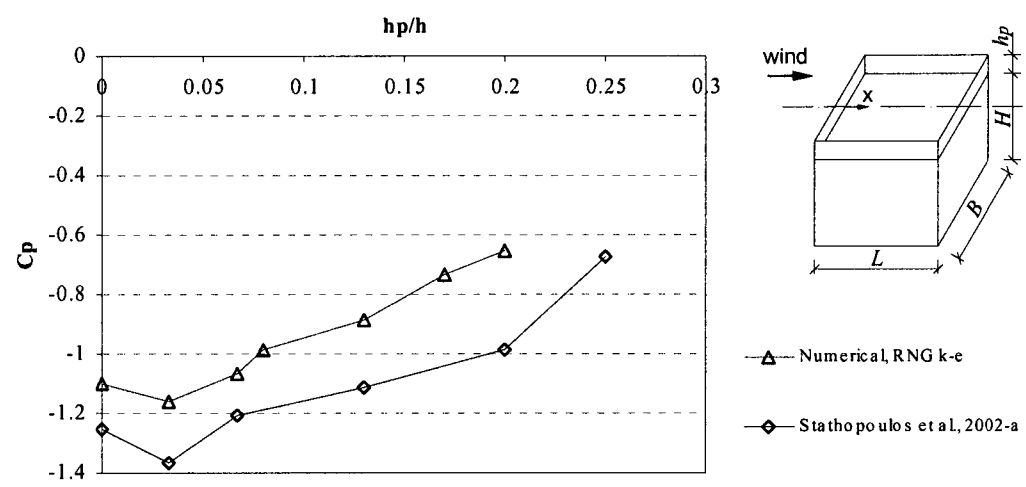
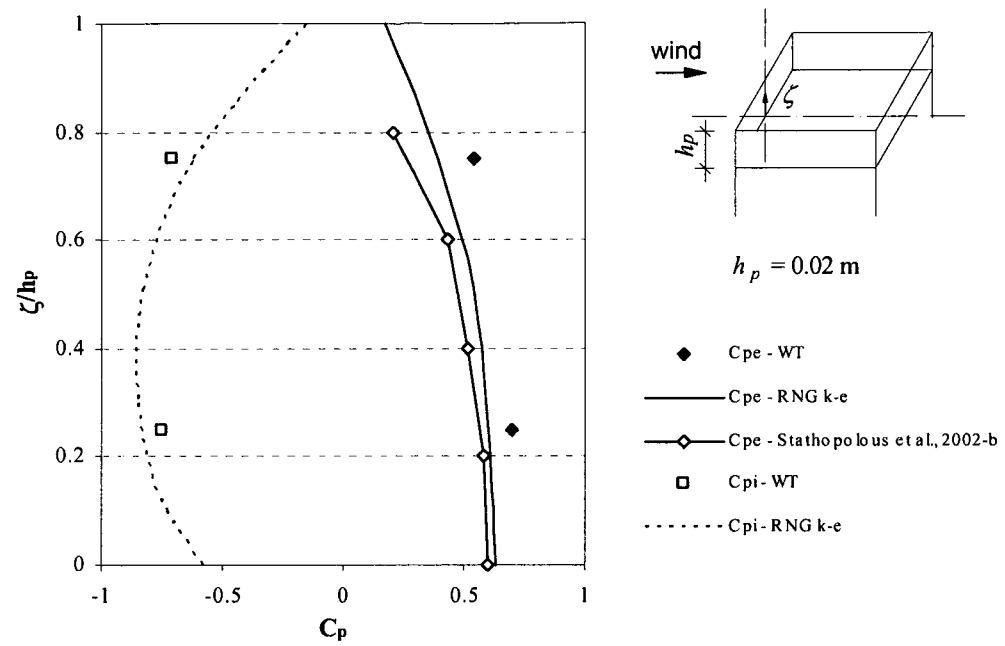
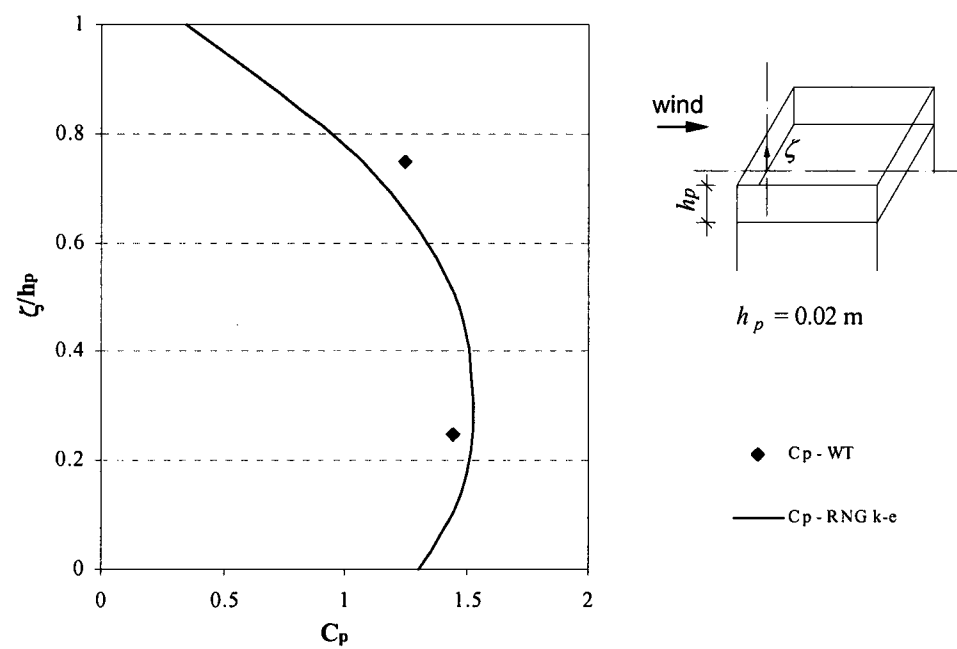


**Figure 6.6: Effect of parapet height on roof pressure**



(a) Individual mean pressure coefficients



(b) Combined mean pressure coefficients

Figure 6.7: Change of parapet surface pressure with parapet height

## *Chapter Seven*

### **CONCLUSIONS, RECOMMENDATIONS AND FUTURE WORK**

In the past, only a limited number of studies were attempted to directly measure parapet surface pressures in the wind tunnel, due to modeling limitations. However, no full-scale study was reported. Consequently, wind loading standards and codes of practice provide very little guidance regarding the design wind loads of parapets. Recently, the ASCE-7 (2005) considered the importance of defining parapet loads. However, due to insufficient research, the proposed recommendations are based on a rational technique rather than on experimental investigations. The present study has attempted to reduce this lack of information regarding parapet design loads based on comprehensive experimental and numerical investigations.

#### **7.1 Summary**

In wind engineering research, it is extremely important to carry out field measurements for wind flow on real buildings. Full-scale testing is suitable to obtain reliable wind-measured data and to understand the flow mechanism around buildings. Consequently, this type of testing is the only reliable method to validate wind tunnel results as well as to verify and develop numerical simulations. Comprehensive field measurements of parapet surface pressures have been completed using a small low-rise building located in an open

area. A perimeter parapet of a height of 0.5 m is attached to the building roof and is drilled for tapping on all parapet surfaces. Mean and simultaneous peak pressures, on the exterior and interior parapet surfaces as well as the roof edge, were recorded.

The experimental building is modeled to be tested in the BLWT of Concordia University. Based on the importance of correctly modeling the turbulence intensity at the roof height, a geometric model scale of 1:50 is used. Two sets of perimeter parapets: 0.01 and 0.02 m, equivalent to 0.5 and 1 m height in full-scale respectively, have been attached to the building model roof. Both local and area-average pressure coefficients are recorded on the exterior and the interior parapet surfaces.

Accurate computer predictions are very useful since this method is less expensive and time consuming than comparable field or wind tunnel testing. Numerical simulation of wind flow over the building model with the parapet was performed with the commercial CFD code Fluent 6.1.22. The steady-state RANS equations were solved using two different modified  $k-\varepsilon$  turbulence models: the RNG  $k-\varepsilon$  model and the RLZ  $k-\varepsilon$  model. The computations were performed for flow perpendicular to the building face ( $\theta = 0^\circ$ ). The experimental building with different parapet heights was simulated in order to examine the effect of parapet on roof pressures. Considering the current state-of-the-art peak pressures are not predicted reliably by computational approaches. Therefore, in the present study only mean wind-induced pressures on the roof and on parapet surfaces were computed and compared with the current experimental results as well as with previous numerical studies.

## 7.2 Concluding Remarks

The wind tunnel results have been systematically compared with the full-scale collected data through the evaluation of the descriptive parameters of parapet surface pressures. Generally, the comparisons reveal reasonable agreement between the two different techniques, confirming successful wind tunnel simulation. Mean pressure coefficients measured in the wind tunnel show very good agreement with the full-scale results. However, the analyses demonstrate some differences in the maximum peak pressure coefficients particularly for critical wind directions, where the highest pressures usually recorded. These differences are largely attributed to the unsteadiness of the direction of natural wind. Moreover, locations and density of the pressure taps on the model may be considered the most important parameter in affecting the experimental results. Specific conclusions regarding the measurements of local parapet surface pressures can be illustrated as follows:

- For exterior parapet surface, the maximum positive peak pressure coefficients occur for winds approaching perpendicular to the parapet face, while the maximum negative peak pressure coefficients occur for winds approaching parallel to the parapet section.
- For interior parapet surface, the maximum negative peak pressure coefficients occur at the leading corner for wind angle near  $45^\circ$ . On the other hand, the

maximum positive peak pressure coefficients occur for winds perpendicular to the interior parapet surface ( $\theta = 180^\circ$ ).

- The maximum negative peak pressure coefficients measured on the roof edge are approximately 15 % and 10 % higher than those on the interior parapet surface, for corner and mid-span locations, respectively.
- Peak drag coefficients, which include the combination of pressures from both parapet surfaces, were found to occur during cornering winds. Negative pressure coefficients on the interior parapet surface are found to dominate the net loading on the parapet. However, the positive pressures on the exterior surface make an important contribution.
- The local inward and outward loads on the parapet measured near the leading corner were approximately 25% and 30%, respectively, higher than those at the mid-span. Simultaneous pressures are found to be lower than non-simultaneous pressures.
- The correlation between roof edge and interior parapet surface pressures depend on the wind direction. High correlation obtained for  $\theta = 0^\circ$ , while, for oblique wind directions ( $30^\circ - 60^\circ$ ) lowest correlation was found. This indicates that roof edge pressures may not be an adequate estimation for the interior parapet surface pressures, in the absence of experiments.

- The overall correlation between the pressures on the exterior and the interior parapet surfaces is considerably low, which indicates that the absolute maximum peak pressures do not occur simultaneously on both surfaces. Therefore, the total load coefficients on a parapet may only be obtained by simultaneously combined the pressure coefficients on both surfaces. The correlation between the exterior and interior parapet surface pressures, measured in the wind tunnel, shows reasonable agreement with the respective full-scale correlation.
  
- The parapet design loads obtained by combining the NBCC (2005) design load coefficients for windward wall and roof were significantly higher than actual loads on the parapet.

Area averaged pressure coefficients show that the net loads on the 1 m height parapet are higher than those on the 0.5 m height parapet by about 15 %. The area-averaged loads on the exterior and the interior surfaces of the parapet, in addition to their simultaneous combination, were compared with the ASCE 7-05 provisions. Specific conclusions are listed as follows:

- For the exterior parapet surface:  
 The ‘wall edge zone’ coefficient suggested by the standard underestimates the surface pressure coefficients on parapet edge up to 20 %.  
 The negative ‘wall interior zone’ coefficient overestimates the negative surface pressure coefficients on parapet mid-span by 10 – 35%. While the positive ‘wall

interior zone' coefficient underestimates the negative surface pressure coefficients on parapet mid-span by 10 – 30%.

- For the interior parapet surface:

The 'roof corner zone' coefficient overestimates the negative surface pressure coefficients on parapet edge by about 40 %.

The 'roof edge zone' coefficient overestimates the surface pressure coefficients on parapet interior locations by 25 - 35 %.

- For combined action from both surfaces:

The coefficient for the Load Case A overestimates the net positive pressure coefficients on the edge of wind-ward parapet by 25 - 50%.

The coefficient for Load Case B overestimates the net pressure coefficients on the edge of lee-ward parapet by 20 – 30 %.

Wind tunnel experimentations, with their reasonable agreement with full-scale data, will continue to be beneficial for research and applications. On the other hand, full-scale investigation is essential to validate the wind tunnel testing results. Properly conducted field testing can also overcome the difficulties of laboratory test deficiencies (Mehta, 2004).

Numerical simulation results of wind flow around a low-rise building with parapet, using Fluent 6.1.22, show that the computed mean pressure coefficients on parapets and on the

roof with parapet agree with the wind tunnel data, for wind perpendicular to the building face. The RNG  $k$ - $\varepsilon$  turbulence model shows better performance in predicting mean pressures when compared with the RLZ  $k$ - $\varepsilon$  model.

It can be realized that it is possible to achieve similar trends, of numerical simulations and experimental measurements, for mean wind pressures over a low-rise building. However, equivalence between results of the two techniques may be achieved with care taken to provide accurate inlet flow profiles, adequate grid resolution, proper boundary conditions and appropriate turbulent model.

As also concluded by Stathopoulos (2002-c), the numerical wind tunnel is still virtual rather than real and further experimental studies will be required to increase the level of confidence in the computational results, in spite of some interesting and visually impressive results produced with Computational Wind Engineering (CWE).

### **7.3 Recommendations Based on the Current Study**

For the design of the main wind force-resisting system the ASCE 7-02 standard recommends net coefficients ( $GC_p$ ) of + 1.8 and - 1.1 for the windward and leeward parapets, respectively. However, after completion of preliminary work on which the present study is based (Stathopoulos et al., 2002-a and 2002-b), these values were revised in the ASCE 7-05 version to + 1.5 and - 1.0, respectively.

With regards to the loads on the components and cladding, ASCE 7-05 recommends  $GC_p$  values of + 3.8 and – 2.4 for windward and leeward parapets, respectively, at edge region and + 2.8 and – 2.2 for mid-span location. Based on the results of the present study, the following recommendations can be proposed for wind standards and codes of practice, particularly for the ASCE 7-05 (the design wind pressure on the components and claddings of parapets):

- Wall pressure coefficients can be used as a good estimate for those on the exterior parapet surface.
- Pressure coefficients on the corner of the interior parapet surface can be reduced from + 3.8 and – 2.4 for windward and leeward parapets, respectively, to + 2.4 and – 2.0.
- Pressure coefficients on the mid-span of the interior parapet surface can be from + 2.8 and – 2.2 for windward and leeward parapets, respectively, to + 2.0 and – 1.8.

#### **7.4 Limitations of the Presents Study**

Although every effort has been made to produce the best possible results in terms of wind-induced pressures on parapets, there are some limitations to be mentioned. These include but are not limited to the following:

- Using specific building configuration and exposure in the full-scale testing, which may not be representative of other cases

- Using sampling rate of 1 Hz in field measurements may not be adequate to capture the most critical peak values. However, comparisons with the results obtained by using higher frequencies are encouraging.

## **7.5 Future Work**

The current thesis has addressed some outstanding concerns regarding to the design wind loads of parapets on low-rise buildings. By providing a complete data set, further studies may assist in expanding the understanding of the results presented in this study. Future research will also help in answering questions raised from the present results. The proposed experimental and numerical investigations are listed as follows:

- Examining different building and parapet heights:

The current study deals with specific building and parapet height. Only two parapet heights were tested in the wind tunnel. It is recommended to study the effect of parapet height on parapet loads by examining different parapet heights. It is also recommended to examine parapet loads for different building heights.

- Measuring surface pressures on a single parapet:

The experimentations conducted in the current study considered a parapet extending around the entire perimeter of the building. Some previous studies experienced significant changes in roof corner pressures in the case of an isolated parapet (Stathopoulos and Baskaran, 1988; Mans et al., 2003). A single parapet located at

the leading corner of the building roof may significantly change the flow dynamics around the building, as the corner vortex from the separation at the roof will interact with a second vortex associated with separation from the end of the parapet (Mans et al., 2003). It is suggested that a full-scale study may be performed using a parapet located along a single building edge. Pressures may be recorded on the exterior and interior surfaces of such parapet and compared with the present results of the perimeter parapet.

- Visualizing the flow field around the parapets:

A flow visualization study may be useful in understanding the physical nature of wind flow above the parapet and clarifying the existing pressure data. The study can include different building and parapet heights in addition to a single parapet. Such study may also help in verifying whether the current results are appropriate for different building configurations.

- Numerical computation of peak pressures:

The current numerical simulation is performed in steady-state conditions and thus only mean pressures are provided. In order to compute wind-induced peak pressures on parapets, and hence calculate the design wind loads, the time dependant form of RANS equations needs to be solved. Either Large Eddy Simulation (LES) or the Algebraic Stress Model can be used. In this case different wind directions may be examined as it was concluded that the largest peak pressures on a parapet occur at an oblique wind angle, i.e. near  $45^\circ$ .

## ***REFERENCES***

Adams, E., Johnston, J., 1998. 'Flow Structure in the Near Wall Zone of a Turbulent Separated Flow'. *Journal of American Institute of Aeronautics and Astronautics, AIAA*. 26: 932-939.

ANSI A.58.1. 'Minimum Design Loads for Building and Other Structures'. American National Standards Institute, New York.

ASCE-7, 2005. 'Minimum Design Loads on Buildings and Other Structures'. American Society of Civil Engineers.

ASHRAE, 1999. 'Hand book Applications'. American Society of Heating, Refrigerating and Air-Conditioning Engineers. Millstar Electronic Publishing Group, Inc.

Baskaran, A., Stathopoulos, T., 1988. 'Roof Corner Wind Loads and Parapet Configuration'. *Journal of Wind Engineering and Industrial Aerodynamics*, 29: 79-88.

Bienkiewicz, B. and Sun, Y., 1992. 'Local Wind Loading on the Roof of a Low-rise Building'. *Journal of Wind Engineering and Industrial Aerodynamics*, 45: 11-24.

Blackmore, P., 1988. 'Load Reduction on Flat Roofs – The Effect of Edge Profile'. *Journal of Wind Engineering and Industrial Aerodynamics*, 29: 89-98.

Blocken, B., Carmeliet, J., Stathopoulos, T., 2007-a. 'CFD Evaluation of the Wind Speed Conditions in Passages Between Buildings—Effect of Wall-Function Roughness Modifications on the Atmospheric Boundary Layer Flow'. *Journal of Wind Engineering and Industrial Aerodynamics*. 95: 941–962.

Blocken, B., Stathopoulos, T., Carmeliet, J., 2007-b. 'CFD Simulation of the Atmospheric Boundary Layer–Wall Function Problems'. *Atmospheric Environment*. 41: 238–252.

Blocken, B., Stathopoulos, T., Saathoff, P., Wang, X., 2008. 'Numerical Evaluation of Pollutant Dispersion in the Built Environment: Comparisons between Models and Experiments'. *Journal of Wind Engineering and Industrial Aerodynamics*, 96: 1817-1831.

Cebeci, T., Bradshaw, P., 1977. 'Momentum Transfer in Boundary Layers'. Hemisphere Publishing Corporation, New York.

Chang, C., Meroney, R., 2003-a. 'The Effect of Surroundings with Different Separation Distances on Surface Pressures on Low-Rise Buildings'. *Journal of Wind Engineering and Industrial Aerodynamics*, 91: 1039-1050.

Chang, C., Meroney, R., 2003-b. 'Concentration and Flow Distributions in Urban Street Canyons: Wind Tunnel and Computational Data'. *Journal of Wind Engineering and Industrial Aerodynamics*, 91: 1141-1154.

Cheng, Y., Lien, F., Yee, E., Sinclair, R., 2003. 'A Comparison of Large Eddy Simulations with a Standard  $k-\varepsilon$  Reynolds-Averaged Navier–Stokes Model for the Prediction of a Fully Developed Turbulent Flow over a Matrix of Cubes'. *Journal of Wind Engineering and Industrial Aerodynamics*, 91: 1301–1328.

Cheung, J., Holmes, J., Melbourne, W., Lakshmanan, N., Browditch, P., 1997. 'Pressure on a 1/10 Scale Model of the Texas Tech Building'. *Journal of Wind Engineering and Industrial Aerodynamics*, 69-71: 529-538.

Columbus, J., 1972. 'The Study of Pressure Coefficients on Large Flat Roofs and Effects of Parapets on These Coefficients'. Engineering Science 400 report, University of Western Ontario, London, Canada.

Cook, N., 1985. 'The Designers Guide to Wind Loading of Building Structures'. Butterworth.

Daugherty, R., et al., 1983. 'Fluid Mechanics with Engineering Applications'. 8th edition, McGraw-Hill, New York.

Davenport, A., 1961. 'The Spectrum of Horizontal Gustiness near the Ground in High Winds'. *Quarterly Journal of the Royal Metrological Society*, 87: 372.

Davenport, A., Surry, D., 1974. 'The Pressure on Low-Rise Structures in Turbulent Wind'. Proceed of the Canadian Structural Engineering conference, the Canadian Steel Industrial construction Council, 1-39.

Eaton, K., Mayne, J., 1975. 'The Measurement of Wind Pressures on Two-Story Houses at Alesbury'. Journal of Wind Engineering and Industrial Aerodynamics, 1: 67-109.

ESDU, 1983. 'Strong Winds in the Atmospheric Boundary Layer. Part 1: Mean-Hourly Wind Speeds'. Engineering Sciences Data Unit, Data Item 82026.

Ferziger, J., Peric, M., 1999. 'Computational Methods for Fluid Dynamics'. 2<sup>ed</sup> edition. Springer-Verlag Berlin Heidelberg.

Flowe, A., Kumar, A., 2000. 'Analysis of Velocity Fields and Dispersive Cavity Parameters as A Function of Building Width to Building Height Ratio Using a 3-D Computer Model for Squat Buildings'. Journal of Wind Engineering and Industrial Aerodynamics, 86: 87-122.

Fluent 6.1.22, 2005. 'User's Guide'. Fluent Incorporated.

Gao, Y., Chow, W., 2005. 'Numerical Studies on Air Flow Around a Cube'. Journal of Wind Engineering and Industrial Aerodynamics, 93: 115-135.

Gumble, E., 1958. 'Statistics of Extremes'. Columbia University Press, New York, USA.

Gumley, S., 1983. 'Tubing Systems for Pneumatic Averaging of Fluctuating Pressures'. *Journal of Wind Engineering and Industrial Aerodynamics*, 12: 189-228.

Hall, D., Spanton, A., Macdonald, R., Walker, S., 1996. 'A Review of Requirements for Simple Urban Dispersion Models'. Building Research Establishment, BRE Client Report CR 77/96.

Ham, H., Bienkiewicz, B., 1992. 'Local Wind Loading on the Roof of a Low-Rise Building'. *Journal of Wind Engineering and Industrial Aerodynamics*, 45: 11-24.

Ham, H., Bienkiewicz, B., 1998. 'Wind Tunnel Simulation of TTU Flow and Building Roof Pressure'. *Journal of Wind Engineering and Industrial Aerodynamics*, 77-78: 119-133.

Hanson, T., Summers, D., Wilson, C., 1984. 'Numerical Modelling of Wind Flow over Buildings in Two Dimensions'. *International Journal for Numerical Fluids*, 4:25-41.

He, J., Song, S., 1997. 'A Numerical Study of Wind Flow around the TTU Building and the Roof Corner Vortex'. *Journal of Wind Engineering and Industrial Aerodynamics*, 67-68: 547-558.

Ho, T., 1992. 'Variability of Building Wind Loads'. Ph.D. Thesis. University of Western Ontario, London, Ontario, Canada.

Ho, T., Surry, D., Davenport, A., 1991. 'Variability of Low Building Wind Loads Due to Surroundings'. *Journal of Wind Engineering and Industrial Aerodynamics*, 38: 297-310.

Ho, T. Surry, D., Morrish, D., Kopp, G., 2005. 'The UWO Contribution to the NIST Aerodynamic Database for Wind Loads on Low Buildings: Part 1. Archiving Format and Basic Aerodynamic Data'. *Journal of Wind Engineering and Industrial Aerodynamics*, 93: 1-30.

Holems, J., 1984. 'Effect of Frequency Response on Peak Pressure Measurements'. *Journal of Wind Engineering and Industrial Aerodynamics*, 17: 1-9.

Holmes, J., Moriarty, W., 1999. 'Application of the generalized Pareto Distribution to Extreme Value Analysis in Wind Engineering'. *Journal of Wind Engineering and Industrial Aerodynamics*, 83: 1-10.

Hoxey, R., Moran, P., 1983. 'A Full-Scale Study of Geometric Parameters that Influence Wind Load on Low- Rise Buildings'. *Journal of Wind Engineering and Industrial Aerodynamics*, 13: 277-288.

Hoxey, R., Robertson, A., 1986. 'Pressure Coefficients for Low-Rise Building Envelopes Derived from Full-Scale Experiments'. *Journal of Wind Engineering and Industrial Aerodynamics*, 53: 283-297.

Hoxy, R., Robertson, A., Richardson, G., Short, J., 1997. 'Correction of Wind-Tunnel Pressure Coefficients for Reynolds Number Effect'. *Journal of Wind Engineering and Industrial Aerodynamics*. 69: 547-555.

Hunt, A. 1982. 'Wind-Tunnel Measurements of Surface Pressures on Cubic Building Models at Several Scales', *Journal of Wind Engineering and Industrial Aerodynamics*, 10: 137-163.

Kareem, A., Lu, P., 1992. 'Pressure Fluctuations on Flat Roofs with Parapets'. *Journal of Wind Engineering and Industrial Aerodynamics*, 41: 1775-1786.

Kasperski, M., 1996. 'Design Wind Loads for Low-Rise Buildings: A Critical Review of Wind Load Specifications for Industrial Buildings'. *Journal of Wind Engineering and Industrial Aerodynamics*, 61: 169-179.

Kawai, H., 1997. 'Structure of Conical Vortices Related with Suction Fluctuation on a Flat Roof in Oblique Smooth and Turbulent Flows'. *Journal of Wind Engineering and Industrial Aerodynamics*, 69: 579-588.

Kind, R., 1974. 'Wind Tunnel Tests on Building Models to Measure Wind Speeds at Which Gravel is Blown off Roof-Tops'. National Research Council of Canada, Ottawa, Ontario.

Kind, R., 1986. 'Worst Suctions near Edges of Flat Rooftops on Low-Rise Buildings'. *Journal of Wind Engineering and Industrial Aerodynamics*, 25: 31-47.

Kind, R., 1988. 'Worst Suctions Near Edges of Flat Rooftops With parapets'. *Journal of Wind Engineering and Industrial Aerodynamics*, 31: 251-264.

Kleiser, L., Zang, T., 1991. 'Numerical Simulation of Transition in Wall-Bounded Shear Flows'. *Annul Review of Fluid Mechanics*, 23: 495-537.

Kopp, G., Surry D., Mans, C., 2005. 'Wind Effects of Parapets on Low Buildings: Part 1. Basic Aerodynamics and Local Loads'. *Journal of Wind Engineering and Industrial Aerodynamics*, 93: 817-841.

Kopp, G., Mans, C., Surry D., 2005. 'Wind Effects of Parapets on Low Buildings: Part 2. Structural Loads'. *Journal of Wind Engineering and Industrial Aerodynamics*, 93: 843-855.

Kopp , G., Mans, C., Surry, D., 2005. 'Wind Effects of Parapets on Low Buildings: Part 4. Mitigation of Corner Loads with Alternative Geometries'. *Journal of Wind Engineering and Industrial Aerodynamics*, 93: 873-888.

Kramer, C., et al., 1978. 'Wind Pressure on Block-Type Buildings'. *Proceed of 3<sup>ed</sup> coll. on Industrial Aerodynamics*, W. Germany, 241- 254.

Landsea, C., Pielke, Jr., R., 1998. 'Normal Hurricane Damages in the United States: 1925-1995'. *Weather and Forecasting*, 13: 621-631.

Laneville, A., 1990. 'Turbulence and Blockage Effects on Two-Dimensional Rectangular Cylinders'. *Journal of Wind Engineering and Industrial Aerodynamics*, 33: 11-20.

Lauder, B., Spalding, D., 1974. 'The Numerical Computation of Turbulent Flows'. *Computer Methods in Applied Mechanics and Engineering*, 3: 269-289.

Larose, G., D'Auteuil, A., 2006. On the Reynolds Number Sensitivity of the Aerodynamics of Bluff Bodies with Sharp Edges. *Journal of Wind Engineering and Industrial Aerodynamics*, 94: 365-376.

Lee, S., 1997. 'Unsteady Aerodynamic Force Prediction on a Square Cylinder using k- $\epsilon$  Turbulence Models'. *Journal of Wind Engineering and Industrial Aerodynamics*, 67: 79-90.

Leutheusser, H., 1964-a. 'The Effects of Wall Parapets on the Roof Pressure Coefficients of Plock-Type and Cylindrical Structures'. Technical Publication Series, No. TP6404, Department of Mechanical Engineering, University of Toronto, Toronto, Ont.

Leutheusser, H., 1964-b. 'Parapets Improve Roof Wind Loading'. *The Consulting Engineer*: 94-96.

Levitan, M., 1993. 'Analysis of Reference Pressure Systems used in Field Measurements of Wind Loads', Ph. D. Thesis, Texas Tech University, Texas, USA.

Levitan, M., Mehta, K., 1992-a. 'Texas Tech Field Experiments for Wind Loads part I: Building and Pressure Measuring System'. *Journal of Wind Engineering and Industrial Aerodynamics*, 41: 1565-1576.

Levitan, M., Mehta, K. 1992-b. 'Texas Tech Field Experiments for Wind Loads Part II: Meteorological Instrumentation and Terrain Parameters'. *Journal of Wind Engineering and Industrial Aerodynamics*, 41-44: 1577-1588.

Ligrani, P., Moffat, R., 1986. 'Structure of Transitionally Rough and Fully Rough Turbulent Boundary Layers'. *Journal of Fluid Mechanics*, 162:69-98.

Lin, J., Surry, D., 1998. 'The Variation of Peak Loads with Tributary Area near Corners on Flat Low Building roofs'. *Journal of Wind Engineering and Industrial Aerodynamics*, 77: 185-196.

Lin, J., Surry, D., Tieleman, H., 1995. 'The Distribution of Pressure near Roof Corners of Flat Roof Low Buildings'. *Journal of Wind Engineering and Industrial Aerodynamics*, 56: 235-265.

Lythe, G., Surry, D., 1983. 'Wind Loading of Flat Roof with and without Parapets'.  
Journal of Wind Engineering and Industrial Aerodynamics, 11: 75-94.

Mans, C. 2001. 'Wind Loads on Parapets'. M.Sc., University of Western Ontario,  
London, Ontario, Canada.

Mans, C. Kopp, G. and Surry, D. 2003. 'Wind Loads on Low Buildings With Various  
Parapet Configurations'. Eleventh international conference on wind engineering.

Mans, C., Kopp, G., Surry, D., 2005. 'Wind Effects of Parapets on Low Buildings: Part 3.  
Parapet Loads'. Journal of Wind Engineering and Industrial Aerodynamics, 93: 857-872.

Marathe, R., 1992. 'Full Scale Study of Wind Loads on Flat Roofs with Parapets'. Master  
Thesis, Concordia University, Montreal, Canada.

Maruyama, T., et al. 2004. 'Field Experiment Measuring the Approaching Flows and  
Pressures on a 2.4 Cube'. 5<sup>th</sup> International Colloquium on Bluff Body Aerodynamics and  
Applications, Ottawa, Canada.

Mehta, K., Levitan, M., Iverson, R., McDonald, J., 1992. 'Roof Pressures Measured in  
the Field on a Low Building'. Journal of Wind Engineering and Industrial Aerodynamics,  
41: 181-192.

Mehta, K., 2004. 'Importance of Field Testing in Wind Engineering'. Proceeding of the National Conference on Wind Engineering, Nagpur, Phoenix Publication, New Delhi, India.

Melaragno, M., 1996. 'Severe Storm Engineering for Structural Design'. Gordon and Breach Science Publishers, Amsterdam.

Meroney, R., Leidl, B., Rafailidis, S., Schatzmann, M., 1999. 'Wind Tunnel and Numerical Modeling of Flow and Dispersion about Several Building Shapes'. Journal of Wind Engineering and Industrial Aerodynamics, 81: 333- 345.

Mikkelsen, A., Livesey, F., 1995. 'Evaluation of The Use of The Numerical  $K-\epsilon$  Chameleon II, For Predicting Wind Pressures On Building Surfaces'. Journal of Wind Engineering and Industrial Aerodynamics, 57: 375-389.

Mohan, M., Siddiqui, T., 1998. 'Analysis of Various Schemes for the Estimation of Atmospheric Stability Classification'. Journal of Atmospheric Environment, 32: 3775-3781.

Murakami, S., 1990. 'Computational Wind engineering'. Journal of Wind Engineering and Industrial Aerodynamics, 36: 517-538.

Murakami, S., Moshihiko, A., Hayashi, Y., 1990. 'Examining the  $k-\varepsilon$  Model by Means of a Wind Tunnel Test and Large Eddy Simulation of the Turbulence Structure around a Cube'. *Journal of Wind Engineering and Industrial Aerodynamics*, 35: 87-100.

Murakami, S., et al., 1992. 'Numerical Study on Velocity-Pressure Field and Wind Forces for Bluff Bodies by  $k-\varepsilon$ , ASM and LES'. *Journal of Wind Engineering and Industrial Aerodynamics*, 44: 2841-2852.

Murakami, S., Mochida, A., 1988. '3-D Numerical Simulation of Air Flow around a Cubic Model by Means of the  $k-\varepsilon$  Model'. *Journal of Wind Engineering and Industrial Aerodynamics*, 31: 283-303.

NBCC, 2005. 'Supplement to the National Building Code of Canada'. Association Committee on the National Building Code, National Research Council of Canada, Ottawa, Ont.

Norris, L. and Reynolds, W., 1975. 'Turbulent Channel Flow with a Moving Wavy Boundary'. Report No. FM-10, Department of Mechanical Engineering, Stanford University.

Okada, H., Ha, Y., 1992. 'Comparison of Wind-Tunnel and Full-Scale Pressure Measurement Tests on Texas Tech Building'. *Journal of Wind Engineering and Industrial Aerodynamics*, 41: 1601-1612.

Patankar, S., 1980. 'Numerical Heat Transfer and Fluid Flow'. McGraw-Hill, New York.

Paterson, D., 1986. 'Computation of Wind Flows over Three-Dimensional Buildings'.  
Ph.D. Thesis, Department of Civil Engineering, Queensland, Australia.

Pindado, S., and Meseguer, J. 2003. 'Wind-Tunnel Study on the Influence of Different Parapets on the Roof Pressure Distribution of Low-Rise Buildings'. *Journal of Wind Engineering and Industrial Aerodynamics*, 91: 1133-1139.

Richards, P., Hoxey, R., Connell, B., Lander, D., 2007. 'Wind-Tunnel Modeling of the Silsoe Cube'. *Journal of Wind Engineering and Industrial Aerodynamics*, 95: 1384-1399.

Richardson, G., Surry, D., 1991. 'Comparison of Wind-Tunnel and Full-Scale Surface Pressure Measurements on Low-Rise Pitched-Roof Buildings'. *Journal of Wind Engineering and Industrial Aerodynamics*, 38: 249-256.

Rhie, C., Chow, W., 1983. 'Numerical Study of the Turbulent Flow Past an Airfoil with Trailing Edge Separation'. *Journal of American Institute of Aeronautics and Astronautics*, 21: 1525-1532.

Robertson, A., 1992. 'The Wind Induced Response of Full-Scale Portal Framed Building'. *Journal of Wind Engineering and Industrial Aerodynamics*, 41:1677-1688.

Sadek, F., Simiu, E., 2002. 'Peak Non-Gaussian Wind Effects for Data-Base-Assisted Low-Rise Building Design'. *Journal of Engineering Mechanics*, 5: 530–539.

Sedefian, L., Bennet, E., 1980. 'A Comparison of Turbulence Classification Schemes'. *Journal of Atmospheric Environment*, 14: 741-750.

Selvam, R., 1992. 'Computation of Pressures on Texas Tech Building'. *Journal of Wind Engineering and Industrial Aerodynamics*, 41: 1619-1627.

Selvam, R., 1997. 'Computation of Pressures on Texas Tech University Building Using Large Eddy Simulation'. *Journal of Wind Engineering and Industrial Aerodynamics*, 67: 647-657.

Shih, T., Liou, W., Shabbir, A., Yang, Z., Zhu, J., 1995. 'A New  $k-\varepsilon$  Eddy Viscosity Model for High Reynolds Number Turbulent Flows- Model Development and Validation'. *Computers Fluids*, 24: 227-238.

Sill, B., Cook, N., Fang, C., 1992. 'The Aylesbury Comparative Experiment: A Final Report'. *Journal of Wind Engineering and Industrial Aerodynamics*, 41: 1553-1564.

Simiu, E., Scanlan, R., 1986. 'Wind Effects on Structures: An Introduction to Wind Engineering'. Wiley-Interscience, New York, 3<sup>rd</sup> edition.

Snaebjornsson, J., 2002. 'Full- and Model Scale Study of Wind Effects on a Medium-Rise Building in a Built Up Area'. PhD theses, Norwegian University of Science and Technology, Norway.

Socket, H., Taucher, R., 1980. 'The Influence of A Parapet on Local Pressure Fluctuations'. Proceed of 4<sup>th</sup> coll. on Industrial Aerodynamics, W. Germany, 107-118.

Sparks, P., Schiff, S., Reinhold, J., 1994, 'Wind Damage to Envelops of Houses and Consequent Insurance Losses'. Journal of Wind Engineering and Industrial Aerodynamics, 53: 145-155.

Stathopoulos, T., 1979. 'Turbulent Wind Action on Low-Rise Buildings'. Ph. D. Thesis, University of Western Ontario, Canada.

Stathopoulos, T., Surry, D., Davenport, A., 1981. 'Effective Wind Loads on Flat Roofs'. Journal of Structural Division, ASCE, 107: 281-297.

Stathopoulos, T., 1981. 'Wind Pressure Functions for Flat Roofs'. Journal of Engineering Mechanics Division, ASCE, 107: 889-905.

Stathopoulos, T., 1982. 'Wind Pressures on Low Buildings with Parapets'. Journal of the Structural Division, ASCE, 108: 2723-2736.

Stathopoulos, T., Surry, D., 1983. 'Scale Effects in Wind Tunnel Testing of Low-Building'. *Journal of Wind Engineering and Industrial Aerodynamics*, 13: 313-326.

Stathopoulos, T., 1984. 'Design and Fabrication of a Wind Tunnel for Building Aerodynamics'. *Journal of Wind Engineering and Industrial Aerodynamics*, 16: 361-376.

Stathopoulos, T., Baskaran, A., 1988-a. 'Wind Pressure on Flat Roofs with Parapets'. *Journal of Structural Engineering, ASCE*, 113:2166-2180.

Stathopoulos, T., Baskaran, A., 1988-b. 'Turbulent Wind Loading of Roofs with Parapet Configuration'. *Canadian Journal of Civil Engineering*, 15: 570, 578.

Stathopoulos, T., Baskaran, A., 1988-c. 'Roof Corner Wind Loads and Parapet Configurations'. *Journal of Wind Engineering and Industrial Aerodynamics*, 29: 79-88.

Stathopoulos, T., Baskaran, A., 1990-a, 'Full Scale Measurements of Wind Pressures on Flat Roof Corners'. *Journal of Wind Engineering and Industrial Aerodynamics*, 39: 1063-1072.

Stathopoulos, T., Baskaran, A., 1990-b. 'Boundary Treatment for the Computational Three-Dimensional Wind Flow Conditions Around a Building'. *Journal of Wind Engineering and Industrial Aerodynamics*, 35: 177-200.

Stathopoulos, T., Zhou, Y., 1993. 'Numerical Simulation of Wind-Induced Pressures on Buildings of Various Geometries'. *Journal of Wind Engineering and Industrial Aerodynamics*, 46-47: 419-430.

Stathopoulos, T., Marathe, R., Wu, H., 1999. 'Mean Wind Pressures on Flat Roof Corners Affected by Parapets: Field and Wind Tunnel Studies'. *Journal of Wind Engineering and Industrial Aerodynamics*, 21: 629-638.

Stathopoulos, T., Saathoff, P., 1991. 'Wind Pressure on Roofs of Various Geometries'. *Journal of Wind Engineering and Industrial Aerodynamics*, 38: 273-284.

Stathopoulos, T., Saathoff, P., Du, X. 2002-a. 'Wind Loads on Parapet'. *Journal of Wind Engineering and Industrial Aerodynamics*, 90: 503-514.

Stathopoulos, T., Saathoff, P., Bedair, R. 2002-b. 'Wind Pressure on Parapets of Flat Roofs'. *Journal of Architectural Engineering, ASCE*, 8: 49-54.

Stathopoulos, T., 2002-c. 'The Numerical Wind Tunnel for Industrial Aerodynamics: Real or Virtual in the new Millennium?'. *Wind and Structures*, 5:193-208.

St. Pierre, L., Kopp, G., Surry, D., Ho, T., 2005. 'The UWO Contribution to the NIST Aerodynamic Database for Wind Loads on Low Buildings: Part 2. Comparison of Data with Provisions'. *Journal of Wind Engineering and Industrial Aerodynamics*. 93: 31-59.

Streeter, V., 1971. 'Fluid Mechanics'. 5th edition, McGraw-Hill, New York.

Suresh Kumar, K., 1998. 'Simulation of Fluctuating Wind Pressures on Low Building Roofs'. Ph.D. thesis. Concordia University, Montreal, Canada.

Surry, D., 1989. 'Pressure Measurements on Texas Tech Building-II: Wind Tunnel Measurements and Comparison with Full-Scale'. Proceed of the eighth coll. on Industrial Aerodynamics and Wind Engineering, W. Germany.

Surry, D., Lin, J., 1995. 'The Effect of Surroundings and Roof Corner Geometric Modifications on Roof Pressures on Low-Rise Buildings'. Journal of Wind Engineering and Industrial Aerodynamics, 58: 113-138.

Tamura, T., et al., 1997. 'Numerical Prediction of Wind Loading on Buildings and Structures—Activities of AIJ Cooperative Project on CFD'. Journal of Wind Engineering and Industrial Aerodynamics, 67–68: 671–685.

Tieleman, H., Hajj, M., Reinhold, T., 1998. 'Wind Tunnel Simulation Requirements to Assess Wind Loads on Low Rise Building'. Journal of Wind Engineering and Industrial Aerodynamics, 74: 675-685.

Tieleman, H., 2003. 'Roughness Estimation for Wind-Load Simulation Experiments'. Journal of Wind Engineering and Industrial Aerodynamics, 91: 1163-1173.

Tieleman, H., 2003. 'Wind Tunnel Simulation of Wind Loading on Low-Rise Structures: A Review'. *Journal of Wind Engineering and Industrial Aerodynamics*, 91: 1627-1649.

Uematsu, Y., Isyumov, N., 1998. 'Peak Gust Pressures Acting on the Roof and Wall Edges of a Low-Rise Building'. *Journal of Wind Engineering and Industrial Aerodynamics*, 77-78: 217-231.

Uematsu, Y., Isyumov, N., 1999. 'Review: Wind Pressures Acting on Low-Rise Building'. *Journal of Wind Engineering and Industrial Aerodynamics*, 82: 1-25.

Van Dormal, J., Raithby, G., 1984. 'Enhancement of the SIMPLE Method for Predicting Incompressible Fluid Flow'. *Journal of Heat transfer*, 7: 147-163.

Versteeg, H., Malalasekera, W., 1995. 'An Introduction to Computational Fluid Dynamics – The Finite Volume Method'. John Wiley and sons, New York.

Von Karman, T., 1948. 'Progress in the Statistical Theory of Turbulence. Proceeding of National Academic Society, 34: 530-539.

Wagaman, S., Rainwater, K., Mehta, K., Ramsey, R., 2002. 'Full-Scale Flow Visualization over a Low-Rise Building'. *Journal of Wind Engineering and Industrial Aerodynamics*, 90:1-8.

Wang, Z., Plate, E., Rau, M., Keiser, R., 1996. 'Scale Effects in Wind Tunnel Modeling'. *Journal of Wind Engineering and Industrial Aerodynamics*, 61: 113-130.

White, F., 1991. 'Viscous Fluid Flow'. 2<sup>nd</sup> edition, McGraw-Hill, New York.

Wieringa, J., 1993. 'Representative Roughness Parameters for Homogeneous Terrain'. *Boundary-Layer Meteorol.* 63:323-363.

Wu, F., Sarkar, P., Mehta, K., Zhou, Z., 2001. 'Influence of Incident Wind Turbulence on Pressure Fluctuations near Flat-Roof Corners'. *Journal of Wind Engineering and Industrial Aerodynamics*, 89: 403-420.

Yakhot, V., et al., 1992. 'Development of Turbulence Models for Shear Flows by a Double Expansion Technique'. *Journal of physics Fluid*, A4: 1510–1520.

Zhang, A., Gu, M., 2008. 'Wind Tunnel Tests and Numerical Simulations of Wind Pressures on Buildings in Staggered Arrangement'. *Journal of Wind Engineering and Industrial Aerodynamics*, 96: 2067–2079.

Zhou, Y., 1995. 'Numerical Evaluation of Wind Effects on Buildings'. Ph.D. Thesis, Concordia University, Montréal, Canada.

## ***APPENDIX A***

### **A.1 Velocity and Turbulence Parameters**

Mean wind speed ( $\bar{U}$ ) decreases with a decreasing distance from the ground, because of frictional effect. A common representation of the wind profile above the earth's surface is the '*power law*', which is employed as an empirical model for mean wind speed profiles and is given by:

$$\frac{\bar{U}}{U_g} = \left( \frac{z}{z_g} \right)^\alpha \quad \text{A.1}$$

where:  $z$  is the height above the mean ground level,  $z_g$  is the gradient height, which is equivalent to the top of the boundary layer and where the velocity is constant (gradient velocity,  $U_g$ ) and  $\alpha$  is the power exponent parameter.

The boundary layer profile approaches zero speed at the ground surface and its shape may be sensitive to the local roughness effect and the '*logarithmic law*' may be applied:

$$\bar{U} = \frac{1}{K} C_g \ln \left( \frac{z}{z_o} \right) \quad \text{A.2}$$

where:  $K$  is Von Karman's constant (0.4 – 0.42),  $C_g$  is the geostrophic drag coefficient and  $z_o$  is the roughness length parameter.

The ‘*turbulence intensity*’ is a simple measure of the gustiness (turbulence) wind within a specific time period, when the mean wind velocity was defined. The longitudinal component can be defined as:

$$I_u = \frac{\sigma_u}{\bar{U}} \quad \text{A.3}$$

where:  $\sigma_u$  is the standard deviation of a fluctuating wind velocity and  $\bar{U}$  is the mean along wind velocity. Another commonly used measure of the variability of the wind is the ‘*gust factor*’ which is defined as:

$$G_u = \frac{|U_u|_{\max}}{\bar{U}} \quad \text{A.4}$$

where:  $|U_u|_{\max}$  is the largest maximum recorded wind velocity during a specific time period.

A more detailed approach for the analysis of turbulence phenomena is by means of ‘*power spectral density function*’, which define the process in time rather than amplitude domain. Spectrum of longitudinal turbulence ( $S_n$ ) represents the distribution of turbulence energy over a frequency range in which:

$$\sigma^2 = \int_0^{\infty} S(n)dn \quad \text{A.5}$$

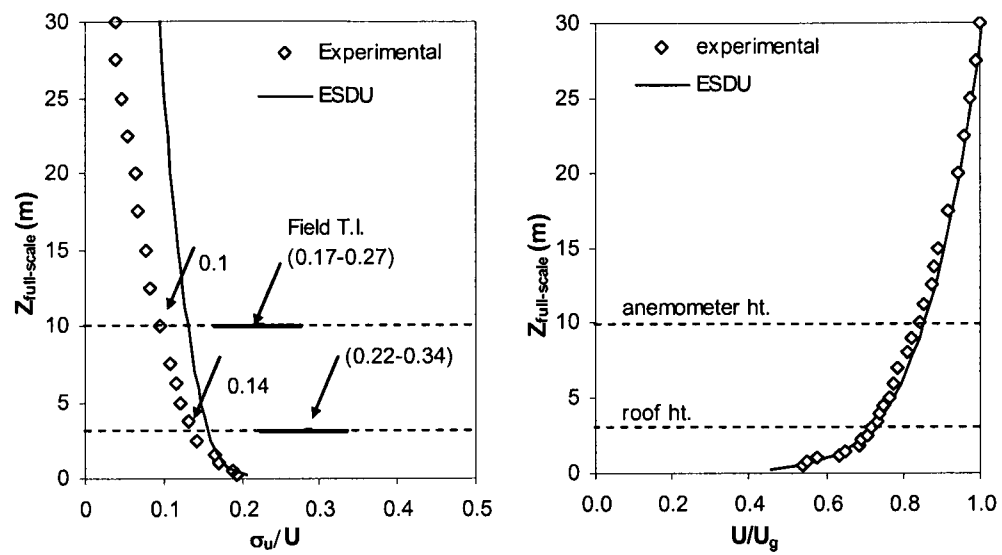
Spectra measurements are performed for the current flow conditions. The experimental data has been compared with some empirical and analytical representations such as Davenport’s empirical equation (Davenport, 1961) and Von-Karman’s analytical expression (Von-Karman, 1948), respectively:

$$\frac{nS_{(n)}}{\sigma^2} = \frac{2}{3} \left( \frac{x^2}{(1+x^2)^{4/3}} \right) \quad x = 1200 \frac{n}{\overline{V}_{10}} \quad \text{A.6}$$

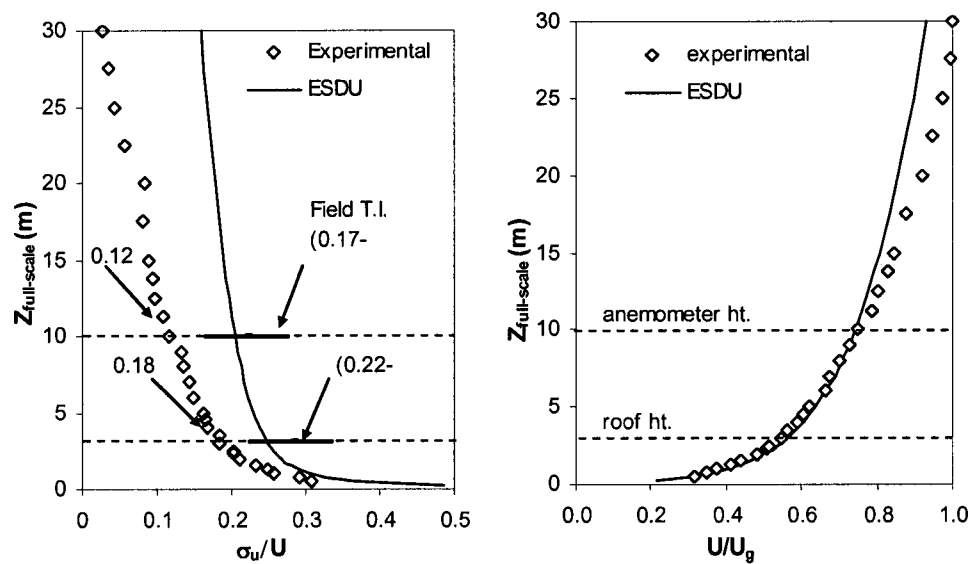
$$\frac{nS}{\sigma^2} = \frac{4x}{(1+70.8x^2)^{5/6}} \quad x = \frac{nL_x}{\overline{V}_z} \quad \text{A.7}$$

where  $n$  is the frequency and  $x$  is a non-dimensional frequency, used to normalize the standard spectra by the appropriate variance,  $\sigma^2$ , with

$$L_x = \frac{25(z-d)^{0.35}}{z_o^{0.063}} \quad (\text{m}) \quad \text{A.8}$$

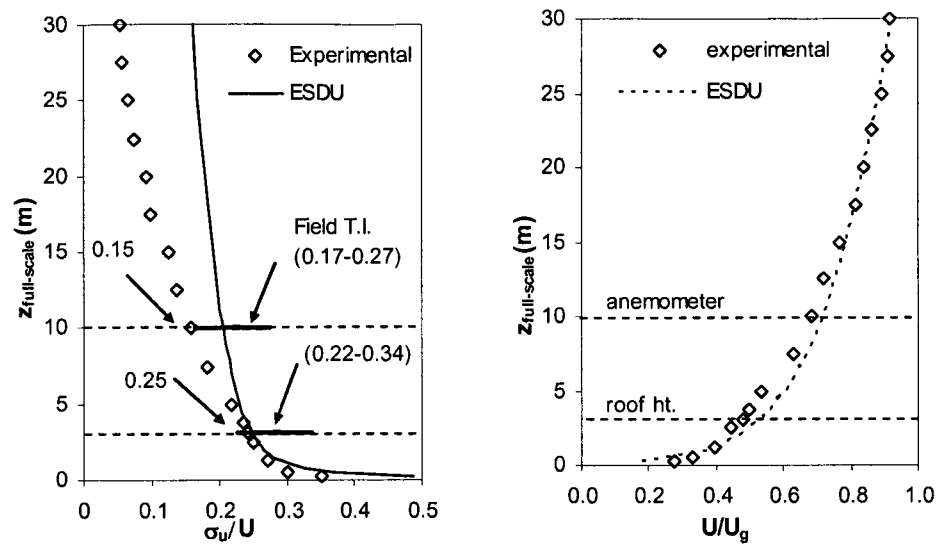


(a) Terrain-1

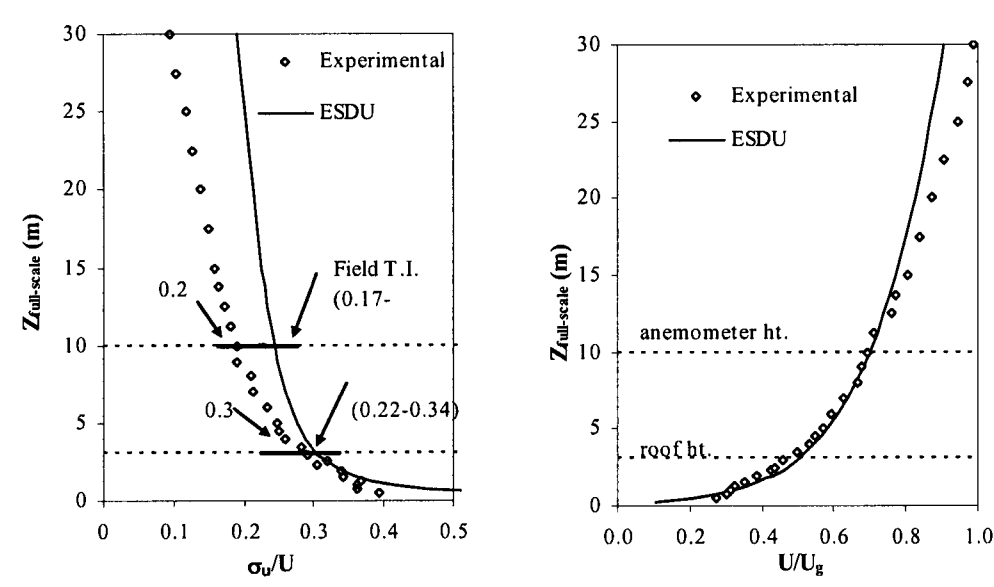


(b) Terrain-2

Figure A.2: Mean velocity and turbulence intensity profiles for different exposures



(c) Terrain-3



(d) Terrain-5

Figure A.2: Continued

## A.2 Anemometer Calibration

The calibration consists of placing the anemometer in the wind tunnel and recording the corresponding output in terms of volts for various speeds. Simultaneously, the wind speed is measured using a hot-wire probe. Subsequently, a graph is plotted of volts vs. wind speed in m/sec and the points are fitted by a straight line (Figure A.1).

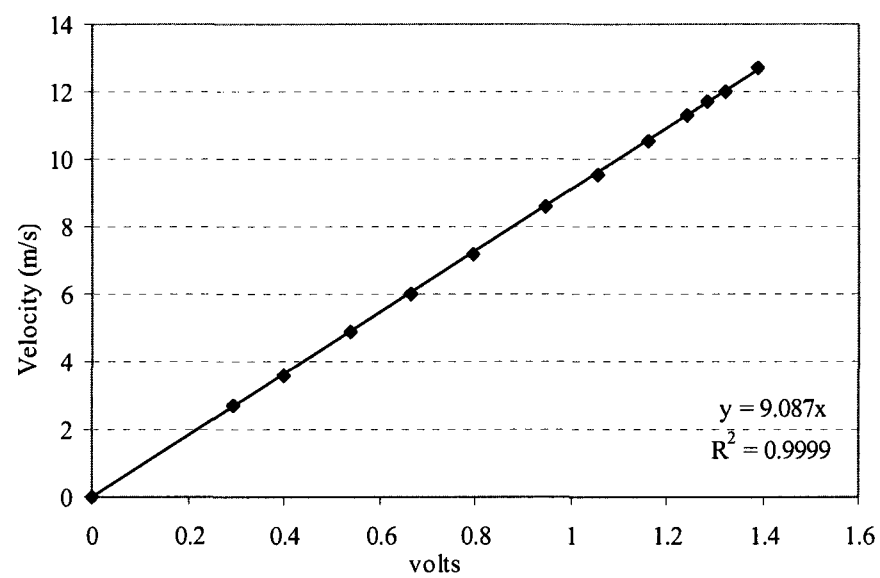


**Figure A.1: Calibration of the anemometer used in field testing**

### A.3 DSM System Setting and Operating Principle

Figure A.3 shows a diagram for installing the Digital Surface Module (DSM-3000) system as presented by Wang, 2005. Two transducers are used, each of 64 scanning channels. A host computer can control the DSM computer via Internet, while the DSM computer connected to the Zero-Operate-Calibrate (ZOC-33) pressure scanner through local cable connection. At the same time, the DSM computer controls a device named DSM-CPM that organizes the working mode of the ZOC-33 pressure scanner. Figure A.4 shows the ZOC-33 valve system and operating modes diagram. ZOC-33 incorporates integrated pneumatic valves that allow four working modes, namely, Purge, Calibrate, Operate and Leak-Test. These modes are controlled by two pistons respectively.

By setting the period in microseconds ( $\mu\text{s}$ ) to  $62 \mu\text{s}$ :

The scanning frequency =  $1 / 64 \text{ channels} \times (62 \times 10^{-6}) \text{ sec} \sim 250 \text{ Hz}$ .

In wind tunnel testing strong wind is simulated, therefore a velocity scale of 1/2 is assumed. For 1/50 length scale, the time scale is obtained as follows:

$$\frac{T_{\text{model}}}{T_{\text{full-scale}}} = \left( \frac{L_{\text{model}}}{L_{\text{full-scale}}} \right) \left( \frac{V_{\text{model}}}{V_{\text{full-scale}}} \right) \quad \text{A.9}$$

Corresponding to 10 minutes in full-scale, scanning time in wind tunnel = 24 sec.

Therefore, 6000 frame / scan are obtained ( $250 \text{ Hz} \times 24 \text{ sec}$ ).

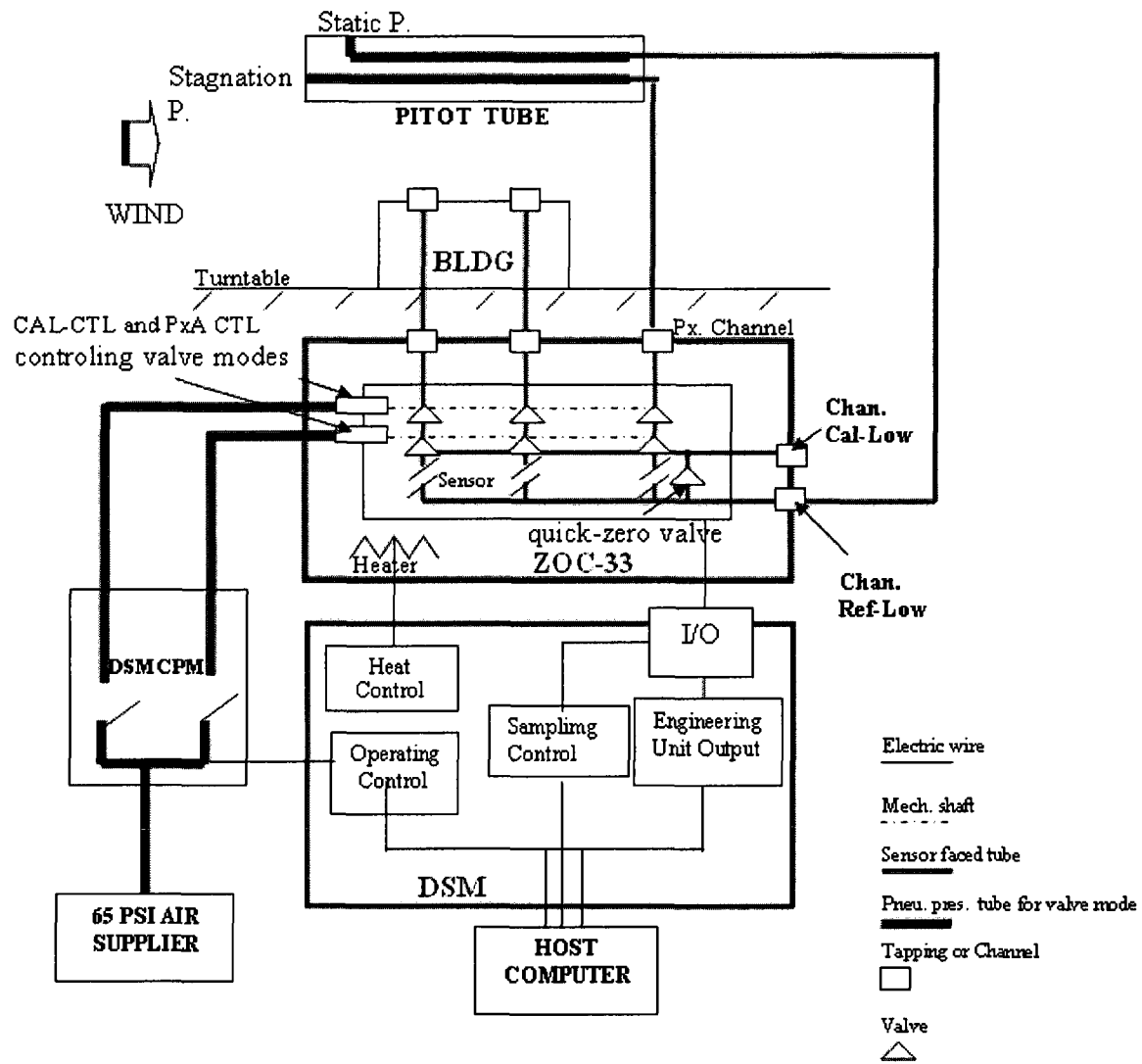


Figure A.3: DSM-3000 system diagram (Wang, 2005)

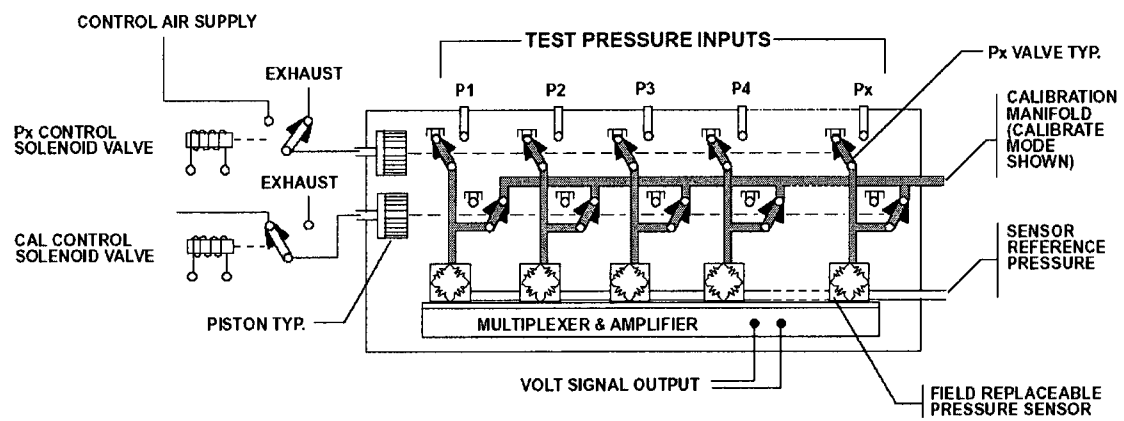
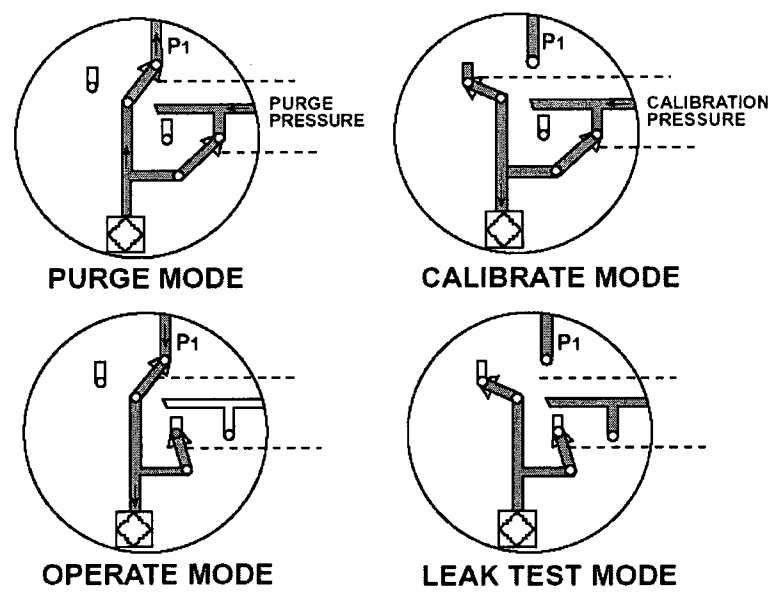


Figure A.4: ZOC-33 system diagram (Wang, 2005)

## A.5 Gumbel Plot

Gumbel's plot (Gumbel, 1958) is used to determine the probability term  $P$  as follows:

$$\ln[-\ln(P)] = -\frac{(x-m)}{s} \quad (\text{A.10})$$

which can be written as:

$$x = m + sy \quad (\text{A.11})$$

where,  $y = -\ln[-\ln(P)]$  is the reduced  $y$ -variant,  $m$  is the mode and  $s$  is the dispersion.

The observed extreme values are sorted into ascending order of magnitude, after which is assigned a rank,  $r$ , where  $r = 1$  for the smallest and  $r = n$  for the largest of  $n$  values. An estimate of  $P$  corresponding to each extreme value can be calculated from their ranks as follows:

$$P = \frac{r}{n+1} \quad (\text{A.12})$$

The mode and dispersion can be determined from plotting equation A.11. Mode corresponds to the  $x$  value when the reduced  $y$ -variant is zero and the dispersion is the slope of the line fitting the data (Suresh Kumar, 1998).

## **APPENDIX B**

### **B.1 Wind Speed and Turbulence Intensity Profiles (ESDU, 1983)**

The ESDU (82026) equilibrium mean wind speed and turbulence intensity model has three scaling parameters: roughness height  $z_o$ , friction velocity,  $u^*$  and the gradient height  $z_g$ . The velocity profile can be calculated as follows:

$$u(z) = 2.5u^* \left[ \ln\left(\frac{z}{z_o}\right) + \frac{23}{4} \frac{z}{z_g} - \frac{15}{8} \left(\frac{z}{z_g}\right)^2 - \frac{4}{3} \left(\frac{z}{z_g}\right)^3 + \frac{1}{3} \left(\frac{z}{z_g}\right)^4 \right] \quad (\text{B.1})$$

This equation is valid up to  $z_g$  in which:

$$z_g = \frac{u^*}{6f_c} \quad (\text{B.2})$$

where  $f_c$  is the Coriolis parameter, which depends on earth's self rotation and latitude.

Eq. B.1 can be simplified for speed profile up to 300 m as follows:

$$u(z) = 2.5u^* \left[ \ln\left(\frac{z}{z_o}\right) + \frac{34.5f_c z}{u^*} \right] \quad (\text{B.3})$$

The turbulence intensity can be obtained as follows:

$$I_u = \frac{u'(z)}{u(z)} = \left( \frac{u'(z)}{u^*} \right) \left( \frac{u^*}{u(z)} \right) \quad (\text{B.4})$$

where:  $u'(z)$  is fluctuation component of the wind velocity and:

$$\frac{u'(z)}{u^*} = \frac{7.5\eta [0.538 + 0.09 \ln(z/z_o)]^{\eta^{16}}}{1 + 0.156 \ln(u^*/(f_c z_o))} \quad (\text{B.5})$$

where:  $\eta = 1 - \frac{6f_c z}{u^*}$

## **B.2 Minimum Design Loads for Buildings and Other Structures,**

**[This Section has been taken verbatim from ASCE 7-05]**

### **Parapets: (Analysis Procedures)**

#### **B.2.1 Main wind force-resisting system**

The design wind pressure for the effect of parapets on main wind force-resisting systems of rigid, low-rise or flexible buildings with flat, gable, or hip roofs shall be determined by the following equation:

$$p_p = q_p GC_{pn} \text{ (lb/sf)} \quad \textbf{(B.6)}$$

where

$p_p$  = combined net pressure on the parapet due to the combination of the net pressures from the front and back parapet surfaces. Plus (and minus) signs signify net pressure acting toward (and away from) the front (exterior) side of the parapet.

$q_p$  = velocity pressure evaluated at the top of the parapet.

$GC_{pn}$  = combined net pressure coefficient;

= + 1.5 for windward parapet

= - 1.0 for leeward parapet.

### B.2.2 Components and cladding

The design wind pressure on the components and claddings elements of parapets shall be designed by the following equation:

$$p = q_p (GC_p - GC_{pi}) \quad (\text{B.7})$$

where

$q_p$  = velocity pressure evaluated at the top of the parapet.

$GC_p$  = external pressure coefficient from Figure B.1.

$GC_{pi}$  = internal pressure coefficient from Table B.1, based on the porosity of the parapet envelop.

Two load cases shall be considered:

Load Case A shall consist of applying the applicable positive wall pressure from Figure B.1 to the front surface of the parapet while applying the applicable negative edge or corner zone roof pressure from Figure B.2 to the back surface.

Load Case B shall consist of applying the applicable positive wall pressure from Figure B.1 to the back of the parapet surface, and applying the applicable negative wall pressure from Figure B.1 to the front surface.

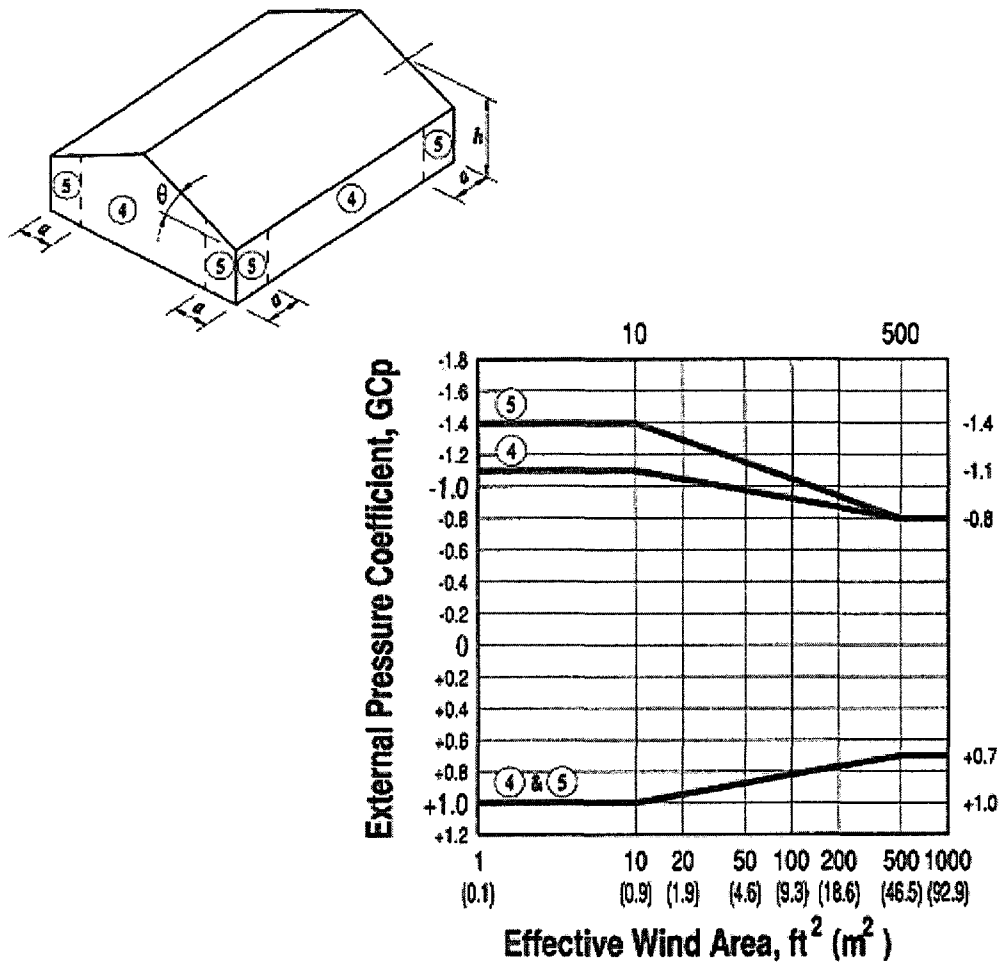
Edge and corner zones shall be arranged as shown in Figures B.1 and B.2.  $GC_p$  shall be determined for appropriate roof angle and effective wind areas from Figures B.1 and B.2. if internal pressure is present, both load cases should be evaluated under positive and negative internal pressure.

**Table B.1 Internal Pressure coefficient,  $GC_{pi}$**

<b>Enclosure Classification</b>	<b><math>GC_{pi}</math></b>
Open Buildings	0.00
Partially Enclosed Buildings	+ 0.55 or - 0.55
Enclosed Buildings	+ 0.18 or - 0.18

**Notes:**

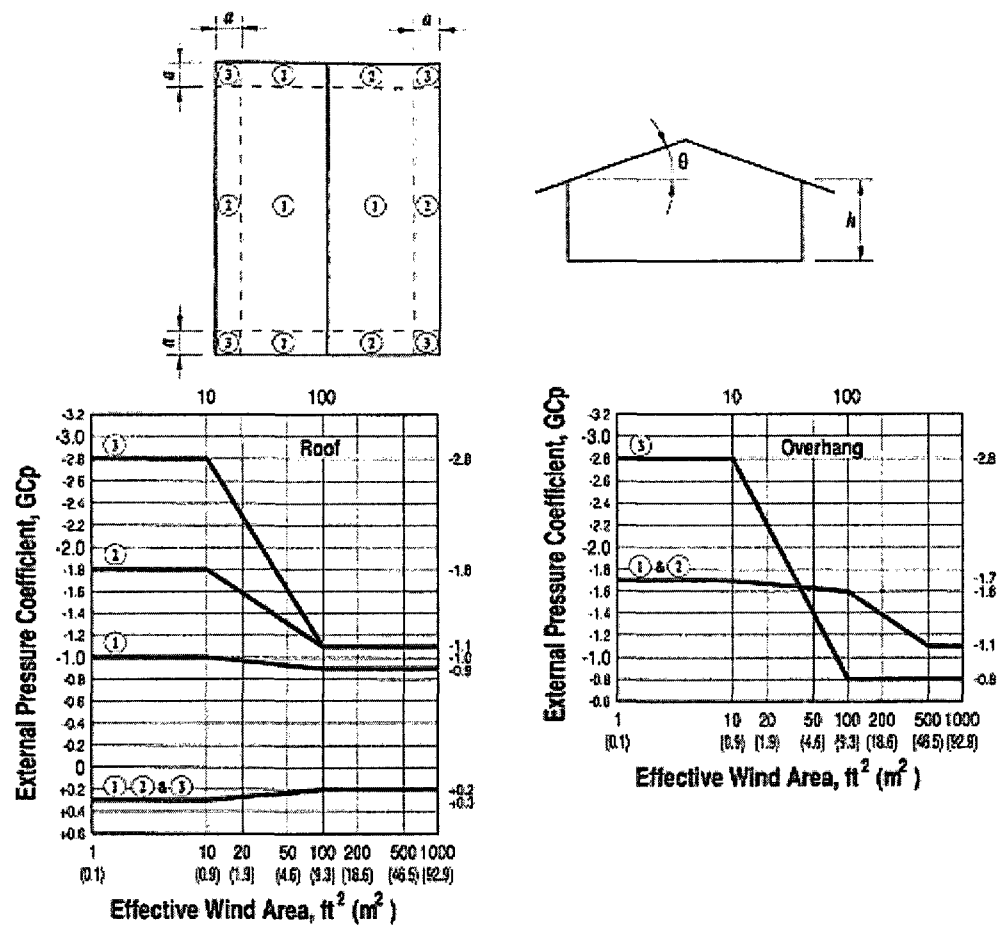
1. Plus and minus signs signify pressures acting toward and away from the internal surfaces, respectively.
2. Two cases shall be considered to determine the critical load requirements for the appropriate condition:
  - (i) a positive value of  $GC_{pi}$  applied to all internal surfaces
  - (ii) a negative value of  $GC_{pi}$  applied to all internal surfaces



**Notes:**

1. Vertical scale denotes  $GC_p$  to be used with  $q_h$ .
2. Horizontal scale denotes effective wind area, in square feet (square meters).
3. Plus and minus signs signify pressures acting toward and away from the surfaces, respectively.
4. Each component shall be designed for maximum positive and negative pressures.
5. Values of  $GC_p$  for walls shall be reduced by 10% when  $\theta \leq 10^\circ$ .
6. Notation:
  - $a$  : 10% of least horizontal dimension or  $0.4h$ , whichever is smaller, but not less than either 4% of least horizontal dimension or 3 ft (0.9 m).
  - $h$  : Mean roof height, in feet (meters), except that eave height shall be used for  $\theta \leq 10^\circ$ .
  - $\theta$  : Angle of plane of roof from horizontal, in degrees.

**Figure B.1 External pressure coefficients,  $GC_{pf}$  (Walls)**



**Notes:**

1. Vertical scale denotes  $GC_p$  to be used with  $q_h$ .
2. Horizontal scale denotes effective wind area, in square feet (square meters).
3. Plus and minus signs signify pressures acting toward and away from the surfaces, respectively.
4. Each component shall be designed for maximum positive and negative pressures.
5. If a parapet equal to or higher than 3 ft (0.9 m) is provided around the perimeter of the roof with  $\theta \leq 7^\circ$ , Zone 3 shall be treated as Zone 2.
6. Values of  $GC_p$  for roof overhangs include pressure contributions from both upper and lower surfaces.
7. Notation:
  - a : 10 percent of least horizontal dimension or  $0.4h$ , whichever is smaller, but not less than either 4% of least horizontal dimension or 3 ft (0.9 m).
  - h : Eave height shall be used for  $\theta \leq 10^\circ$ .
  - e : Angle of plane of roof from horizontal, in degrees.

**Figure B.2 : External pressure coefficients,  $GC_p$  (Roofs)**